

NORTHWESTERN UNIVERSITY

**A Nano to Macro Study of Friction and Adhesion
in Granular Materials**

A DISSERTATION

SUBMITTED TO THE GRADUATE SCHOOL
IN PARTIAL FULFILLMENT OF THE REQUIREMENTS

for the degree

DOCTOR OF PHILOSOPHY

Field of Chemical and Biological Engineering

By

Benjamin L. Severson

EVANSTON, ILLINOIS

June 2007

© Copyright by Benjamin L. Severson 2007
All Rights Reserved

ABSTRACT

A Nano to Macro Study of Friction and Adhesion in Granular Materials

Benjamin L. Severson

The study of granular matter is both scientifically intriguing and industrially important, yet it presents several unique characteristics and challenges. The discrete nature of granular materials often precludes the use of the continuum descriptions that are so commonly used for fluids, so alternative methods must be developed. Particles interact via their surfaces, which allows surface forces such as friction and adhesion to affect essentially any aspect of their collective behavior. The origins of these forces stem from molecular-level surface properties, so a study of friction and adhesion in granular flows requires a multi-scale approach.

Experimental results presented here show that even nanoscale differences in surface roughness greatly affect the angle of repose in a rotating drum. Surprisingly though, rough and smooth particles with considerable differences in their angles of repose do not segregate, putting into question a common explanation for segregation.

Particle dynamics simulations can connect inter particle friction and adhesion to bulk granular behavior. Simulation results for binary systems of particles that differ only in their adhesive or frictional properties show a strong dependence upon the relative concentration of particle types and particle interaction strength. Molecular systems display a similar range of behavior, which has prompted the application of the structure of thermodynamic solution theory to analyze the granular system.

Friction and adhesion manifest themselves in different ways in granular materials depending upon the size of the particles. For micro and nanoparticles, van der Waals adhesion can be significant and even dominate particle behavior. Adhesion was incorporated into particle dynamics simulations and applied to systems of small particles in shearing, drum rotation, and to develop a novel type of mechanical damping device.

On the molecular level, simulations capture the origins of friction and adhesion. Monte Carlo

simulations were used to calculate the adsorption isotherms of model lubricants (long-chain alkanes) along with their density and orientation profiles in slit shaped pores. The adsorption behavior of the lubricant affects the stability of thin films at high temperatures and stresses. Molecular simulations predicted temperature and load combinations which can induce lubrication failure.

Dedicated to my sweet wife Sarah,
who was with me through this whole wild ride.

Contents

CHAPTER 1	Introduction	13
I.	Importance and setting	13
A.	Friction effects in segregation	14
II.	Particle dynamics simulations	16
A.	Contact forces	17
B.	Limitations of the particle dynamics method	21
C.	Sensitivity to parameters	23
III.	Particle size effects	25
IV.	Adhesion	27
A.	Van der Waals forces and Hamaker's equation	27
B.	Contact mechanics of adhesive elastic spheres: JKR and DMT theories	29
C.	Surface roughness effects on adhesion	31
D.	Capillary forces in moist granular materials	35
V.	Origins of friction and laws across length scales	37
VI.	Fine powders (micro and nano)	38
VII.	Organization of the dissertation	40

CHAPTER 2	Surface Roughness Effects in Granular Matter	41
I.	Introduction	41
II.	Experimental approach	43

	7
A. Chrome steel beads and their tribological characteristics	43
B. Rotating tumbler	49
III. Experimental results	50
A. Mono-disperse angle of repose	50
B. Do different angles of repose cause segregation?	50
C. Angle of repose of bi-disperse mixtures	52
IV. Simulation of particles with varying friction	55
V. Conclusions	57
CHAPTER 3 Granular mixtures: analogy with chemical solution thermodynamics	59
I. Introduction	59
II. Simulation method.	60
A. Force Models	61
B. Flow geometries	62
III. Dependence of the angle of repose on friction and adhesion	64
IV. Contact analysis of well mixed systems	64
V. Ideal and non-ideal behavior of a granular mixture	65
VI. Granular viscosity	67
VII. Conclusions	68
CHAPTER 4 Mechanical Damping Using Adhesive Micro or Nano Powders	70
I. Introduction	70
II. Particle dynamics simulations	71
III. Force models	72
A. Normal force with adhesion	72
B. Tangential forces with adhesion	73
C. Addition of adhesion hysteresis	75
IV. Device design	77
A. Couette flow	78

	8
B. Modifying the geometry of the shear cell	79
C. Piston geometry	81
V. Conclusion	84
CHAPTER 5 Analysis of lubrication failure using molecular simulation	85
I. Introduction	85
II. Molecular model	88
III. Grand canonical Monte Carlo methods	88
IV. Solvation pressure	90
V. Effects of temperature and fluid pressure	92
VI. Grand isostress ensemble methods	93
VII. Grand isostress ensemble results	95
VIII. Conclusions	98
CHAPTER 6 Monte Carlo simulation of n-alkane adsorption isotherms in carbon slit	
pores	100
I. Introduction	100
II. Molecular model	102
III. Simulation method	104
IV. Results	105
A. Density and orientation profiles	105
B. Isotherms	109
C. Effect of temperature	111
V. Conclusion	116
CHAPTER 7 Conclusions	118
I. Specific	118
II. Connections between chapters	121
III. Recommendations	122

List of Tables

1.1. The design matrix of a $2^{(4-1)}$ fractional factorial design of experiments	25
1.2. The average effect of the simulation parameters on the angle of repose	25
1.3. Explanation of variables in dimensionless numbers	26
1.4. Values of dimensionless ratios	27
2.1. Typical surface roughness of beads	45
2.2. Coefficients of friction from a tribometer	46
2.3. Coefficients of friction from sliding tripods	47
2.4. Critical angle to initiate the sliding of a tripod of particles	48
3.1. Values of the constants used in particle dynamics force models	62
4.1. The default particle properties in damping simulations	77
5.1. Grand isostress and grand canonical ensemble calculations of stable gap heights . . .	96
6.1. Alkane and slit wall interaction parameters	103

List of Figures

1.1. Radial segregation caused by differences in particle size	15
1.2. Graphical depiction of α in a particle dynamics simulation	19
1.3. The dynamic angle of repose of a granular material in a rotating drum	24
1.4. Explanation of variables in Equation (29)	28
1.5. Simulation of adhesion between finite planar surfaces	32
1.6. Adhesion force between finite planes	33
1.7. Gold surface with nanoscale sinusoidal roughness	33
1.8. Adhesion force with sinusoidal roughness	34
1.9. A liquid bridge between two particles	36
2.1. The quasi-2D rotating drum with 2 mm particles	43
2.2. Typical surface profiles	44
2.3. Angle of repose as a function of Froude number	53
2.4. Angle of repose as a function of concentration of rough particles	54
2.5. Particle dynamics pictures of the angle of repose	56
3.1. The simulation volume of the rotating cylinder simulations.	63
3.2. The simulation volume of the sheared parallel plates.	63
3.3. The angle of repose as a function of friction coefficient and adhesion	64
3.4. Contact analysis of a binary mixture	65
3.5. Angle of repose as a function of mixture composition	66

	11
3.6. Viscosity as a function of friction coefficient and concentration	68
4.1. Example of a normal collision with adhesion hysteresis	77
4.2. Shear cell geometry.	78
4.3. Shear stress as a function of the packing density	78
4.4. Shear stress as a function of the energy release rate of unloading (Γ_r)	80
4.5. Shear stress as a function of the energy release rate of loading (Γ_a)	80
4.6. Couette shear cell with teeth to break up agglomerates.	81
4.7. Enclosed container with moving piston	82
4.8. The position and force experienced by the disc in the piston	82
4.9. Area determining the energy dissipated per cycle	83
4.10. Energy dissipated per cycle for increasing packing density	83
5.1. A lubricant between two asperity surfaces	86
5.2. Solvation pressure as a function of gap height	90
5.3. Pentane isotherms in slits of various heights at 300 K.	93
5.4. Pentadecane isotherms in a 19.2 Å slit at various temperatures.	93
5.5. Picture of a gap fluctuation move	95
5.6. Grand Isostress simulations squeezing out the lubricant	97
5.7. Lubrication gap for several temperature-load combinations for pentadecane	98
6.1. The slit pore unit cell	102
6.2. Ethane density and orientation profiles showing ordered layers	106
6.3. Pentane density and orientation profiles showing ordered layers	107
6.4. Density and orientation profiles at varying pressure	108
6.5. Picture of slit pore with pentane at a pressure just below pore filling	108
6.6. Pentane density and orientation profiles at 300K and 1500K	109
6.7. Ethane isotherms at 300 K in slits of various heights	110
6.8. Pentane isotherms at 300 K in slits of various heights	110
6.9. Decane isotherms at 300 K in slits of various heights	112

	12
6.10. Hysteresis between the adsorption and desorption isotherms for decane	112
6.11. Comparison of isotherms for alkanes of different lengths	113
6.12. Pentane isotherms at various temperature in a 19.2 Å slit	114
6.13. Pentadecane isotherms in a 19.2 Å slit for temperatures from 300 to 1500 K	114
6.14. Collapse of pentane isotherms at different temperatures with Polanyi potential . . .	115
6.15. Collapse of isotherms of different species with Polanyi potential	116

This dissertation is aimed at understanding the role of friction and adhesion in granular materials. Friction and adhesion are surface forces which arise from the atomic and nanoscale properties of the solid surfaces of the particles involved. This study involves a multi-scale problem spanning length-scales of many orders of magnitude to connect the atomic level properties of surfaces to macroscopic behavior. Particle dynamics simulations provide a useful way to connect particle properties to bulk granular behavior.



Introduction

I Importance and setting

The prevalence of granular matter is astounding. A large portion of the earth's surface is composed of granular matter such as sand, gravel, rocks, soils, snow and ice. Their common occurrence in nature is mirrored in industry. Granular materials are major components of the raw materials, intermediates, and products in the mining, chemical, pharmaceutical, and food industries. As a group they rank second in their importance to human activity and consume roughly ten percent of all the energy produced on this planet in their processing and transport [1]. Granular materials can range from low value added commodities to specialty high value added materials. In the pharmaceuticals industry, on the high end, a resurgence of attention to manufacturing is predicted now that the boom of drug discovery seems to have peaked [2]. Due to long neglect, the potential to increase profits through manufacturing improvements rivals that of discovering new drugs [3].

Granular matter has received a resurgence of attention from academia in the last two decades (especially by the physics community). One focus of the recent activity is that they represent a

unique form of matter [4]. Granular materials undergo phase transitions as their level of kinetic energy increases. A granular pile at rest acts as a solid—it can resist a stress. When the grains are given enough energy to flow, they can act like a liquid. Finally a vigorously shaken group of grains has many properties of a gas. These granular phases are distinct from their thermodynamics counterparts. The two major characteristics that make them unique are that temperature plays no role, and the interactions between grains are dissipative [5]. Friction, as one of the main mechanisms of dissipation, is at the heart of what makes granular systems such a unique and counter-intuitive form of matter. Because of their dissipation, a constant energy flux is required to maintain granular materials in one of the fluid states. Without it, a granular gas or liquid quickly settles to the solid state. Friction alters the amount of energy input needed to sustain a granular material in a fluid granular state.

Of the granular phases, solids and dense fluids are the most likely to be sensitive to surface forces. These systems have the most surface contacts, and friction will dominate over other dissipation mechanisms. Granular flows are prevalent in industry and could greatly benefit from a better understanding of the effects of surface forces. Some common forms of transport include: flow through chutes, hoppers, down inclines or even pneumatic conveyance. Processing operations include: grinding, mixing, and sieving. Major problems in industry can be grouped into two categories [1]. The first are problems occurring with clogging or arching during flow which cause blockage and halt the procedure. The second is segregation during mixing or flow when homogeneity is desired. Friction and adhesion between grains are at the heart of these problems. Inter-particle contacts are very important to the behavior of a granular material. Friction and adhesion at these contacts will have an effect on essentially all granular phenomena.

A Friction effects in segregation

The effects of friction and adhesion in granular materials are not always intuitive. This is the case with segregation. A binary mixture of granular materials often segregates during flow or vibration due to differences in particle properties. Segregation has often been observed due to differences in particle size or density. More recently, segregation due to differences in adhesion

was also observed [6], but in spite of several theoretical predictions [7–9], segregation has not been observed due to differences in particle friction [10]. This will be discussed in more detail in Chapter 2.

One useful geometry to study segregation is a quasi-two-dimensional rotating drum (a cylinder whose radius is much larger than its depth). A typical segregation pattern shows one species located at the center of the drum with the other species preferentially at the edges (Figure 1.1). This is commonly called radial segregation.

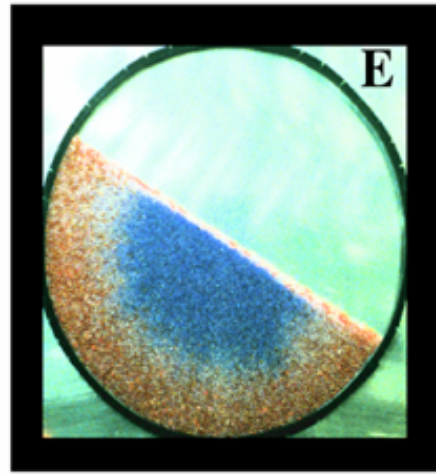


Figure 1.1: *Radial segregation caused by differences in particle size. [11]*

The non-segregation of particles differing only in their frictional properties draws into question a popular mechanism used to explain radial segregation. In the mechanism, segregation is based on differences in the angle of repose of the two materials. The angle of repose is the slope that the flowing granular material forms as it is rotated in the drum, and is thought to be a measure of flow ability. The model predicts that the material with the lower angle of repose will flow more readily down the slope, completely cross the diameter of the drum, and position this component preferentially at the perimeter. The material with a higher angle of repose is more likely to stop flowing before crossing the diameter of the drum, and get trapped in the center of the drum.

Particles which differ only in their frictional properties can display large differences in their angle of repose [10, 12–14]. Therefore by not segregating, frictional particles are an exception to the angle of repose explanation of segregation.

Fortunately there is another explanation of segregation that does not rely on the angle of repose. In this mechanism, segregation is based upon the preferential percolation of one particle type through the flowing layer. This mechanism can account for why small particles are found in the center of the drum during size segregation, and also why the more dense particles are found in the center of the drum during density driven segregation. Apparently, differences in friction do not significantly affect a particles ability to percolate.

II Particle dynamics simulations

Several different methods have been developed to simulate the behavior of granular materials, including the use of continuum models, cellular automata, Monte Carlo, hard sphere (event driven) and particle dynamics. Each method has advantages and disadvantages stemming from the assumptions made in the model. The focus here is on the particle dynamics method—which offers perhaps the greatest degree of realism of the simulation methods listed. Particle dynamics simulations are sometimes also called the discrete element method (DEM), the soft-sphere model, or even molecular dynamics. The title “particle dynamics” is used here because it is more descriptive than the “DEM”, and the usage of “molecular dynamics” could be confused with simulations done on the molecular scale.

Calling particle dynamics simulations the “soft sphere model” can perhaps be somewhat misleading to people not familiar with this field and perhaps should be clarified. The term has nothing to do with the elastic properties of the particles in the simulation. They are called soft spheres because a particle collision is resolved in several time steps. In contrast, the hard-sphere model uses an event driven algorithm which progresses by predicting which particles will collide next and then instantly resolving the outcome of the collision. We prefer the soft sphere method for our purposes since it more directly links particle properties to contact forces as will be explained.

Particle dynamics simulations offer a method to directly study the connection between individual particle properties and the collective particulate behavior. These simulations track the individual motion of up to a few thousand particles based on force rules from contact mechanics. The effects of particle properties on bulk flow behavior are readily visible from this technique, as

particle properties can be modified individually.

Particle dynamics simulations are the offspring of molecular dynamics simulations and use the same algorithm by integrating Newton's laws of motion to update the particle positions and velocities through time [15,16]. Several of these algorithms have been analyzed for their efficiency in particle dynamics simulations. The half-step Verlet algorithm has been found to be effective [17]. The simulations reported in this dissertation allow translational and rotational movement of particles in all three dimensions.

$$\ddot{x}_i = \frac{1}{m} \sum f_i \quad (1)$$

$$\ddot{\theta}_i = 1/I \sum t_i \quad (2)$$

Where x is the particle's position and m is its mass in Equation (1). Rotational motion is accounted for by updating the rotational law of motion according to the moment of inertia of the particle (I) and the experienced torques (t_i) as shown in Equation (2).

Particle dynamics simulations need the initial particle positions and velocities as an input. From the initial conditions, particle positions and velocities are updated at each time-step to track the particle behavior through time. This updating is done by integrating Newton's law of motion. The forces needed in order to integrate the equation of motion come from force models to be discussed shortly.

A Contact forces

Normal contact of elastic solids: Hertz theory Heinrich Hertz first developed a theory for the elastic contact of spheres while studying the diffraction patterns of light in contacting glass lenses [18]. When two solid spheres are brought into contact they first touch at a single point, and as the load is increased the contact region grows into a circle. Hertz derived a relationship between the applied load (P), the elastic repulsive forces needed to balance that load, and the size and distribution of stress throughout the circular contact area caused by the load. Some of the important results are listed here. Johnson has provided a detailed derivation [19].

For two spheres with radii, elastic moduli, and Poisson ratios of R_i , E_i , and ν_i the collective elastic and geometric properties are:

$$\frac{1}{R^*} = \frac{1}{R_1} + \frac{1}{R_2} \quad (3)$$

$$\frac{1}{E^*} = \frac{1 - \nu_1^2}{E_1} + \frac{1 - \nu_2^2}{E_2} \quad (4)$$

In Hertz theory, the radius of the contact circle is found to be:

$$a = \left(\frac{3PR^*}{4E^*} \right)^{1/3} \quad (5)$$

The pressure distribution over the contact region is:

$$p = p_0[1 - (r/a)^2]^{1/2} \quad (6)$$

where r is the distance from the center of the contact circle and p_0 is the maximum contact pressure given by

$$p_0 = \left(\frac{3P}{2\pi a^2} \right) = \left(\frac{6PE^{*2}}{\pi^3 R^{*2}} \right)^{1/3} \quad (7)$$

and the approach of the centers of mass is:

$$\alpha = \frac{a^2}{R^*} = \left(\frac{9}{16} \frac{P^2}{R^* E^{*2}} \right)^{1/3} \quad (8)$$

Of these equations, Equation (8) is the most important to our particle dynamics algorithm. In a simulation, α can be calculated by subtracting the distance between the centers of mass of two particles from the sum of their radii. Then Equation (8) can be rearranged to solve for the normal force between two particles as a function of α :

$$f_n = 4/3 E^* \sqrt{R^*} \alpha^{3/2} = K_n \alpha^{3/2} \quad (9)$$

where we have substituted f_n for P . α can also be thought of as the amount that the spheres overlap in a particle dynamics simulation as depicted in Figure 1.2.

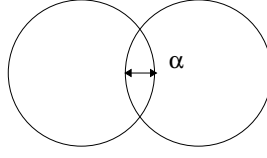


Figure 1.2: Graphical depiction of α in a particle dynamics simulation

Tangential forces Tangential, or shear, forces between particles are connected to the normal force through Coulomb's laws of friction.

$$f_t \leq \mu_s f_n \text{ for static friction} \quad (10)$$

$$f_t = \mu_d f_n \text{ for dynamic friction} \quad (11)$$

Here μ_s and μ_d are the static and dynamic friction coefficients. The \leq sign in Equation (10) signifies that under static conditions the tangential force exactly counteracts the unknown external tangential force. A tangential force larger than $\mu_s f_n$ will cause the particles to begin sliding. While sliding, the tangential force is calculated using Equation (11). While descriptive, Equation (10) does not enable the calculation of the tangential force in a particle dynamics simulation for static conditions. To calculate the tangential force, models patterned after the work of Mindlin are often used [20]. One such model [21] is to simply use a linear spring.

$$f_t = K_t s \quad (12)$$

In this model, the tangential force is proportional to s , which is the tangential displacement between surfaces since they came into contact. The tangential displacement can be calculated as:

$$s(t) = \int_{t_0}^t v_s(t') dt' \quad (13)$$

Note that v_s has contributions from both the relative translational velocities and rotational velocities of the particles in contact. Another popular model adds a —the radius of the contact area from

Hertz theory—into the tangential force model [22].

$$f_t = K_t a s \quad (14)$$

Either of these models for the static tangential force can be put together succinctly with the tangential force during sliding as:

$$f_t = \min(|K_t s|, |\mu f_n|) \quad (15)$$

Usage of Equation (15) in the simulation progresses as follows. When particles first come into contact s is small and so the friction force will be determined by the tangential spring. After some amount of tangential displacement, the criterion for sliding is likely to be reached where the tangential force will then be calculated from the product of the friction coefficient with normal force.

Energy dissipation Accounting for the energy dissipation that occurs when particles collide, rub and roll against each other is critical to accurately capture their behavior and bulk properties. If particles do not fracture or plastically deform, then kinetic and potential energy are converted into thermal energy. Particle dynamics methods generally separate energy dissipation into impact dissipation and frictional dissipation, although in reality both of these mechanisms reflect the ability of particles to turn their kinetic energy into vibrations and then heat as the vibrations become disordered. Impact dissipation is often discussed in terms of the coefficient of normal restitution e_n of a collision, which is the ratio of the velocities before and after contact.

$$e_n = -\frac{v_n^f}{v_n^i} \quad (16)$$

The coefficient of restitution is bounded between 0 and 1 where 1 is a perfectly elastic collision and 0 is perfectly inelastic. Dissipation has sometimes been added to the Hertz model with the addition of a damping term, which is proportional to the velocity of the particles (17).

$$f_n = -K_n \alpha^{3/2} - K_d v_n \quad (17)$$

This expression for damping leads to the unphysical behavior of an increasing coefficient of restitution with v_n^i [17,23] compared to experiments showing that $(1 - e_n)$ is proportional to $v_n^{i-1/5}$ [24]. Derivations for viscoelastic particles give the following expression for the elastic force with damping [25,26]:

$$f_n = -K_n \alpha^{3/2} - K_d \sqrt{\alpha} v_n \quad (18)$$

This equation correctly models the behavior of e_n as a function of v_n^i . Models capturing normal forces and damping of plastic particles have also been developed [27], but they are beyond the scope of this dissertation.

B Limitations of the particle dynamics method

The inability to simulate large numbers of particles and long times can limit the capabilities of particle dynamics simulations. However, many methods have been developed to ease these limitations.

Number of particles The scaling of the computational time as the number of particles increases depends upon the contact detection scheme used. At each time step during a simulation, a list of particles which touch (or interact) is passed to the routine which calculates the contact forces. The simplest way (but not the most efficient) is to calculate the distance between every pair of particles to find out which interact. This algorithm causes the computational time to scale as N^2 where N is the number of particles in the simulation. The inclusion of a cell list, neighbor list or both can reduce this scaling factor [15]. An appropriate contact detection scheme can reduce this scaling factor so that the computational time scales with $N \log N$ [28].

Even with this improvement, particle dynamics simulations are generally limited to simulating less than 10,000 particles on a single processor. However, the appropriate use of periodic boundary conditions can often enable the simulation of bulk granular properties from a relatively small system of particles.

Other techniques are emerging to take advantage of symmetries in the problem geometry or periodicities in time [28]. In other cases, the important dynamics are often limited to a thin flowing

layer. The simulation of particles outside of this important region can often be greatly simplified to increase the computational speed or to simulate a much larger system [29].

Time step The computational time of a simulation is inversely proportional to the time step used. The time step in a simulation should be small enough to resolve a collision at a characteristic velocity of the problem to be studied in no fewer than around 30 time steps. Resolution of a collision in too few time-steps can result in uncontrolled energy gains and losses. A good estimate of the necessary time step, Δt , can be calculated from the Rayleigh wave speed of force transmission on the surface of elastic bodies [30]. For a granular material, the highest frequency of Rayleigh wave propagation is determined by the smallest particles, leading to a critical time step Δt_c given by

$$\Delta t_c = \frac{\pi d_{p_{min}}}{2\lambda} \sqrt{\frac{\rho_p}{G}} \quad (19)$$

where $d_{p_{min}}$ is the diameter of the smallest particle, G is the shear modulus and λ is

$$\lambda = 0.1631\nu + 0.8766 \quad (20)$$

Equation (19) shows the relationship between time-step particle size, density, and elastic properties. The time step needs to decrease with particle size to be able to capture the dynamics of a collision. With the number of particles, particle size, density and elastic properties to consider, knowing what length and time scales that can be tackled with a particle dynamics simulation can be complicated. For code which employs a contact detection algorithm that scales with $N \log N$, a simulation of 3000 1 mm glass particles for one second takes about eight hours on a single 3 GHz processor.

Particle Shape Besides system size and time limitations, particle shape can also present a problem. The most convenient particle shape to simulate is the sphere. The boundary of a sphere is completely defined by the sphere's radius and the position of its center of mass. This becomes important when considering which particles interact. In addition, deriving force models from contact mechanics for complex geometries is not trivial. Some work has been done on a few other

particle shapes. A good review of some of the basic strategies to simulate non-spherical particles has been provided by Dziugys and Peters [31]. One method is to build a non spherical particle by attaching a few spheres together to create a composite particle. Rods, tetrahedrons and cubes can reasonably be simulated using this technique [32]. The contact detection schemes and force models as described above can be directly applied to the new particle construct. One drawback is that since each particle construct consists of multiple spheres, fewer particle constructs can be simulated in a reasonable amount of time. Another approach has attempted to simulate polygons [33,34]. These simulations are only two-dimensional. Contact algorithms and contact forces are dependent upon the area of overlap between two shapes. This necessitates simplifications to the contact mechanics. A third approach to simulating non-spherical particles to focus on ellipsoids. This approach benefits from the fact that the contact mechanics of Hertz and Mindlin have easy extensions for ellipsoids. The challenges have mainly come from developing efficient contact detection algorithms, but some groups have made good progress [35–38].

C Sensitivity to parameters

It is difficult to know which of the many parameters in a particle dynamics simulation will significantly affect any given calculated property. Too often simulation studies are reported without any type of sensitivity analysis of their results to the parameter values used. A few exceptions to the rule, however, have been published [39–41]. It is quite possible that the property of interest is not a simple function of any single parameter, but depends upon the interplay of two or more parameters. One way to assess the sensitivity of a measured property against changes in the input variables is through a statistically designed set of experiments called the factorial design. An analysis of this type is not new, but it does seem to be rarely used in the simulation community who may not identify well with “experimental” design. However, there is just as much need for applying these techniques whether the experiments are of the traditional or of the simulation variety. Too often particle dynamics simulations are performed without much thought about the parameters which are input. Which of these parameters are important to the quantities which I am calculating? If I have errors in some of these parameter values that I input, how much is that

likely to affect my results?

To show how the factorial design of experiments can clearly answer these questions we will show the simulation results and analysis of a simple example—the particle properties which influence the dynamic angle of repose in a rotating drum. Setting up the factorial design requires a choice of particle properties which might have an effect on the angle of repose. The constants from Equations (18) and (15) were chosen here to analyze their individual and combined effects on the angle of repose. A certain number of values for each variable is then chosen to investigate. In this example only two values of each variable were necessary to quickly assess their importance.

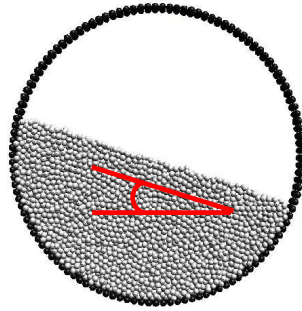


Figure 1.3: *The dynamic angle of repose of a granular material in a rotating drum*

As is suggested by the name, the design matrix of the full factorial design of 4 variables with 2 values each will contain 2^4 combinations of parameters or 16 possible simulation runs. If higher order terms are not of interest or not suspected, this design matrix can be simplified and yet still preserve the capability to investigate lower order effects. If only first and second order effects are of interest, the design matrix in this case simplifies to a 2^{4-1} fractional factorial design. A good reference for designing fractional factorial matrices is provided by Montgomery [42]. With this simplification, the number of simulations decreases from 16 to 8 while preserving the information that we want. The design matrix for the 2^{4-1} fractional factorial design is shown in Table 1.1 along with the calculated angles of repose for each parameter set.

The average effect of each individual parameter is analyzed by subtracting the average angle of repose of runs where a parameter is low from the average angle of repose where a parameter is high. Results of this operation are shown in Table 1.2. The friction coefficient is by far the most important simulation parameter affecting the angle of repose. It accounts for essentially all of the

Table 1.1: The design matrix of a $2^{(4-1)}$ fractional factorial design of experiments. (+) or (−) signifies if the higher or lower value of each parameter is used in a particular experimental run.

Run #	K_s	μ	K_d	K_n	Ave. Angle (Degrees)	Std. Dev.
1	-	-	-	-	19.64	0.71
2	+	-	-	+	19.70	0.83
3	-	+	-	+	26.60	1.17
4	+	+	-	-	26.50	0.82
5	-	-	+	+	19.73	0.74
6	+	-	+	-	19.88	0.73
7	-	+	+	-	26.28	1.08
8	+	+	+	+	26.65	0.79

Table 1.2: The average effect of the simulation parameters on the angle of repose

	Average Effects (degrees)
K_t	0.12
μ	6.77
K_d	0.02
K_n	0.10

difference in the angle of repose between runs. Two-way effects can also be extracted from this type of experimental analysis to analyze if a combination of parameters is critical to the measured property, but in this example there were not any two-way effects.

III Particle size effects

The particle dynamics force models described in the previous section are generally appropriate to simulate the behavior of dry granular material consisting of particles larger than $100 \mu\text{m}$ in size. Below that size threshold the physics of the problem can change considerably. Forces that are insignificant on a millimeter particle scale can dominate the dynamics of micrometer or nanometer sized particles. In particular, surface forces including adhesion and friction increase in importance. Much of this change in physics can be understood through the surface area to volume ratio of a spherical particle. As the size of the particle decreases, the surface area to volume ratio increases as seen in Equation (21). A corresponding increase in the importance of surface forces occurs with the increase in surface area.

$$\frac{\text{surface area}}{\text{volume}} = \frac{4\pi R^2}{4/3\pi R^3} = \frac{3}{R} \quad (21)$$

Dimensionless numbers and the relevant physics The relevant physics of the problem can be estimated through appropriate dimensionless numbers. Equations (22)–(27) are derived from ratios of forces [43]. An explanation of the variables in these dimensionless numbers is given in Table 1.3.

$$\frac{\text{gravity}}{\text{viscous}} = \frac{\pi R^3 \rho g}{\eta R v} \quad (22)$$

$$\frac{\text{inertial}}{\text{viscous}} = \frac{\rho R^2 v^2}{\eta R v} \quad (23)$$

$$\frac{\text{gravity}}{\text{inertial}} = \frac{\pi R^3 \rho g}{\rho R^2 v^2} \quad (24)$$

$$\frac{\text{adhesive}}{\text{viscous}} = \frac{f_r \gamma R}{\eta R v} \quad (25)$$

$$\frac{\text{adhesive}}{\text{inertial}} = \frac{f_r \gamma R}{\rho R^2 v^2} \quad (26)$$

$$\frac{\text{adhesive}}{\text{gravity}} = \frac{f_r \gamma R}{\pi R^3 \rho g} \quad (27)$$

Table 1.3: Explanation of variables in dimensionless numbers and values used in sample calculations. The values were chosen to mimic a system of glass particles in air.

Symbol	Property	Value	Units
ρ	Solid density	2,200	kg/m^3
η	Fluid viscosity	1.82×10^{-5}	$\text{Pa}\cdot\text{s}$
γ	Solid surface energy	0.10	J/m^2
f_r	Surface roughness factor	0.001	unitless
g	Gravitational acceleration	9.81	m/s^2
v	Characteristic velocity	0.01	m/s

Table 1.4: *Values of dimensionless ratios based on properties listed in Table 1.3*

Dimensionless Ratio	Particle Diameter (m)					
	10^{-3}	10^{-4}	10^{-5}	10^{-6}	10^{-7}	10^{-8}
grav./vis.	10^5	10^3	10^1	10^{-1}	10^{-3}	10^{-5}
inert./vis.	10^3	10^2	10^1	10^0	10^{-1}	10^{-2}
grav./inert.	10^2	10^1	10^0	10^{-1}	10^{-2}	10^{-3}
adh./vis.	10^2	10^2	10^2	10^2	10^2	10^2
adh./inert.	10^{-1}	10^0	10^1	10^2	10^3	10^4
adh./grav.	10^{-3}	10^{-1}	10^1	10^3	10^5	10^7

Consider, for example a typical system of particles with the properties listed in Table 1.3. The values of the ratios in Equations (22)–(27) were calculated for particles ranging in size from 1 mm down to 10 nm and the results are shown in Table 1.4. The values of the different ratios clearly show the change in physics as the particle size decreases. Where gravitational and inertial forces dominate the mm scale, adhesive and viscous forces dominate the nanoscale.

IV Adhesion

Adhesion is commonly observed in granular materials. Adhesion may stem from a number of different sources including capillary forces, static electricity and van der Waals attraction. The importance of each of these factors to the total attractive force will depend on both ambient conditions and material properties. Static electricity mostly affects poorly conducting particles in dry environments [44], and capillary forces are only present when the relative humidity is high. The theories of adhesion are reviewed here, but it is very difficult to predict actual adhesion from theory due to the many contributions to adhesion and their sensitivity to past history and ambient conditions.

A Van der Waals forces and Hamaker's equation

Van der Waals forces are comprised of three types of atomic interactions: dipole/dipole, dipole/induced-dipole, and induced-dipole/induced-dipole interactions. This last interaction explains how even uncharged, non-polar atoms can experience attractions. Fluctuations in the electron density around non-polar atoms can cause an instantaneous dipole. This dipole can induce a dipole in a neigh-

boring atom. The attraction between the two is called London dispersion forces, as it was first proposed by London in 1930 [45]. London showed that the potential energy for these interactions has an inverse sixth power dependence on the distance between the two atoms involved.

$$w(r) = -\frac{C}{r^6} \quad (28)$$

In 1937, Hamaker calculated the van der Waals interaction between macroscopic solid spheres [46]. By assuming that the pair-wise interactions of all of the atoms in the solid bodies were additive, he integrated the London potential between two spheres and obtained:

$$W(z) = -\frac{A}{12} \left[\frac{D_1 D_2}{z^2 + zD_1 + zD_2} + \frac{D_1 D_2}{z^2 + zD_1 + zD_2 + D_1 D_2} + 2 \ln \left(\frac{z^2 + zD_1 + zD_2}{z^2 + zD_1 + zD_2 + D_1 D_2} \right) \right] \quad (29)$$

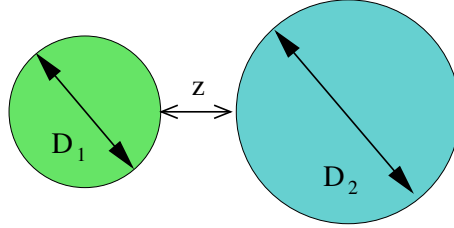


Figure 1.4: Explanation of variables in Equation (29)

where A in Equation (29) is the Hamaker constant which comes from atomic properties and geometric constants and the other variables are shown in Figure 1.4. For the case of $D \gg z$ this result simplifies to

$$W(z) = -\frac{A}{12z} \left(\frac{D_1 D_2}{D_1 + D_2} \right) \quad (30)$$

This assumption is very reasonable when trying to estimate the van der Waals interaction between powder particles which are nearly in contact. In the following chapters, Hamaker's result is applied to particle dynamics simulations as a force ($-dW/dz$).

$$F(z) = -\frac{AR^*}{12z^2} \quad (31)$$

For a good review of the integration of the London potential between solids of this and other geometries see Israelachvili [47]. It should be noted that there are singularities in the above equations when $z = 0$. This arises because no repulsive potential between molecules is considered in Equation (28). Usually a separation of 3\AA is assumed to be the separation causing the maximum adhesion force. Henderson et al. have used Hamaker's approach and integrated the full Lennard-Jones potential over two spherical particles [48]. The Lennard-Jones potential adds a repulsive term to Equation (28) of B/r^{12} . The integration including the repulsive term results in an expression which has a finite equilibrium distance where there is a minimum in the potential energy.

Hamaker's approach to calculating the van der Waals force between spheres is good for rigid spheres, but it does not take into account the elasticity of the solid during contact. Deformation of the particle's shape will affect the adhesion force, and likewise the adhesion forces will cause particle deformation. The following section will discuss how researchers studying the contact of elastic bodies have included the effects of adhesion in their theories.

B Contact mechanics of adhesive elastic spheres: JKR and DMT theories

The theory of Johnson, Kendall, and Roberts (JKR) adds the effects of adhesion to Hertz's theory of elastic contact by considering the contribution of the surface energy to the energy of the compressed elastic spheres [49]. In the theory there are three contributions to the total energy U_T of the contacting spheres: the mechanical potential energy U_M

$$U_M = \frac{-P \left(\frac{P'^{2/3}}{3} + \frac{2PP'^{-1/3}}{3} \right)}{\left(\frac{16E^*2R^*}{9} \right)^{1/3}} \quad (32)$$

the stored elastic energy

$$U_E = \frac{\frac{P'^{5/3}}{15} + \frac{P^2P'^{-1/3}}{3}}{\left(\frac{16E^*2R^*}{9} \right)^{1/3}} \quad (33)$$

and the surface energy

$$U_S = -2\pi\gamma \left(\frac{3R^*P'}{4E^*} \right)^{2/3} \quad (34)$$

Taking the derivative of U_T with respect to P' leads to an expression for the contact radius of an adhesive contact.

$$a^3 = \frac{3R^*}{4E^*} P' \quad (35)$$

where P is the applied load and P' is the effective load, or the apparent Hertz load (the load in Hertz theory required to make the same contact area). P' can be related to the applied load and the critical 'pull-off force' P_c .

$$P' = P + 2P_c + (4PP_c + 4P_c^2)^{1/2} \quad (36)$$

where P_c is

$$P_c = 3\pi\gamma R^* \quad (37)$$

JKR theory also gives us a relationship between α and the applied load. This relationship can be used as a force model in a particle dynamics simulation in the same way as Equation (9) is used with Hertz theory.

$$\frac{\alpha}{\alpha_f} = \frac{3 \left(\frac{P}{P_c} \right) + 2 \pm 2 \left(1 + \frac{P}{P_c} \right)^{1/2}}{3^{2/3} \left[\frac{P}{P_c} + 2 \pm 2 \left(1 + \frac{P}{P_c} \right)^{1/2} \right]^{1/3}} \quad (38)$$

Equation (38) can be used in particle dynamics simulations to calculate the normal force from the positions and radii of the particles. In it, α_f is defined as

$$\alpha_f = \frac{3}{4} \left(\frac{\pi^2 \gamma^2 R^*}{E^{*2}} \right)^{1/3} = \left(\frac{3P_c^2}{16R^*E^{*2}} \right)^{1/3} \quad (39)$$

and represents the tensile deformation that occurs just before particle separation. Also in (38) P_c is the JKR pull-off force and is defined in Equation (37)

Derjaguin, Miller, and Toporov [50] derived a similar theory that is applicable for more rigid materials. It accounts for a ring of material around the contacting area that is near enough to contact to contribute significantly to the adhesion forces. The softer materials for which the JKR theory is applicable deform so that there is no solid outside of the contacting region which significantly contributes to the adhesion force. In spite of the differences in theory produce similar

adhesive behavior. For example the pull-off in DMT theory is:

$$P_c = 4\pi\gamma R^* \quad (40)$$

C Surface roughness effects on adhesion

Hamaker's result forms the theoretical basis of how atomic level van der Waals forces affect larger solid bodies such as two powder particles. However this result is really the maximum possible London force that could be observed between real objects. For example, if we use Hamaker's result to calculate the force between two identical spheres in contact, we can solve for the size of sphere where the London force equals the weight of one of the particles (Appendix I). This calculation predicts that a silica sphere of 1.6 mm diameter should exhibit adhesion comparable to its weight. However this calculation is quite an overstatement, since powder particles larger than 50 μm rarely exhibit cohesion. Kendall [51] calls this the adhesion paradox—the paradox being that atomic theory predicts all matter to be sticky, yet we rarely observe stickiness between the solid objects around us. To reconcile this paradox surface roughness and contamination need to be considered.

Atomistic calculations of adhesion An atomically detailed surface can capture the effects of nanometer surface roughness on the adhesion force between two solid surfaces nearly in contact. Equations (29)-(31) above describing the van der Waals interaction between macroscopic bodies have been derived by assuming that the London interactions between a pair of atoms are additive and then integrating the pair potential to yield a macroscopic expression. Another way to calculate the potential between macroscopic bodies is to manually sum up the pair potentials with a computer instead of using integration. In a calculation at this level of detail the positions of all atoms are known, making it easy to compute the distance between any two atoms in opposing solids. Since the interactions are summed individually it is easy to do not only for smooth, but for rough surfaces as well. The interaction for even arbitrarily rough surfaces could be calculated in this way. A greater understanding of how roughness affects the adhesion force can be achieved after a few simple calculations.

The following calculations use the atomic properties of gold. The atomic radius is 1.4 angstroms, and the atoms are placed in a face-centered-cubic (FCC) crystal structure. The program computes the distances and the forces between each pair of atoms in opposing solid bodies. The forces are then added to give the total interaction between the two objects.

Calculation of adhesion between finite planar slabs One calculation that we can glean insight from is the interaction of two atomically-smooth finite slabs. The routine creates two finite planar surfaces of atoms in a FCC structure separated by a gap of 4 angstroms from atom center to atom center (see Figure 1.5). It then calculates the van der Waals force between slabs of different thicknesses. The routine starts with the planar surfaces being only one atom deep and each subsequent calculation adds one more layer of atoms to each plane making them thicker. The gap remains a fixed distance throughout the process.

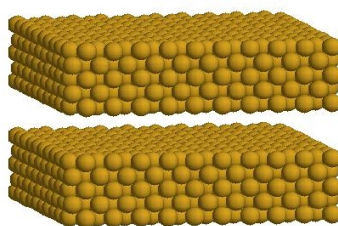


Figure 1.5: *Simulation of adhesion between finite planar surfaces*

A plot of the adhesion force as a function of the number of layers in each planar object yields some interesting insight. First, as seen in Figure 1.6 the force initially increases as more layers are added but then levels off as, at some point, the added layer is too far away from the opposing surface to significantly contribute to the total adhesion force. This illustrates how the van der Waals interaction is short-ranged and is often called a surface force for macroscopic solids. Second, it is notable that more than 40% of the total adhesion force comes from the interactions between the first layer of atoms on each side of the gap and that 99% of the force comes from the interaction between the first 10 atomic layers. Since the adhesion force is so dependant upon the fist few layers of atoms, it is extremely sensitive to surface roughness. The following calculations further

illustrate this idea.

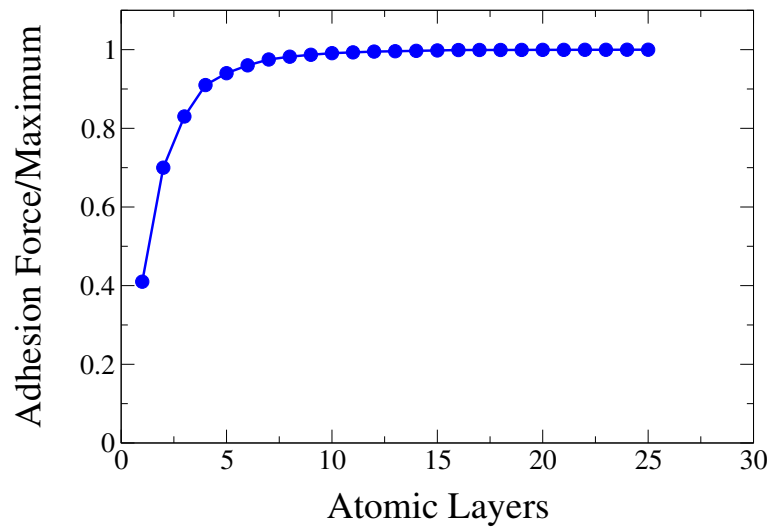
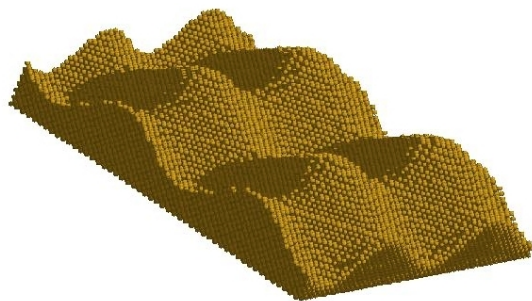
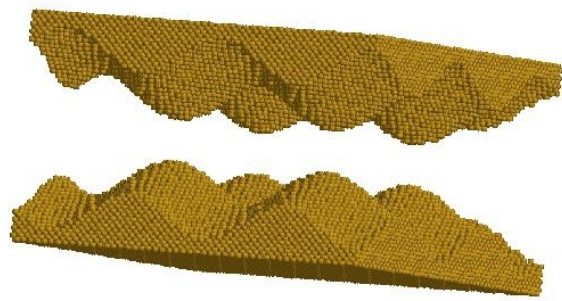


Figure 1.6: Adhesion force between finite planes as a function of layer thickness. The distance between atomic centers across the gap is 4 \AA , and the slab is 400 \AA on a side.

Calculation for sinusoidal roughness The next calculation will illustrate how the addition of roughness to the planar slabs greatly affects the adhesion force between them. Here the surface of the solid follows a sine function in both the x and y directions to model the interaction of rough surfaces (Figure 1.7).



(a) Gold surface with nanoscale roughness with the shape of a sine curve



(b) Two interacting surfaces

Figure 1.7: Gold surface with nanoscale sinusoidal roughness

The following simulation shows how the adhesion force changes as the amplitude of the sine-curve roughness increases. As the amplitude increases, more atoms are deleted from the slab. The period of the sine curve and the separation distance between the slabs remain constant.

The adhesion force between the slabs decreases rapidly as the amplitude of the roughness is increased. Figure 1.8 shows that the adhesion force has decreased to about one percent of the atomically smooth case after the addition of roughness with a 20 atom depth. This corresponds to 5.6 nanometer roughness. Even a highly polished material commonly has about 10 nanometers of roughness. The adhesion force for essentially all rigid solid objects is only a fraction of what it would be in the atomically smooth case.

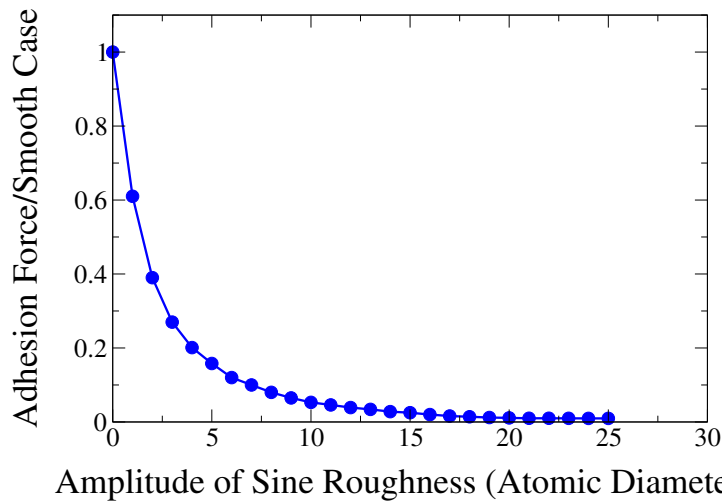


Figure 1.8: Adhesion force as a function of the amplitude of the sine curve roughness. The length of the period of the sine function is 20 atomic diameters.

Various studies have added corrections to Hamaker's expression to account for the decrease in adhesion force due to surface roughness. One approach to doing this uses the radius of one asperity instead of the radius of the whole particle [51]. Rumpf [52] expanded upon this to take into consideration that the asperities are sitting upon the sphere of much larger radius. He created a model which accounts for both the adhesion between asperities at a close distance plus the interaction of the much larger spheres at that distance plus the height of the asperities.

$$F_{Rumpf}(z) = \frac{A}{6} \left(\frac{r}{z^2} + \frac{D}{2(z+r)^2} \right) \quad (41)$$

In Equation (41) r is the radius of the asperities and D is the diameter of the particles.

Later Rabinovich et al. [53] employed the root-mean-square (rms) roughness in the Hamaker expression to include a parameter which is characteristic of the particle surface roughness on the whole. They also found it necessary to include a parameter for the distance between asperities on the surface λ .

$$F_{Rabin.}(z) = \frac{AD}{12z^2} \left(\frac{1}{1 + \frac{29.07Drms}{\lambda^2}} + \frac{1}{\left[1 + \frac{1.82rms}{z}\right]^2} \right) \quad (42)$$

From these studies it is apparent that intimate details of the surface geometry are needed to accurately calculate the adhesion force from theory.

D Capillary forces in moist granular materials

The presence of a small amount of liquid can have a considerable influence on the bulk properties of granular matter. It is the reason why otherwise free-flowing sand can be shaped and molded into ornate sand castles. Granular materials become cohesive when wet due to liquid bridges that form between close particles. Particles connected by a liquid bridge resist being separated. Experimental studies of the effect of moisture on the angle of repose [54] show that both the surface tension and the viscosity of the liquid can have a significant effect on the behavior of the resulting moist granular material.

Addition of capillary forces to particle dynamics Lian et al. [55] have created a detailed theoretical model for the capillary forces caused by a liquid bridge between two rigid particles. The model has been applied in particle dynamics simulations to investigate the cohesive behavior of moist granular materials. In the model, the force between particles includes a contribution from both the surface tension of the fluid and from the pressure difference across the air-liquid interface.

$$F_s = 2\pi R\gamma \sin^2 \beta \quad (43)$$

$$F_h = \pi R^2 \Delta P \sin^2 \beta \quad (44)$$

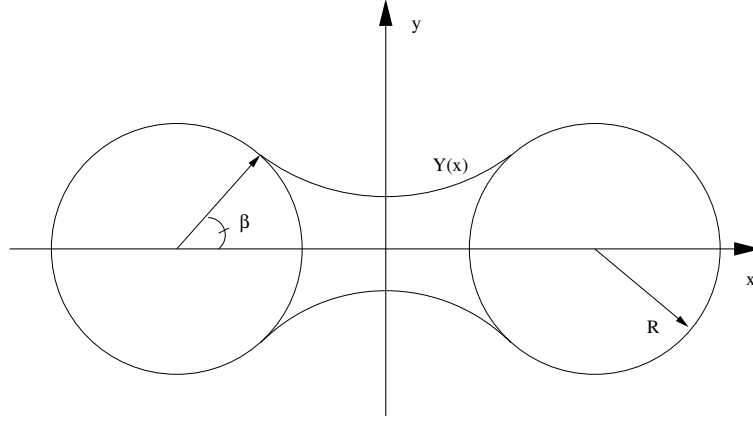


Figure 1.9: *A liquid bridge between two particles*

Where γ is the surface tension of the liquid and β is the liquid/solid contact angle as shown in Figure 1.9. The sum of these components can be rearranged to give

$$F_c = 2\pi R\gamma \sin^2 \beta \left[1 + \frac{R\Delta P}{2\gamma} \right] \quad (45)$$

The capillary force can be calculated if the geometry of the liquid bridge is known, and the geometry can be obtained from the Laplace-Young equation, with X and Y defined in Figure 1.9.

$$\frac{2R\Delta P}{2\gamma} = \frac{(d^2Y/dX^2)}{1 + ((dY/dX)^2)^{3/2}} - \frac{1}{Y(1 + Y^2)^{1/2}} \quad (46)$$

where Y is the position of the gas-liquid interface.

McCarthy et al [56] have used and expanded the model created by Lian in particle dynamics simulations to investigate various mixing [57] and segregation [58] problems involving moist granular material. Cohesion due to moisture can mitigate size segregation, but particles with differences in their contact angles can be made to segregate because of their adhesive differences [59]. McCarthy has defined some dimensionless numbers to capture the phase space of when mixing or segregation may occur as a function of differences in particle size and cohesivity. Phase diagrams for cohesive particle mixing and segregation have been constructed based upon their dimensionless numbers.

V Origins of friction and laws across length scales

In the past decade many of the atomic origins of friction have been uncovered. The laws of friction on length-scales near to the atomic level are different than those observed on the macroscopic scale. Discovering what properties and events on the atomic scale cause the observable Coulomb's laws of friction on the macroscopic scale has been a recent topic of research [60]. In fact much headway has been made to uncover these atomic origins of friction. This effort has led to the discovery that the traditional laws of friction are not valid on the atomic length scale. The original laws were probably first formulated by Leonardo da Vinci (1452-1519) when he observed that the same force is required to keep a rectangular block sliding regardless of which of its faces it is resting on. However, da Vinci never published his findings, so about 200 years later Guillaume Amontons rediscovered them and made the ideas public. Charles de Coulomb also contributed, for which the set of laws commonly bear his name.

Coulomb's laws of friction Coulomb's laws of friction are now well known and are often phrased in three simple statements (Compare these statements with Equations (10) and (11)).

- The friction force that resists sliding is proportional to the normal load. The proportionality constant is called the coefficient of friction.
- The magnitude of the friction force is independent of the area of contact.
- The friction force is independent of sliding speed (once the sliding starts).

These laws were derived solely from macroscopic observations. Over the years several premature attempts were made to fundamentally explain these observations. However, it wasn't until recently that tools were developed that were able to create controlled friction environments. These tools made headway towards discovering the atomic origins of friction. These tools include: the atomic force microscope, quartz crystalline micro-balance, surface forces apparatus, and computer simulation with atomic level detail [61]. These methods show friction in a way that does not obey Coulomb's laws. Some new laws have been proposed to describe how friction behaves on the atomic scale.

Friction on the atomic scale

- The friction force is proportional to the actual area of contact.
- The friction force is directly proportional to the sliding speed of the interface at the true contact points, as long as the surfaces do not heat up [62].
- The friction force depends on the adhesion hysteresis; the relative ease with which two surfaces can become stuck compared to becoming unstuck. Friction is proportional to the degree of irreversibility of the force that squeezes the two surfaces together, rather than the outright strength of the force [63].

These findings have also led to a mechanism for friction on the atomic scale. As surfaces slide, the atomic interactions between the surfaces cause the atoms to vibrate. The vibrations are nothing more than sound waves, which are sometimes called phonons. The phonons travel into the materials where they are distorted into heat. Energy from the sliding surface is transferred into heat and that is why it takes more mechanical energy to keep the surfaces sliding.

Mesoscale factors to friction The apparent discrepancy between Coulomb's laws and atomic scale friction must be resolved by the mesoscale. As in the case of adhesion, surface roughness plays a large role. Take for example the opposing statements that friction is proportional to the contact area on the atomic scale, but independent of the contact area on the macroscale. The paradox is solved by distinguishing the apparent area of contact from the true area of contact. Surface roughness causes the true area of contact to be only a small fraction of the apparent area of contact at the macroscale. Surface roughness allows the true area of contact for macroscopic solids to be proportional to the normal load, and not the apparent area of contact. That is how da Vinci's rectangular block has the same friction force no matter which face it rests on.

VI Fine powders (micro and nano)

Microparticles The behavior of particles in the micrometer range can be heavily influenced by both inter-particle adhesive forces and viscous forces caused by the interstitial fluid. These forces

are routinely dealt with by those operating fluidized beds. Gas flowing up through a column packed with a granular material can display a variety of fluidization behavior depending on the particle size, density, and adhesive forces. Fluidized beds are commonly used in chemical reactors, the most recognizable of these is the catalytic cracker in a fuel refinery. Geldart [64] has classified the behavior observed into four groups with the letters A-D and characterized the particle properties important to obtaining each of these four behaviors. Qualitative observations are made about the behavior of a fluidized bed made from granular materials of each type. e.g. Bed expansion, bubble formation, amount of mixing in the bed, and speed of bed collapse after the gas flow is shut off.

Another significant source of information on the behavior of particles on the micrometer length scale comes from the work of Castellanos et al. [65–69]. The particles in their studies are micrometer sized printer toner particles. They report many characteristics of the behavior of particles on this length scale by studying the powder in rotating drums and shear geometries. The behavior of their particles clearly reflect the influence of van der Waals adhesion between particles and viscous forces from the ambient air. For example simply tumbling the powder in a rotating drum causes the whole system to fluidize.

Nanoparticles The current boom in nanotechnology is producing particles on the nano scale in increasing volume and variety. Adhesion typically dominates the behavior of particles on this length scale causing widespread agglomeration. The small size of these particles makes it relatively difficult to study many details of the powders experimentally, so particle dynamics simulations have much to contribute.

With the appropriate particle properties and force models, systems of nanoparticles can be studied in a detailed fashion. Modeling the significant forces is different on the nanoscale from the macro and even the micro scale. For instance, in addition to adhesion during contact, van der Waals forces are significant between particles separated by distances of up to several particle diameters. To continuously model adhesion between particles before and during contact, there needs to be a way to combine the Hamaker expression with JKR theory. This is explained in detail in Chapter 4.

The contact mechanics for nanoparticles may also be different from the theories governing the macroscale. The nano scale friction laws discussed in the previous section should be applied to the contact mechanics of the particle dynamics simulations to accurately model this. Where theory has not yet been developed, relationships may be obtained empirically. Experimental devices such as the atomic force microscope are enabling the manipulation of nano particles and measurement of nano contact forces. These studies can provide the particle properties and force models to accurately model nano mechanics [70–73].

VII Organization of the dissertation

The topics discussed in this introduction provide the necessary background to simulate a number of granular phenomena using particle dynamics simulations. By accounting for the important forces between particles of varying sizes, particle dynamics simulations can connect the inter-particle behavior to bulk granular behavior. The rest of this dissertation discusses simulation efforts to model the effects of friction and adhesion in granular matter.

The chapters are generally in order of the length-scale considered, starting from the largest. Chapter 2 is a study of how nanoscale surface roughness affects the macroscopic flow of millimeter sized particles in a rotating drum. Chapter 3 proposes a theory which connects surface forces in a binary mixture of particles to the bulk properties of the mixture, both friction and adhesion are applied which suggests the application to micrometer sized particles. Chapter 4 develops a particle dynamic model suitable to capture the energy dissipated in adhesive contacts and proposes how to design a mechanical damping device to take advantage of energy dissipation due to adhesion hysteresis. Chapters 5 and 6 report work on the molecular level. They discuss Monte Carlo simulations of alkane models which are used to calculate adsorption behavior. Alkanes can be viewed as a model lubricant. Adsorption being an important mechanism involved in lubrication failure. Finally chapter 7 draws conclusions from these studies and recommends future work in this area to better understand the connection between surface forces and the behavior of granular matter from a molecular level all the way up to macroscopic phenomena.

Nanoscale variations in the surface roughness of individual particles affect macroscale granular flow characteristics. Experiments were conducted in circular rotating tumblers with smooth and rough 2 and 3mm steel particles. The angle of repose for rough particles increased by 10 to 25 degrees over that of smooth particles. Even though surface roughness affects the angle of repose, segregation was not detected in mixtures of rough and smooth particles. For mixtures of smooth and rough particles, the angle of repose increased monotonically with increasing concentration of rough particles. Particle dynamics simulations verified that the dependence of the angle of repose on the concentration of rough particles can be directly related to the coefficient of friction of the particles. Simulations over a broad range of friction parameters also failed to induce segregation. These results indicate that nanoscale surface roughness can affect the flow ability and angle of repose of granular matter without driving de-mixing of the bulk granular material.



Surface Roughness Effects in Granular Matter

I Introduction

The nature of surface roughness and its influence on granular mixing and flow is a subject that has received little attention in granular flow studies. In most experiments, the surfaces of individual particles, typically spherical, in the flowing medium are implicitly assumed to be nominally “smooth.” However, this characteristic is rarely quantified. Due to the extraordinary number of contacting surfaces between discrete particles and because granular particles slide and roll with respect to one another when they flow, it is apparent that tribological effects can potentially play a major role in granular flow.

In general, it has been implicitly assumed that nanoscale surface effects are orders of magni-

tude less important than macroscopic properties such as particle size and density in granular flow. However, the coefficient of friction, a macroscale parameter, is often adjusted in discrete element modeling to produce significant changes in the granular flow characteristics [74–76]. Likewise, the experimentally determined angle of repose of a bulk material increases as the interaction friction is increased [77]. In fact, the conceptual relevance of the coefficient of friction to the angle of repose of a granular pile can be related to the simple problem of a block sliding down an inclined plane [78]. Of course, the macroscopic coefficient of friction merely reflects the multiple nanoscale surface interactions in granular flow.

Only a few researchers have attempted to quantify microscopic surface interactions between individual granular particles. For example, measurements indicate that surface properties influence the normal and tangential compliance of materials in both micro-slip and the gross sliding limit of friction [79]. More recent experiments coupling atomic force microscopy and annular shear cell tests focused on relating tribological properties to macroscale effects by introducing lubricants into a granular bulk of glass beads [80].

At a macroscopic scale, quasi-2D rotating drums, like that shown in Figure 2.1, are often used to study the characteristics of flowing granular materials [81–84]. Typically, a cylinder is filled to 50% volume fraction with granular material and rotated about its axis causing the material to tumble down the angled free surface in a thin flowing layer. Upon reaching the end of the free surface, the material is trapped in near solid body rotation with the drum until it reaches the free surface again. Such tumblers provide a convenient means to measure the dynamic angle of repose. Moreover, quasi-2D and 3D rotating drums are often used to study granular segregation. Two initially well-mixed materials having different properties (such as size or density) tend to unmix leading to the classical radial segregation pattern in a quasi-two-dimensional tumbler [78, 85–87] and bands of segregated material in a three-dimensional tumbler [88–90].

The focus of this paper is the relation between the friction due to the nanoscale surface roughness of a granular material and the macroscale granular flow properties. In particular, we consider the angle of repose for pure smooth or rough spherical particles as well as mixtures of these particles. As we shall demonstrate, surface roughness affects the dynamic angle of repose in rotating

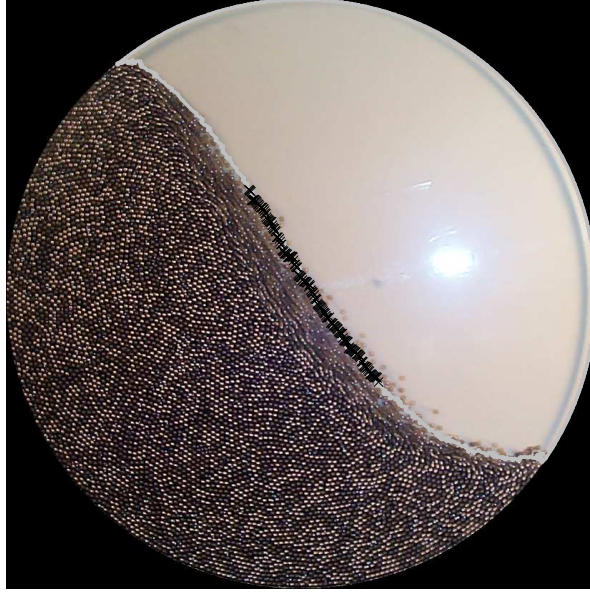


Figure 2.1: Single image of the quasi-2D rotating drum with 50% rough concentration of 2 mm particles at $Fr = 6.07 \times 10^{-3}$. A gray curve indicates the surface of the flowing layer from the ten ensemble averaged images and black \times 's show the middle 40% of the tumbler diameter.

tumblers. And the angle of repose is widely believed to be a predictor of segregation. Is this, however, the case? To this end, we evaluate the tendency toward mixing or segregation of particles with differing surface roughnesses in quasi-2D and 3D tumblers. In addition, we use particle dynamics simulations to further evaluate the influence of imposed friction characteristics on granular flows.

II Experimental approach

A Chrome steel beads and their tribological characteristics

Spherical chrome steel beads (AISI 52100 Standard, Grade 1000, Fox Industries) having diameters of 2.37 mm (which we denote 2 mm) and 3.18 mm (3 mm) to within ± 0.01 mm were used in the experiments. Using smaller beads would have made the surface roughness measurements difficult and permitted electrostatic forces to interfere with the tumbler experiments described shortly. The new beads were shiny with a hard surface (62-65 on the Rockwell “C” scale). Rock polishing

lapidary equipment (Lortone 3A Rotary Tumbler with super-coarse 46/70 silicon carbide grit) was used to roughen half of the beads. The rolling motion of the grit against the beads pitted the surface creating pock marks and eliminating the original shiny surface without altering the spherical shape or the diameter of the particles. The other half of the beads were used in their smooth, shiny state.

After cleaning the beads to remove the silicon carbide grit, the nanoscale surface profile of the beads was measured using a white light phase-shift interferometer (*ADE Phase-Shift MicroXAM*). The surface profile for a new smooth particle, shown in Figure 2(a), is quite smooth with only a few short asperities. The surface profile of a rough particle, shown in Figure 2(b), has many

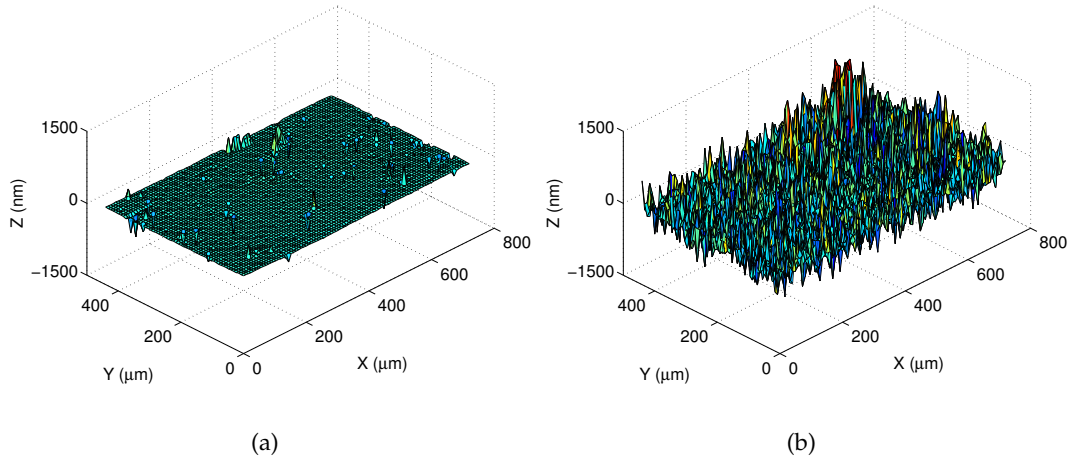


Figure 2.2: Typical surface profile for 2 mm particles for (a) new material and (b) after roughening.

more asperities, nearly all having much larger magnitudes than those of the smooth bead. The surface roughness, R_q , of the material is defined as the standard deviation of the measured height. Only a small portion of the bead surface ($\approx 800 \mu\text{m} \times 600 \mu\text{m}$) can be measured at one time, so multiple measurements on a single bead were used to verify that the measured surface roughness was equivalent over the entire surface. The surfaces of at least 35 particles per lot of material were measured with the averaged surface roughness results given in Table 2.1 for a typical lot of the new and roughened beads. Even with the extraordinary hardness of the base material, there was some degradation in the surface roughness after the beads were tumbled in a rotating drum, as

Table 2.1: Typical surface roughness (R_q) of beads used in experimentation (all roughness values are in nanometers).

	Ball Size			
	2 mm		3 mm	
	New	Roughened	New	Roughened
Pre-Test	26±9	235±29	59±11	244±31
Post-Test	31±10	160±34	57±13	174±30



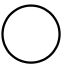

is evident in the change in the roughness from the “Pre-Test” values to the “Post-Test” values for the roughened particles. Most likely, plastic deformation occurred due to the asperity interactions of the rough surfaces when particles collided. The decay of the surface properties was limited by keeping the total number of revolutions of the tumbler to less than 400.

The macroscale friction characteristics of the granular particles were measured in three ways: a scratch test, acceleration of sliding particles down an angled slope, and the critical angle to cause particles at rest to start sliding.

A standard tribological scratch test determines the dynamic coefficient of friction via the ratio of drag force to the applied normal force. A CETR Tribometer held a single 3 mm bead at a constant normal force on a flat disk and measured the transverse force while the bead was slid without rolling at a constant velocity across the disk. Due to their small size, 2 mm beads could not be tested in this apparatus. Table 2.2 reports the mean and standard deviation of at least six measurements of the coefficient of friction. The schematics in the “Surface Condition” column show the surface roughnesses of the spherical particles and the flat surfaces (the relative surface heights are not to scale). The shading in the “Friction Intensity” column provides a visual indication of the relative magnitudes of the coefficient of friction with black showing $\mu = 0.5$ and white indicating a frictionless sliding contact. Rough particles tested on a machine ground flat steel surface ($R_q = 544$ nm) had a higher coefficient of friction than smooth particles on the same surface, as expected, but the coefficient of friction depended on the normal force. When the particles were tested on a flat steel surface polished to a mirror finish ($R_q = 29$ nm), the coefficient of friction was higher for the smooth particles than for the rough particles, especially at higher normal forces.

Although these results seem counterintuitive, they are consistent with the theory of tribologi-

Table 2.2: Mean of the coefficient of friction for six tests of 3 mm rough and smooth particles on a machine ground surface and a polished surface. (Surface roughness of the beads is different from Table 2.1 due to different lots of material.)

Surface Condition	Normal Force (mN)	Coefficient of Friction (μ)	Friction Intensity
$R_q = 235$ nm  $R_q = 544$ nm	49	0.22 ± 0.03	
	147	0.19 ± 0.03	
	245	0.15 ± 0.01	
$R_q = 235$ nm  $R_q = 29$ nm	49	0.26 ± 0.05	
	147	0.23 ± 0.03	
	245	0.28 ± 0.07	
$R_q = 56$ nm  $R_q = 544$ nm	49	0.11 ± 0.01	
	147	0.12 ± 0.01	
	245	0.11 ± 0.01	
$R_q = 56$ nm  $R_q = 29$ nm	49	0.27 ± 0.02	
	147	0.44 ± 0.03	
	245	0.48 ± 0.03	

cal surface interaction. Macroscale friction is a function of the normal force between two surfaces, not the area of contact. However, when the contact area is significantly reduced, such as in near single point contact between a sphere and a flat surface, the nature of the contact becomes critically important. The rough beads probably have a higher coefficient of friction on the machine ground flat surface than the smooth beads because a greater number of asperities are in contact between the two surfaces, requiring a greater tangential shear necessary for relative motion. The reduction in the coefficient of friction for the rough particles on the same surface with an increasing normal force is likely a result of plastically deforming the asperities. The smooth bead on the machine ground flat surface reduces total asperity contact, and the corresponding coefficient of friction is less. The smooth particle on a polished flat surface results in a remarkable increase in the coefficient of friction compared to the cases where at least one of the surfaces is rough. This is likely due to the increased stiction between the two surfaces due to the lack of asperity interaction on the microscale level.

The minimum normal force available in the CETR Tribometer corresponds to weight of more

than 37 particles (the weight of a single bead is 1.3 mN), which is much larger than the total depth of the flowing layer in a typical tumbler experiment, usually 7-10 particles. Therefore, two other methods having contact forces generated by the mass of individual particles were used to characterize the coefficient of friction. In the first case, the dynamic coefficient of friction was measured based on the acceleration of sliding particles on a sloped flat surface. In order to prevent rolling and maintain a sliding contact, a tripod of three 3 mm particles was bonded together with an adhesive. The tripod was released on a flat surface tilted at a known angle θ with respect to horizontal, and its motion was recorded with a digital video camera. Assuming a constant acceleration, the coefficient of friction was calculated as $\mu = \tan(\theta) - \frac{2A}{g \cos \theta}$, where A is the coefficient of the squared term in a parabolic fit to the position of the tripod with respect to time. The smooth and rough plates were made of AISI 52100 chrome steel, the same alloy as the particles, so as to mimic particle-to-particle interactions in a granular flow. Acrylic was also used as a flat surface to characterize contacts between particles and the material of the drum walls. Results averaged over thirty or more trials of every combination of surface-bead contacts are reported in Table 2.3 (the transparent acrylic surface is schematically represented by a dashed line).

Table 2.3: Average and standard deviation of the coefficient of friction from at least thirty runs of tripods sliding down a flat surface. The surface roughness is the average over the three particles of the tripod.


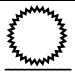
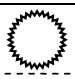

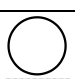
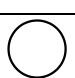








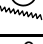















Surface Condition	Coefficient of Friction (μ)	Friction Intensity
 $R_q = 235 \text{ nm}$ $R_q = 304 \text{ nm}$	0.16 ± 0.02	
 $R_q = 235 \text{ nm}$ $R_q = 23 \text{ nm}$	0.35 ± 0.07	
 $R_q = 235 \text{ nm}$ $R_q = \text{N/A}$	0.44 ± 0.02	
 $R_q = 56 \text{ nm}$ $R_q = 304 \text{ nm}$	0.14 ± 0.01	
 $R_q = 56 \text{ nm}$ $R_q = 23 \text{ nm}$	0.25 ± 0.02	
 $R_q = 56 \text{ nm}$ $R_q = \text{N/A}$	0.35 ± 0.07	

Table 2.4: Critical angle to initiate the sliding of a tripod of particles. At least sixty trials were conducted for each particle size and surface roughness combination. The surface roughness is the average over the three particles of the tripod.

Flat Surface	Mirror Polish R _q = 23 nm		Machine Ground R _q = 304 nm		Acrylic Transparent	
Particle Size	2 mm					
Particle R _q (nm)	34.1 	250.8 	55.5 	168.5 	33.6 	277.8 
Sliding Angle	11.4°±2.0° 	21.6°±7.5° 	12.8°±2.0° 	16.8°±4.4° 	28.2°±8.1° 	33.8°±6.8° 
Particle Size	3 mm					
Particle R _q (nm)	59.3 	284.2 	43.4 	246.0 	37.9 	343.8 
Sliding Angle	16.3°±3.3° 	23.4°±6.3° 	12.4°±2.0° 	15.2°±3.5° 	27.2°±6.9° 	29.9°±4.5° 

The results match intuition that rough particles have a higher coefficient of friction. However, it is interesting to note the factor of two increase in the coefficient of friction as the chrome steel flat surface changes from the rough machine ground to the smooth mirror finish. Again, it appears that the lack of asperities on the mirror polished surface results in a greater number of contacts between the surface causing an increase in the measured coefficient of friction.

Finally, the static friction was characterized by measuring the critical angle of a flat surface that induces motion of a particle tripod set. The experiment was conducted by placing a tripod on a horizontal flat surface which was then tilted very slowly ($1.5^\circ/\text{sec}$) until the tripod began sliding. The average angle that initiated the sliding motion averaged over at least 60 trials is reported in Table 2.4. The schematics in each column represent the relative surface roughness between the particles and the flat surface, which are oriented at the angle that sliding occurred for that particle and flat surface combination. In this case, the 2 mm particles were also evaluated. The key result is that the critical sliding angle increases for all cases when the surface roughness of the particles changes from smooth to rough. The large standard deviation is indicative of the difficulty in obtaining repeatable measurements.

All three methods of characterizing friction suggest that increased surface roughness of particles generally causes a corresponding increase in the observed friction, although exceptions occur depending upon the roughness of the flat surface. It is clear that quantifying and obtaining consistent values of the macroscale friction based on the surface roughness of contacting surfaces for

individual particles is quite difficult.

B Rotating tumbler

The collective effect of the surface roughness of many particles on granular flow was measured using a quasi-2D tumbler with a diameter of $2R=28$ cm and a thickness of $2.8d$, where d is the particle diameter (the thickness was adjusted according to the particle size). These dimensions were chosen to provide a large drum diameter to particle diameter ratio, $2R/d$: 118 and 88 for $d=2$ mm and 3 mm, respectively. The thickness of the quasi-2D tumbler was necessarily small to reduce the quantity of particles that were used. This was particularly important due to the cost of the particles, which could only be used for a limited time because the surface properties changed with use, as indicated in Table 2.1. The front and back plates of the tumbler were 6.4 mm thick, clear, static-dissipative acrylic allowing visualization of the free-flowing surface and measurement of the angle of repose. The surfaces of the acrylic were electrically grounded to minimize electrostatic charge build-up in the tumbler.

The dynamics of the flow in a rotating drum are governed by the Froude number [78], $Fr = \frac{R\omega^2}{g}$, where ω is the rotational speed and g is the gravitational acceleration, which represents the ratio of centrifugal to gravitational forces acting on the particles in the drum. By changing the rotational speed, the Froude number was varied from 10^{-5} , just fast enough so that the flow was continuous (not avalanching), to 1.5×10^{-2} , which was well into the cataracting regime of flow. The tumbler rotation was controlled with a brushless stepper motor and a micro-step driver with input control to the driver via a computer controlled square wave generator. In all cases, the fill level of the drum was 50%.

To measure the dynamic angle of repose β_d , ten high resolution digital images of the rotating tumbler were obtained at each Froude number. The drum was stopped while the images were downloaded in order to reduce wear of the particle surfaces. The motor was then accelerated from rest to the next Froude number. The intensity from ten digital images for each Froude number were ensemble averaged and, after eliminating the extraneous background via image processing, the surface profile of the flowing granular material was located with an edge-find function, pro-

ducing results like that shown in Figure 2.1. Only the central 40% of the edge, evident as the dark \times 's near the surface, was used for the linear fit to determine the dynamic angle of repose, thus avoiding the curved free surface near the periphery of the tumbler.

III Experimental results

A Mono-disperse angle of repose

To begin, we report the dynamic angle of repose, β_d , of mono-disperse smooth and mono-disperse rough particles. For the smooth 2 mm particles, the angle of repose was 26.2° at $Fr = 2.0 \times 10^{-4}$. The smooth 3 mm particles at the same rotation rate had a lower dynamic angle of repose of 23.4° . The higher angle of repose with decreased particle size is consistent with previous results [81]. When the contents of the drum were changed to rough 2 mm and 3 mm particles, the angles of repose increased to 43.4° and 31.1° , respectively, for the same Froude number, clearly indicating that the angle of repose of a bulk material is directly related to the surface roughness of the individual particles. Most likely, interlocking asperities result in greater sliding and rolling friction between rough particles than for particles having smooth surfaces so that rough particles pile up at a higher angle before gravity can overcome the inter-particle friction.

After the experiments, the surface roughness of the particles was measured to determine the wear due to tumbling, with the results given for the mono-disperse rough and smooth systems in Table 2.1. The surface roughness of the smooth particles was within a standard deviation of the pre-tumbled particles. The “smoothing” of rough particles was much greater with a decrease between 24% and 34% from the initial surface roughness. The difference in wear between rough and smooth particles can be attributed to greater plastic deformation of the taller asperities of the roughened particles due to collisional impact.

B Do different angles of repose cause segregation?

One of the interesting aspects of granular flow is the segregation of poly-disperse material. For instance, in a quasi-2D tumbler, radial segregation occurs with small or dense particles gathering

at the center of the fixed bed and the remaining material near the periphery [78]. The radial segregation can be explained in terms of percolation, where the smaller particles fall through the voids in the lattice of larger particles, or buoyancy, where more dense particles sink to lower levels in the flowing layer [86,91].

A theoretical approach to predicting segregation is based on the angle of repose of each member of a bi-disperse system, regardless of particle size or density. For instance, a cellular automata model predicts that radial segregation can occur in rotating drums when two distinct particles fall at different angles of repose due to the individual particle friction [92].

Given these models for radial segregation based on particles with different angles of repose, and that pure rough and smooth beads exhibit different angles of repose, we attempted to find a situation in which the rough and smooth particles segregated. However, no radial segregation was observed for the bi-disperse (smooth and rough) mixtures in the quasi-2D tumbler for Froude numbers ranging from 3.9×10^{-7} to 1.5×10^{-3} , an example of which is shown in Figure 2.1. Even when the materials started in an unmixed state (each material filling a sector of the drum), the two species mixed thoroughly. In addition, there was no preferential neighboring of rough or smooth particles based on analysis of the connectivity of smooth-to-smooth or rough-to-rough particles after a few rotations of the system. Thus, it appears that differences in surface roughness characteristics alone cannot cause radial segregation, even though the angles of repose of the two species differ substantially.

In three-dimensional situations, either long cylinders or spherical containers, bands of segregated material spontaneously form and then coarsen due to differences in particle size [88–90,93,94]. The differing angles of repose for the two components of a bi-disperse mixture is key in the explanation of how bands are produced in three dimensional experiments [95,96]. This mechanism is predicated upon a radial core preceding the formation of enriched bands of particles that are observed in axial segregation.

We also performed experiments in 3D (spherical) and 2D+1 (cylindrical) granular systems to explore the potential for banding of rough and smooth particles given their differing angles of repose. In a 3D spherical container with a diameter of 35 particles, rotation of a mixture of rough

and smooth particles at 50% volume fraction over 10 hours at a Froude number of 6×10^{-3} to generate a continuous, flat flowing layer resulted in no banding. A similar test in a half-filled cylinder with a 76.2 mm diameter (32 particles) and 185 mm length rotated at $Fr = 6.1 \times 10^{-3}$ also did not produce segregated bands over a test run of 72 hours. In fact, starting with one-half of the length of the tube half-filled with rough particles and the other half with smooth particles only produced diffusion of the rough and smooth particles rather than maintaining axial segregation. There was a clear difference in the angle of repose between the two different materials. However, this did not prevent the mixing of the two particle types. Thus, while the surface roughness can change the angle of repose of the bulk material, this characteristic alone does not appear to be a sufficient condition for segregation, at least for the conditions used in this study. This further suggests that radial segregation as a result of percolation or buoyancy is a necessary precursor to axial segregation and subsequent axial banding.

C Angle of repose of bi-disperse mixtures

Although the difference in the angles of repose of the smooth and rough beads does not cause segregation, it may alter the nature of the granular flow for bi-disperse mixtures of smooth and rough beads. Hence, the dynamic angle of repose was measured as a function of Froude number for a variety of mixtures of smooth and rough 2 mm and 3 mm beads at concentrations ranging from 0% rough to 100% rough as shown in Figure 2.3. To assure that the measured angle of repose was related to the Froude number and not a result of the changes in the surface roughness of the beads due to wear, the measurements were conducted by increasing the rotational speed to obtain data for every other Froude number in Figure 2.3. Then, the remaining data were obtained by decreasing the rotational speed. In addition, multiple data points at the same Froude number identify rotational speeds that were re-tested in order to verify the repeatability of the measurements. Although there was a measurable decrease in rough particle surface roughness during an experiment, as indicated in Table 2.1, the angle of repose remained only a function of the concentration of rough particles and the Froude number.

The results in Figure 2.3 show that the angle of repose increases with increasing Froude num-

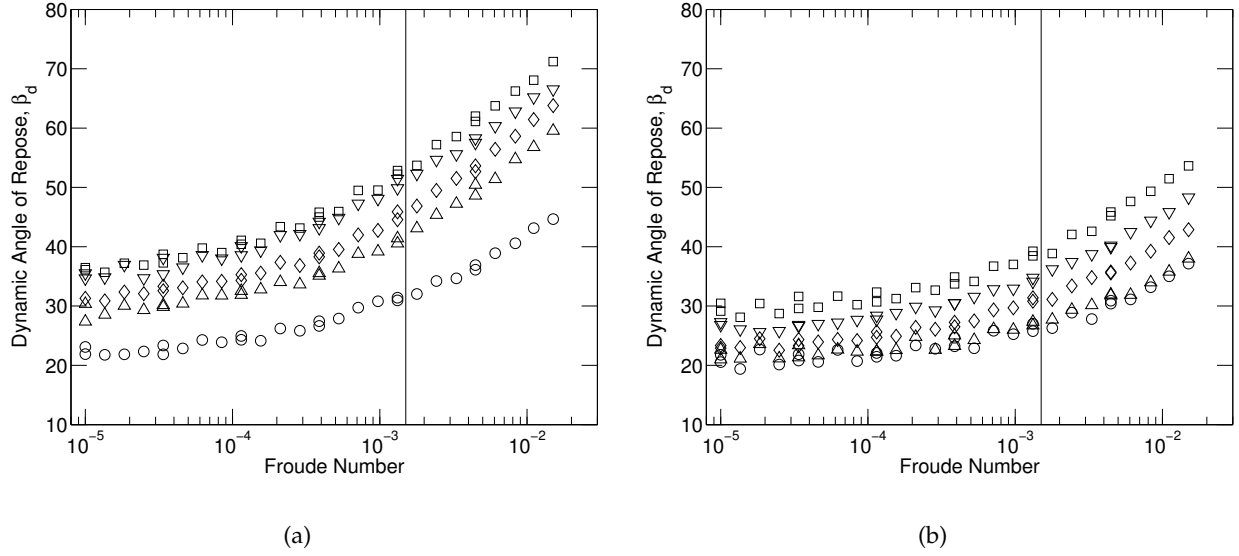


Figure 2.3: Angle of repose as a function of Froude number for (a) 2 mm and (b) 3 mm beads for different concentrations of rough particles; \circ = 0% rough concentration, \triangle = 25% rough, \diamond = 50% rough, ∇ = 75% rough, and \square = 100% rough.

ber, consistent with previous results [81], regardless of particle size or rough particle concentration. Above approximately $Fr = 1.5 \times 10^{-3}$ (marked by the vertical lines in Figure 2.3), the free surface becomes curved indicating a transition to the cataracting regime of flow. More importantly, the angle of repose increases as the concentration of rough particles increases, which is shown more clearly in Figure 2.4. At low Froude numbers, the angle of repose for the 2 mm beads increases by about 15° as the concentration changes from purely smooth to purely rough particles. At higher Froude numbers, the change in the angle of repose as the concentration of rough beads increases is even larger, greater than 25° at the highest speed. The changes in the angle of repose from one concentration to another at the same Froude number are somewhat less for the 3 mm beads, particularly when the rough particle concentration changes from 0% to 25%. The difference may be a consequence of the surface roughness of the smooth beads. Table 2.1 indicates that the smooth 2 mm particles had a smaller surface roughness than the smooth 3 mm particles. It is possible that small concentrations of rough particles with very smooth particles may have more influence on the angle of repose than when the smooth particles are not quite as highly polished. It

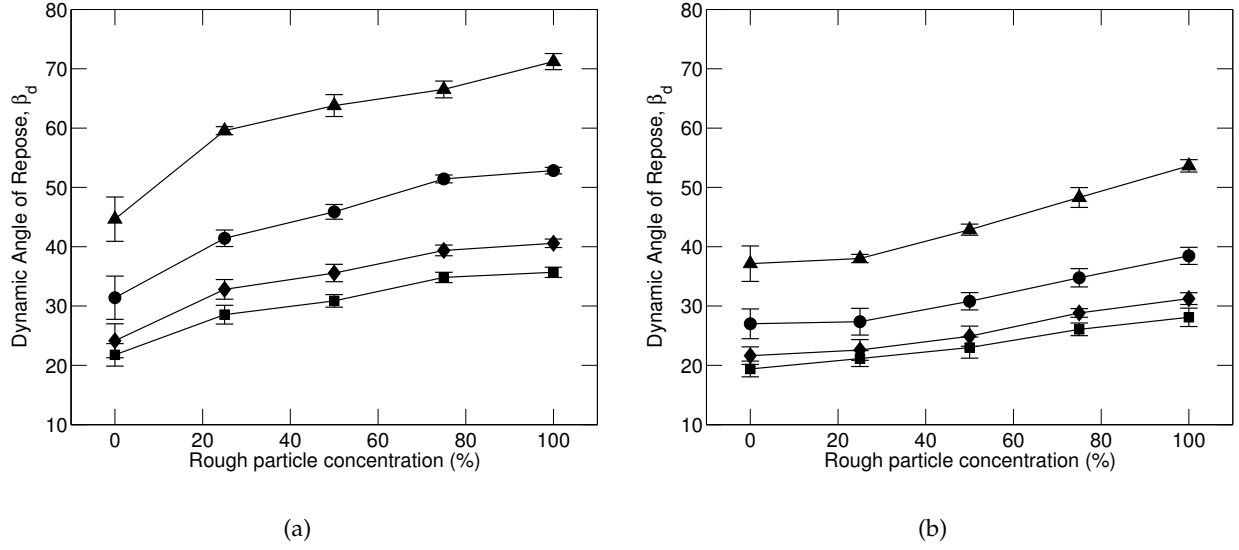


Figure 2.4: Angle of repose as a function of concentration of rough particles for (a) 2 mm and (b) 3 mm beads for different Froude numbers; ■ $Fr = 1.4 \times 10^{-5}$, ◆ $Fr = 1.6 \times 10^{-4}$, ● $Fr = 1.3 \times 10^{-3}$, ▲ $Fr = 1.5 \times 10^{-2}$. Error bars represent the standard deviation for the angle of repose measurement for ten individual images.

is also evident that the angle of repose is greater in all cases for the smaller beads than for the larger beads, consistent with previous results [81]. Figure 2.4 also indicates the variability of the angle of repose measurement when individual images are used rather than ensemble averaging the raw image intensity. The largest standard deviation occurs for the 0% rough concentration. The shiny appearance of the smooth particles makes it difficult for the edge-find function to differentiate between the free surface of particles and the background in an individual image. Otherwise, the standard deviation is independent of the Froude number or concentration of rough particles.

Besides surface roughness, other microscopic forces can influence the angle of repose for granular flow. For instance, electrostatic attraction forces between the walls and the particles can increase the angle of repose. Furthermore, particle impacts induce magnetic properties in the steel beads that can cause small attraction forces between particles. As a precaution, prior to all experimental runs the beads were passed through an oscillating magnetic field to minimize the induced magnetic attraction between particles. Surprisingly, the thickness of the acrylic end plates also affected the angle of repose. Increasing the thickness of the acrylic end plates from 6.4 mm to 9.5 mm

caused an increase of $3\text{--}4^\circ$ in the angle of repose for otherwise similar conditions. This may be a result of a slight decrease in the axial drum length as the thicker cover plate flexed outward less due to the axial pressure of the fixed bed of steel beads. Further tests verified that increasing t/d from 2.8 particles to 5 and 7 resulted in a decrease in the measured angle of repose, consistent with previous results in a granular heap flow [97–99] and rotating tumbler flow [100]. Nevertheless, the trend of increasing angle of repose with increasing concentration of rough particles occurred regardless of the value of t/d . Thus, the surface roughness is the primary factor causing a change in the angle of repose of granular flow for the results shown in Figures 2.3 and 2.4.

IV Simulation of particles with varying friction

Particle Dynamics (PD) simulations have been shown to accurately capture many aspects of granular materials in a rotating tumbler [83, 101], including segregation of bi-disperse particles [102–107]. Here PD simulations have the advantage over experiments in that the method provides precise control over the factors influencing the particle contact allowing the isolation of the causes of flow behavior. In this way, the difficulty in measuring the coefficient of friction between rough-smooth surfaces and rough-smooth particles can be circumvented by simply assigning different friction characteristics to two classes of particles in the simulations.

The simulation consisted of solving the fundamental equations of motion for each particle given the normal and tangential forces, f_n and f_t , being applied by other particles in contact [102]. The parameters of the particle interaction were the spring stiffness in the normal and tangential directions, k_n and k_t , the damping of particle velocity after contact, k_d , and the coefficient of friction between sliding surfaces, μ . The normal forces were modeled via Hertzian overlap [108], while the tangential force was computed as the minimum between (1) the product of the normal force and the coefficient of friction ($f_n\mu$) or (2) the restoring force from the tangential spring and lateral displacement ($k_t\delta$). The free moving granular particles were constrained in a circular boundary of particles that held a fixed radial position but rotated as an entire ring at a specified rotation rate. The simulated tumbler had a diameter of 40 particles and a rotation rate of 1.05 revolutions per minute producing a Froude number of 4.94×10^{-5} . Periodic boundary conditions were assumed

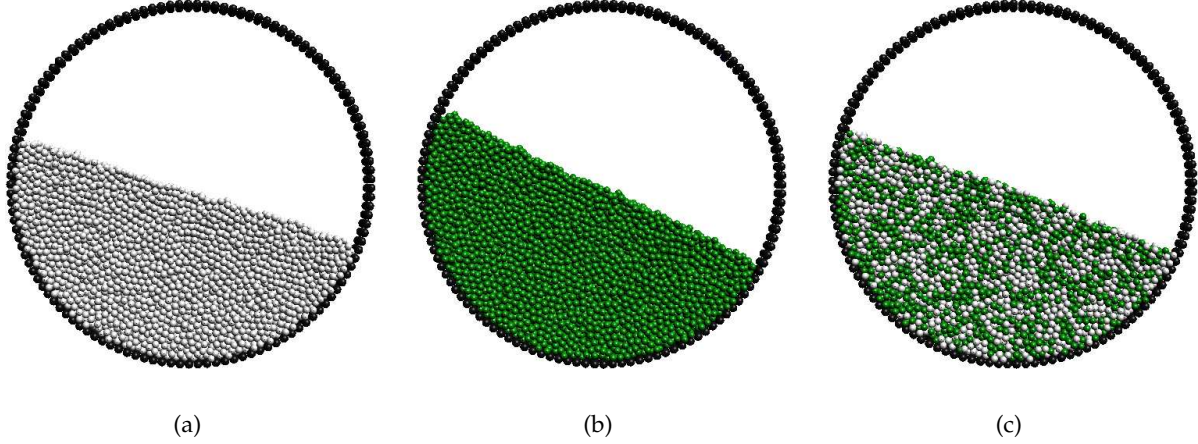


Figure 2.5: Single instances of the PD simulations for the following friction conditions: (a) $\mu = 0.1$ for all particles (0% rough concentration); (b) $\mu = 0.5$ for all particles (100% rough concentration); (c) 50% rough particle concentration where $\mu = 0.1$ between light particles, $\mu = 0.5$ between dark particles, and $\mu = 0.3$ for mixed contacts.

in the axial direction of the simulated tumbler. The particle parameters were based on the typical material properties of the chrome steel beads used in the experiments ($k_n = 4.44 \times 10^9$ N/m^{3/2}, $k_t = 7.23 \times 10^5$ N/m, and $k_d = 380$ N s/m^{3/2}) with a time step of $\Delta t = 2.76 \times 10^{-7}$ s.

A sensitivity analysis was performed to determine the most important parameters that influence the angle of repose in the simulations. The stiffnesses, coefficient of friction, and damping were varied by an order of magnitude, but the angle of repose was only influenced by changes in the coefficient of friction. Therefore, investigations were limited to low and high friction between particles. Single snapshots of the simulation results with low friction particles ($\mu = 0.1$) and high friction particles ($\mu = 0.5$) are shown in Figures 5(a) and 5(b), respectively. After achieving steady flow, the angle of repose of particles at the free surface was averaged over 250 simulation configurations distributed over more than one-quarter revolution of the drum so that more than half of the particles passed through the flowing layer. For the condition of $\mu = 0.1$, the angle of repose was $16.9 \pm 0.9^\circ$. It increased to $24.7 \pm 1.1^\circ$ when the coefficient of friction was set at $\mu = 0.5$. While the magnitudes of the angle of repose do not match the experimental results, the increased inter-particle friction causing an increase in the angle of repose is qualitatively consistent. The likely reason for the differences between experimental and simulation results is the limited size of the

simulated tumbler due to the computation being constrained to a reasonable number of particles (4000).

To model mixtures of smooth and rough particles, bi-disperse mixtures of low friction and high friction particles were simulated. One of the difficulties is determining the value of the coefficient of friction that should be used for interactions between the low friction and high friction particles in simulating the mixture. In this case, such interactions were assumed to have a coefficient of friction of $\mu = 0.3$, the average of the low and high friction particles. The resulting angle of repose was $19.9 \pm 0.9^\circ$ for a 50% rough concentration, shown in Figure 5(c). Simulations at other concentrations of rough particles resulted in a linear relationship between the concentration of high friction particles and the angle of repose. Thus, the particle dynamics simulations confirmed that the angle of repose changes by varying only the coefficient of friction.

Finally, a benefit of the particle dynamics simulation is the knowledge of every particle position. A statistical analysis verified that the number of contacts between low-low, high-high, and mixed friction particles matched the expectation for a random distribution of particle contacts. This also matches the experimental observation of complete mixing of particles having different frictional properties with no tendency toward segregation.

V Conclusions

It is clear that nanoscale surface roughness of a granular material can affect the macroscale behavior. The dynamic angle of repose is greater for rough particles than for smooth particles over a wide range of Froude numbers. Furthermore, as the concentration of rough particles increases, a corresponding increase in angle of repose occurs, regardless of the Froude number. However, it is quite difficult experimentally to wholly capture the effect of the surface roughness solely in terms of the coefficient of friction. The contact area between particles is so small that the interlocking of asperities and stiction can play a major role. Nevertheless, particle dynamics simulations verified that increasing the coefficient of friction between particles alone increases the angle of repose of the bulk material just as increasing the fraction of rough particles does.

Even though the angles of repose of the rough and smooth particles differed substantially, this

did not result in either radial segregation in quasi-two-dimensional tumblers or banding in three-dimensional tumblers for bi-disperse mixtures. The absence of segregation both experimentally and computationally suggests that the segregation mechanisms based solely on surface roughness or the angle of repose need to be reconsidered. A variation in the angle of repose may be necessary for segregation but is clearly not sufficient. While both properties of surface roughness and angle of repose may play a role in the flow ability of granular material, they do not by themselves appear to cause segregation.

Acknowledgments This work was funded in part by the Office of Basic Energy Sciences of the Department of Energy (DE-FG02-95ER14534) and by the National Science Foundation IGERT Programs “Dynamics of Complex Systems in Science and Engineering” (DGE-9987577) and “Virtual Tribology” (DGE-0114429). Also, thanks to Professor Qian Wang for providing access to the ADE Phase-Shift MicroXAM and CETR Tribometer to characterize the surface properties of the granular material. Thanks to Paul Umbanhowar for several useful discussions.

Particle dynamics simulations reveal parallels between granular mixtures and chemical solutions. Thermodynamic solution theory provides a connection between the interaction strength of the molecules, the concentration of each species in the solution, and bulk solution behavior. Particle dynamics simulations demonstrate a similar relationship between the inter-particle forces, the composition of the granular mixture, and bulk flow behavior. The analogy holds true over different particle interaction types (friction or adhesion) and over different bulk properties (the angle of repose in a rotating drum and the viscosity of particles sheared between parallel plates). A solution theory for granular mixtures would provide a framework to study the properties of granular mixtures.

3

Granular mixtures: analogy with chemical solution thermodynamics

I Introduction

Our understanding of granular behavior has progressed in recent years in part due to direct [109–113] and heuristic [114–116] analogies to thermodynamics and statistical mechanics. Drawing parallels from thermodynamics provides a concerted way to extend a large body of knowledge from molecular to granular systems. At the same time, even though general parallels exist it is often difficult to define the details of granular thermodynamics for even the most basic concepts. For example, a granular material can be seen to act like a solid, liquid or gas depending upon its effective temperature [117, 118]. Yet there is still debate about how to define this granular temperature [119]. However, even without a rigorous definition of some of the key thermodynamic properties, analogies to thermodynamic concepts can enrich our understanding of granular behavior.

In many thermodynamics textbooks a few chapters are devoted to the behavior of mixtures, often called solution theory [120, 121]. In the theory, bulk properties of a mixture are connected to the interactions of the species in the mixture and studied as a function of concentration. To our knowledge, there has been no application of solution theory to granular materials. If such parallels exist, they would be useful given that many granular materials are not homogeneous, but are mixtures of more than one type of particle.

Solution theory can give us a structure to analyze properties of granular mixtures as a function of the concentration of the particle types and the types and strength of the interactions between particles. The goal in this Letter is not to derive the details of a granular solution theory from first principles, but rather to show parallels that exist between the behavior of chemical solutions and granular mixtures and explain how this comparison increases our understanding of the behavior of granular mixtures.

In chemical solution theory, the baseline model is called the ideal solution. In an ideal solution the bulk properties are directly proportional to the concentration of the individual components. Real solutions are then compared to and classified according to their deviations from the ideal solution model. Real solutions display a wide range of behavior spanning both strong positive and negative deviations from the ideal solution model. Bubble points, dew points, enthalpies, and molar volumes are commonly analyzed with solution theory. This Letter will show that bulk properties of granular mixtures can display a similar range of ideal and non-ideal behavior. Using the structure of solution theory helps to understand how bulk properties depend upon particle interactions and the composition of the mixture.

II Simulation method.

Particle dynamics simulations are increasingly used to model granular systems. They are a discrete element simulation method similar to molecular dynamics, where the forces between elements are patterned after the significant forces acting on solid particles [122, 123]. Linear and rotational movement of the particles is followed through time and is calculated from the contact forces and body forces acting on the particles. The particle interactions in the simulations can

be precisely controlled and the effects measured, making these simulations a useful tool to test whether granular materials follow solution theory.

A Force Models

The forces accounted for in each simulation include gravity, contact forces and, in some simulations, an adhesion force. The components of the contact force are calculated separately as normal and tangential components.

The normal component of the contact force is calculated from equation 1 where α is the sum of the particle radii minus the distance between particle centers and represents the amount of particle deformation during a collision. k_n is a spring constant and k_d is the dissipation constant.

$$F_n = k_n \alpha^{3/2} - k_d v_n \sqrt{\alpha} \quad (1)$$

This equation is based on Hertz's Theory of elastic contact, but also includes a dissipation term which depends on the relative velocity (v_n) of the particles and the square root of the deformation. This form of the dissipation term reproduces the experimentally observable behavior that increasing impact velocity reduces the coefficients of restitution. Tangential forces are based on Coulomb's laws of friction. Like Coulomb's laws this model connects the maximum friction force to the normal force with a coefficient of friction. It also introduces a linear tangential spring to mimic frictional forces before the onset of sliding. The tangential force is expressed as:

$$F_t = \min(k_t s, \mu F_n) \quad (2)$$

where μ is the coefficient of sliding friction, k_t is the tangential stiffness and s is the tangential displacement that has taken place since the particles first came into contact.

In some simulations an adhesion force is added using Hamaker's expression for the van der Waals attraction between macroscopic spheres in close proximity. In this Equation R is the particle radius, z is the distance between particle surfaces and A is the Hamaker constant which captures

Table 3.1: *Values of the constants used in particle dynamics force models*

Parameter	Value	Units
k_n	3.44×10^9	$\text{Nm}^{-3/2}$
k_d	7.85×10^5	$\text{Nsm}^{-3/2}$
k_t	4.34×10^5	Nm^{-1}
μ	varied	none
A	varied	J

the chemical properties of the particles.

$$F_A = \frac{A}{6z^2} \left(\frac{1}{R_1} + \frac{1}{R_2} \right)^{-1} \quad (3)$$

This expression diverges as z goes to zero. Usually repulsive forces between atoms are found to be important at separations of approximately 4 Å. To prevent divergence in the simulation, the adhesion force is held constant when z is less than 4 Å and throughout particle contact. The values of the constant parameters in the force models can be found in Table 3.1.

B Flow geometries

Results from two different flow geometries are reported in the paper. Particles are rotated in a circular drum and sheared between parallel plates. The walls in both cases consist of particles 1.5 mm in diameter but otherwise with the same properties of the free-flowing particles. The sides not bounded by walls are treated with periodic boundary conditions. Free-flowing particles have a size distribution to avoid crystallization affects. The average particle diameter is 1.2 mm, but can vary up to 5 percent larger or smaller than this. Both wall and free-flowing particles have a density of 7900 kg/m³.

The rotating cylinder has a diameter of 40 particles and is 3 particles deep. The open faces of the cylinder have periodic boundaries. In all simulations reported the drum is rotated at 10 rpm and is filled with 3400 free-flowing particles which fill the drum nearly half way.

In the simulated shearing, each wall is 20 particles long and 4 particles deep and the gap is filled with 800 free-flowing particles. The top wall is sheared at a rate of 12 cm/s and is free to move up or down to allow the sheared particles to dilate. The weight of the wall particles keeps

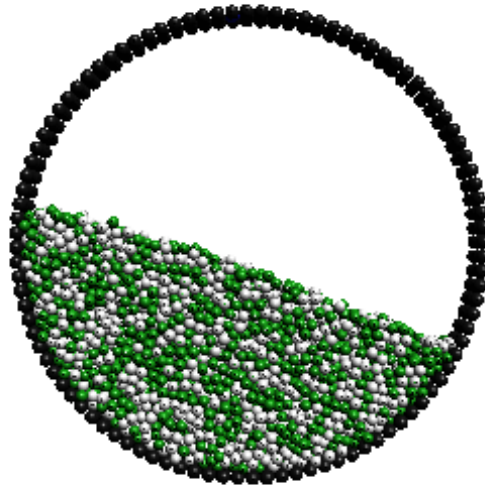


Figure 3.1: *The simulation volume of the rotating cylinder simulations.*

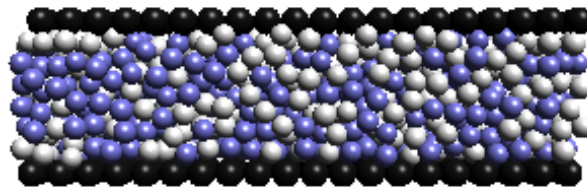


Figure 3.2: *The simulation volume of the sheared parallel plates.*

the wall in contact with the free-flowing particles.

In the simulations of the drum, inter-particle friction and adhesion were altered systematically and the effect on the dynamic angle of repose was measured. In the simulations of shearing, the effect of inter-particle friction was changed and the viscosity of the granular material was calculated. In all simulations, changes were only made to friction or adhesion properties; the size and density of all particles were always the same.

III Dependence of the angle of repose on friction and adhesion

The focus of this work is the behavior of mixtures, but knowledge of the behavior of homogeneous particles provides a baseline to analyze the mixture behavior. Similar to recent experiments [16], simulations in the rotating drum show that increasing the friction coefficient between particles increases the dynamic angle of repose (Figure 3.3). The angle of repose increases monotonically as the friction coefficient (μ) increases from 0 to 1; however, the slope of the plot in Figure 3.3 steadily decreases.

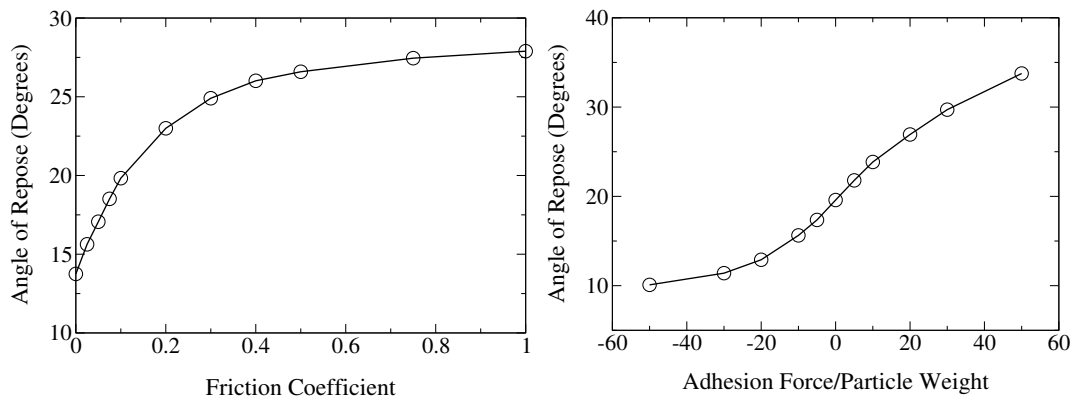


Figure 3.3: *The angle of repose in a circular drum as a function of friction coefficient (left) and adhesion force (both attractive [+] and repulsive [-]) between particles (right).*

Inter-particle attraction and repulsion also affect the angle of repose. The angle of repose of the bulk granular material is seen to increase with increasing particle attraction Figure 3.3.

IV Contact analysis of well mixed systems

The bulk properties of a granular mixture will depend upon the concentration of the various particle types in the mixture. More specifically, in a system where particles differ only in their surface properties, it is the prevalence of each type of particle contact that is important to bulk properties. For a well-mixed system of particles of the same size, the distribution of contacts can be predicted from the concentration of particle types as follows. In a binary mixture of type A and B particles, there are three types of particle interactions: A-A, B-B, and A-B. We wish to express the

impact of the heterogeneous A-B interaction on the bulk behavior of the mixture—an interaction which is not present in homogeneous systems. A probability analysis can predict the prevalence of each type of contact in a randomly mixed system of particles of the same size. For example, in a binary mixture where 25% of the particles are of type A, a random contact between two particles has a 25% 25% or 6.25% chance that the contact will be of the A-A type. In the same mixture there will be 56.25% B-B contacts and 37.5% A-B contacts. This probability analysis is easily performed for the whole range of possible compositions in a binary mixture and is shown in Figure 3.4. From this analysis we can expect the heterogeneous contact to be important to the bulk behavior of the mixture over a wide range of compositions spanning at least the range of 20-80% type A particles.

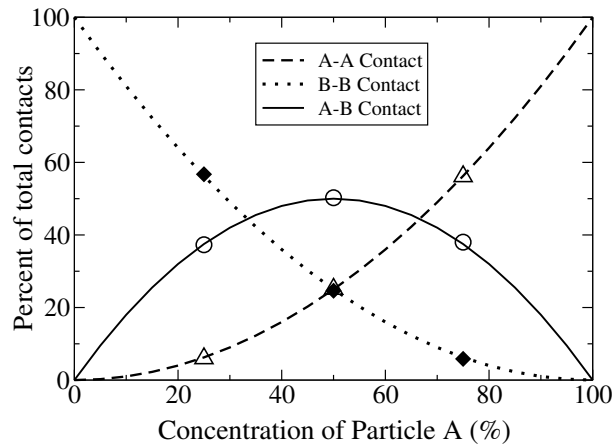


Figure 3.4: Analysis of contacts in a binary mixture of particles A and B. Lines are calculated from probability in a random mixture; markers are observed values in the particle dynamics simulations.

During simulations where particles differed only in their coefficients of friction, we counted the number of homogeneous and heterogeneous contacts and found them to agree well with the expected values for a random mixture (Figure 3.4). The agreement of the simulations with the probability analysis shows that particles do not segregate due to friction [124].

V Ideal and non-ideal behavior of a granular mixture

Simulations of a rotating drum were run to investigate the effect that changing the heterogeneous interaction has on the dynamic angle of repose of a binary mixture. Two systems were investi-

gated: in the first system particles differed only in their friction coefficients, while in the second system particles differed only in adhesive properties. In the frictional system, the values of the homogeneous friction coefficients (μ) were fixed at 0.2 for μ_{A-A} and 0.05 for μ_{B-B} , while the value of μ_{A-B} took on a range of values from 0 to 0.5. The resulting angles of repose are plotted as a function of mixture composition in Figure 3.5. The value of μ_{A-B} has a large influence on the angle of repose for mixtures where the A-B contact is plentiful. If μ_{A-B} is set near the average of the homogeneous friction coefficients, the angle of repose increases linearly with concentration. However, if μ_{A-B} deviates significantly from this average value, the angle of repose becomes a non-linear function of concentration and can even produce a maximum or minimum if μ_{A-B} is greater than μ_{A-A} or less than μ_{B-B} .

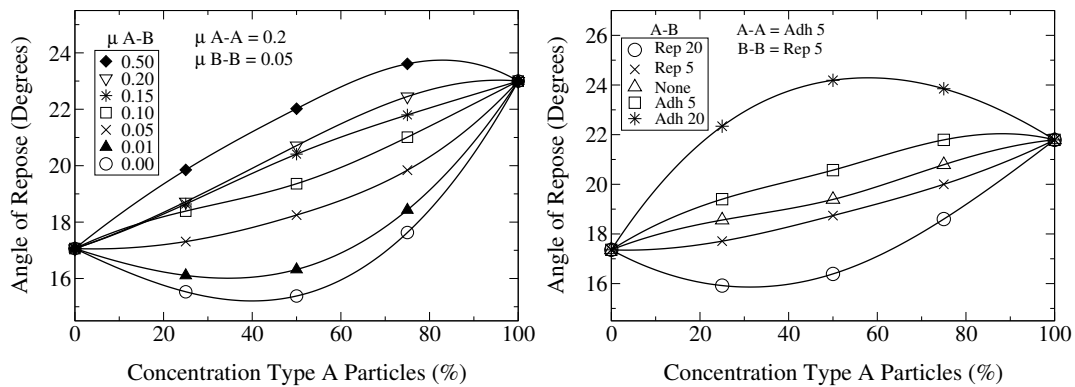


Figure 3.5: Angle of repose as a function of mixture composition. Ideal as well as both positive and negative deviations from ideal behavior are observed depending on the heterogeneous (A-B) interaction. Frictional system left, adhesive system right.

The behavior in Figure 3.5 mirrors the range of behavior seen in bulk properties of chemical solutions. It is common to see plots similar to Figure 3.5 for properties such as bubble points, dew points, enthalpy, and molar volume. Depending on the molecular interactions in the solution, bulk properties can vary linearly or deviate positively or negatively from linear behavior as a function of concentration. In solution theory a linear relationship is classified as ideal behavior and non-ideal solutions which deviate in either the positive or negative directions from ideality are not uncommon. In the granular system, the ideality of the mixture is determined by the heterogeneous interaction (μ_{A-B}). The second granular system simulated in the rotating drum consisted

of particles that differed only in their attractive properties. Simulations were run where the A-A interaction was attractive and the B-B interaction was repulsive. The magnitude of each interaction force was five times the weight of one particle. The A-B interaction strength was modified to study a range of forces spanning from a repulsive force of 20 particle weights to an attractive force of 20 particle weights. Simulations of mixtures of varying concentrations of adhesive and repulsive particles were run and the measured angles of repose are plotted in Figure 3.5. The adhesive–repulsive system of particles also displays the full range of ideal and non-ideal behavior in the angle of repose depending upon the interaction strength of the heterogeneous contact. Hence solution theory can be used to describe granular behavior arising from a variety of particle interactions. It is interesting to note that the shape of the curves in Figure 3.5 is not symmetric despite the symmetry present in Figure 3.4. The concentration at which a maximum or minimum occurs is a result of both the contact analysis (Figure 3.4) and how the friction coefficient affects the angle of repose (Figure 3.3). The non-linear behavior of the angle of repose as a function of the friction coefficient produces the asymmetry in Figure 3.5.

VI Granular viscosity

A granular solution theory should be applicable to a variety of bulk properties across many flow geometries. Simulations of a sheared granular material were also run to demonstrate the versatility of the analogy. The viscosity of a granular material was calculated by shearing it at a constant velocity between two parallel plates. The top plate is free to move in the direction normal to shear, but the weight of the plate keeps it in contact with the flowing particles [16]. The viscosity of the granular material was calculated from the shear stress that the top plate experienced during the simulation divided by the shear strain. The velocity profile was observed to be nearly linear at the set wall velocity of 12 cm/s. The viscosity of the granular material is sensitive to both the inter-particle friction and the friction with the wall, but since we are interested mainly in the properties of the granular material the friction coefficient between the wall and any free flowing particle was set to 0.5 throughout all simulations. Changing the friction coefficients between free-flowing particles produced the reported change in viscosities. The viscosity of a homogeneous granular

material increases as the inter-particle friction coefficient is increased (Figure 3.6 left). When a mixture of particles is sheared, the viscosity depends upon the value of the heterogeneous friction coefficient as well as the concentration of the high and low friction particles. The plot in Figure 3.6 (right) is very similar to the plots in Figure 3.5 even though a different property and different flow geometry of the granular material were studied. In both instances the behavior of the granular material follows a solution theory type behavior.

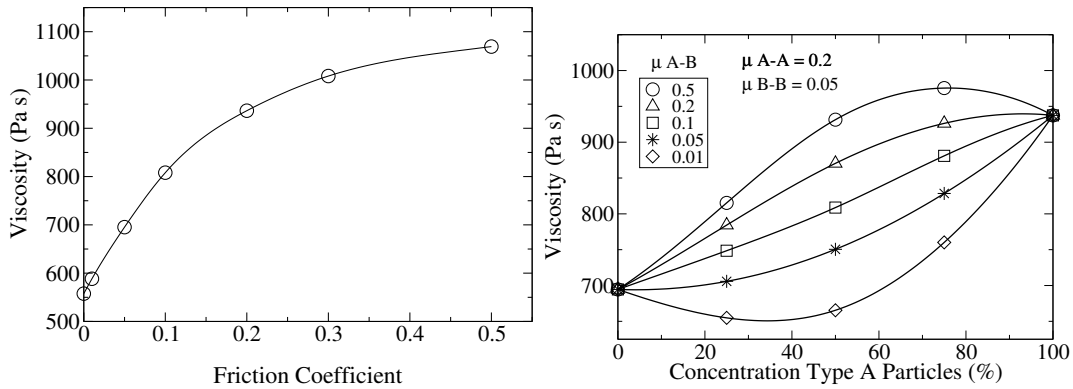


Figure 3.6: Viscosity of a homogeneous granular material as a function of friction coefficient (left). The viscosity of a granular mixture behaves in a manner predicted by solution theory (right).

VII Conclusions

Our simulations show that granular mixtures can be classified in a similar manner as chemical solutions. The bulk properties of a granular mixture depend upon the interaction strength of the various particle types as well as on their relative concentrations. Depending on the heterogeneous interaction (A-B), the bulk properties of a granular mixture can be classified as ideal or can display either positive or negative deviations from ideality as a function of concentration. The study of other properties of granular mixtures (e.g. packing densities, rheology, ease of fluidization etc.) could benefit from an analysis using this same structure, the structure of solution theory. Further development of a rigorous solution theory for granular matter could provide insights into the connection between bulk granular flow behavior of mixtures and the properties and interactions of the particles. Development of a granular solution theory could provide a way to predict the

properties of the bulk powder given the properties of the particles, or possibly even facilitate the reverse analysis—providing a way to estimate individual particle interactions based on the bulk behavior of a mixture.

Acknowledgments The authors thank the U.S. National Science Foundation IGERT program and the Air Force Office of Scientific Research for funding.

Particle dynamics models are developed and used to design a mechanical damping device which uses micro or nano powders as the damping medium. A damping device based on a powder has the advantage of temperature insensitive operation over the traditional use of a viscous fluid. Adhesion forces significantly affect the behavior of small particles. The damping mechanism targeted stems from energy dissipated due to the breaking of many adhesive particle contacts. Adhesive contacts can dissipate energy due to hysteresis in the force between particle loading and unloading. Adhesion hysteresis was added to the JKR model of adhesive contact and then used in particle dynamics simulations. The effects of adhesive properties and packing densities are studied in two device geometries (shear and a piston) using simulation.



Mechanical Damping Using Adhesive Micro or Nano Powders

I Introduction

It is often desirable to damp mechanical motions or vibrations to protect mechanical structures from fatigue. Devices engineered for damping commonly exploit the viscous drag of a liquid to convert the undesirable kinetic energy into heat. However, under extreme conditions—such as wide temperature ranges—liquids are not suitable as a damping medium. For example, most damping fluids cannot withstand operating temperatures above 500 C, and the viscosity can vary widely with temperature which can cause poor performance. On the other hand, the performance of granular materials is largely unaffected by temperature [125,126].

Granular materials are well suited for use as a damping medium since they naturally dissipate energy through a number of mechanisms when they flow, are jostled or are impacted. Because of these natural characteristics of granular materials, they have recently been targeted for use to

damp mechanical motion in a number of applications. For example, particles can be injected into cavities of beams and plates [127] to help dissipate vibrations in structures. The performance of these dampers appears to be effective in damping vibrations of a wide range of frequencies [128] of either harmonic or random excitations [129]. Particles are known to dissipate energy through friction as they slide along each other, or during an impact because of their viscoelastic properties or plastic deformation [130]. The particles employed in these applications typically have diameters on the millimeter length scale. What we explore here is the use of micron and nanometer-sized particles for use as the damping medium.

Micro and nano particles dissipate energy due to impacts and friction just like millimeter-sized particles. However, in addition to these mechanisms, we propose that adhesion between micro or nano particles can be targeted as a novel damping mechanism. Particles naturally become adhesive as their size decreases. The omnipresent van der Waals forces begin to overcome gravitational and inertial forces on the micro scale and can dominate the nano scale. When particles are adhesive, energy can be dissipated through adhesion hysteresis when particle contacts form and then are broken. We target this mechanism of energy dissipation to create a novel type of damper based on the dissipation of energy through adhesion hysteresis.

II Particle dynamics simulations

In order to evaluate the possibility of creating a damper based on an adhesive powder as the damping fluid, particle dynamics simulations are used to connect the adhesive properties of individual particles to the behavior of the bulk powder. In these simulations, every particle position, velocity and force is recorded throughout the simulation. This wealth of detail makes it a powerful tool to study granular behavior. The accuracy of course depends upon the assumptions made in the model, so development of realistic models is critical. We improve upon the current particle dynamics models for adhesive contact to include energy dissipation due to adhesive effects and then show ways to use the model to aid in the design of mechanical damping devices filled with adhesive particles.

III Force models

A Normal force with adhesion

Even before particle contact, adhesion from van der Waals forces can significantly affect the behavior of micro and nano particles. The attractive force between two particles whose surfaces are a distance z apart is captured in Hamaker's expression [46] [131].

$$F_{Ham} = -\frac{AR^*}{12z^2} \quad (1)$$

where A is the Hamaker constant which depends on the chemical properties of the solid. R^* is defined as

$$\frac{1}{R^*} = \frac{1}{R_1} + \frac{1}{R_2} \quad (2)$$

Hamaker's equation has been applied to particle dynamics simulations before to study the effect of adhesion on packing [132]. Once particles touch JKR theory provides a solution to the contact problem of adhesive elastic spheres in a quasi-static/thermodynamic manner. In theories of elastic contact, the effective properties of two bodies in contact are commonly defined as

$$\frac{1}{E^*} = \frac{1 - \nu_1^2}{E_1} + \frac{1 - \nu_2^2}{E_2} \quad (3)$$

$$\frac{1}{G^*} = \frac{2 - \nu_1}{G_1} + \frac{2 - \nu_2}{G_2} \quad (4)$$

where E is the Young's modulus, G the shear modulus, ν is the poisson ratio.

JKR theory considers three contributions to the energy of the system, namely the stored elastic energy, the mechanical potential energy and the surface energy. In their derivation a relationship is given between the relative approach of the particle centroids α and the applied normal load P [133].

$$\frac{\alpha}{\alpha_f} = \frac{3 \left(\frac{P}{P_c} \right) + 2 \pm 2 \left(1 + \frac{P}{P_c} \right)^{1/2}}{3^{2/3} \left[\frac{P}{P_c} + 2 \pm 2 \left(1 + \frac{P}{P_c} \right)^{1/2} \right]^{1/3}} \quad (5)$$

This expression is used in our simulations to calculate the normal force from the positions and radii of the particles. In it, α_f is defined as

$$\alpha_f = \frac{3}{4} \left(\frac{\pi^2 \gamma^2 R^*}{E^*2} \right)^{1/3} = \left(\frac{3P_c^2}{16R^*E^*2} \right)^{1/3} \quad (6)$$

where γ is the interfacial energy of the contact. α_f represents the tensile deformation that occurs just before particle separation during unloading. P_c in Equation (5) is the JKR pull-off force and is defined as

$$P_c = 3\pi\gamma R^* \quad (7)$$

In the simulations, both the Hamaker expression and JKR theory are used. A few comments should be made about how they are used in conjunction. The simple answer is that JKR theory is used when particles are in contact and the Hamaker expression is used when they are not, but when particles are in contact requires some discussion. Particles first touch when $z < \alpha_f$. At this point particle surfaces are said to “jump into contact”–because if they were rigid spheres they would not touch until $z = 0$. This jumping into contact is reported in experiments, but is also convenient in these simulations because it avoids the singularity in Equation (1) when $z = 0$. To ensure a continuous transition from adhesion before contact to adhesion during contact, we have used a relationship to connect the Hamaker constant to the surface energy $A = 24\pi z_0^2 \gamma$ where z_0 is taken as 0.165 nm [131].

B Tangential forces with adhesion

Adhesion also affects the tangential forces between particles. The tangential force model used here was created by Thornton and Yin [134,135]. Their work extends the the work of Mindlin [20] and Savkoor and Briggs [22] to model the tangential forces between adhesive spheres.

The approach of Thornton and Yin is based on the idea that the surfaces in an adhesive con-

tact will need to peel before they can slide when there is an applied tangential force. In their model, different equations are used to calculate the tangential force T depending upon whether the contact is stationary (not yet peeled) or if it is sliding.

Before the contact has peeled, the application of a tangential force will cause micro-slip in the area of contact. This is captured in the following relation:

$$T = 8G^*a\delta \quad (8)$$

where a is the radius of the contact area and δ is a displacement. This equation is sometimes called Mindlin's 'no slip' solution. In our simulations Equation (8) is used to calculate the tangential force from a displacement, or the distance that surfaces have moved relative to each other since coming into contact. Savkoor and Briggs have suggested that the application of a tangential force reduces the potential energy of the contact by an amount $T\delta/2$ which leads to the following expression for the radius of the contact area

$$a^3 = \frac{3R^*}{4E^*} \left[P + 2P_c \pm \left(4PP_c + 4P_c^2 - \frac{T^2E^*}{4G^*} \right)^{1/2} \right] \quad (9)$$

The tangential force is modeled by Equations (8) and (9) during the peeling stage. Note that the radius of the contact area is used in calculating the tangential force and that the tangential force is needed to calculate the radius of the contact area. This is resolved in practice by using the tangential force from the previous time-step to calculate the radius of the contact area and then calculating the new tangential force.

The tangential force is calculated from (8) until peeling is complete. The completion of peeling is marked by reaching a critical tangential force given by

$$T_c = 4 \left[\frac{(PP_c + P_c^2)G^*}{E^*} \right]^{1/2} \quad (10)$$

Once T_c is reached peeling is complete and sliding can occur. The tangential force during sliding is calculated from one of the following expressions depending upon the magnitude of the normal

force. If $P < -0.3P_c$ the tangential force is calculated as

$$T = \mu P' \left(1 - \frac{P' - P}{3P'} \right)^{3/2} \quad (11)$$

where μ is the friction coefficient and P' is defined as

$$P' = P + 2P_c + 2(PP_c + P_c^2)^{1/2} \quad (12)$$

When $P > -0.3P_c$, the tangential force is calculated from

$$T = \mu(P + 2P_c) \quad (13)$$

When used in conjunction, Equations (8)-(13) have been shown to match experimental measurements of the tangential force during adhesive contacts well over a wide range of normal loads [135].

C Addition of adhesion hysteresis

Up to this point we have explained Thornton's model for adhesive contact and applied Hamaker's expression to account for attractive forces between particles which are close but not touching. In this section we describe modifications to JKR theory to cause energy dissipation in each adhesive collision.

The loading and unloading of a particle contact following JKR theory, being a quasi-static thermodynamic theory, is a perfectly elastic interaction. It does not capture the energy losses that occur in dynamic collisions. Modifications to JKR theory are necessary to simulate a collision which dissipates energy. Thornton's application of JKR theory does include some energy dissipation. In their simulations, particle contact does not occur until $\alpha = 0$ during loading, but during unloading, particles remain in contact until $\alpha = -\alpha_f$. The energy dissipated during a collision is a constant value given by

$$E_{diss} = \int_{-\alpha_f}^0 P d\alpha \quad (14)$$

where $P(\alpha)$ is obtained by rearranging Equation (5). The energy dissipated during a collision using this strategy is constant regardless of the details of the collision. The same amount of energy is dissipated no matter what the incoming velocity or how compressed the particles became during the collision.

We have increased the complexity of Thornton's simulation model to capture some of these details by including adhesion hysteresis. Experiments show hysteresis, or a difference in the contact force between loading and unloading, in adhesive contacts [136, 137]. It is thought that adhesion hysteresis arises from surface rearrangements which occur during contact [138, 139]. Molecules can form bonds or become entangled with molecules on the opposite surface, which causes the force to separate surfaces to be greater than the attractive force which brought them together [140]. The difference in contact forces between loading and unloading causes a loss of energy. This mechanism of energy dissipation is what is being targeted in this work to design a mechanical damping device. Adhesion hysteresis and the subsequent energy dissipation were included in our simulations by replacing the thermodynamic work of adhesion in the JKR model with an energy release rate Γ which differs depending upon whether the particles are advancing Γ_a or retracting Γ_r . Considerable differences in the energy release rate have been measured experimentally to the point where Γ_r can be up to $100\Gamma_a$ [137].

A single collision between particles which have a hysteretic adhesion force ($\Gamma_r = 10\Gamma_a$) can be analyzed by looking at the resulting load-displacement plot. Two identical particles with properties listed in Table 4.1 were made to collide at a relative velocity of 0.22 m/s and the normal force was recorded and plotted vs. α for each time-step the particles were in contact. The area between the loading and unloading curve represents the energy dissipated during the collision. This area will increase as the initial velocity increases because higher values of α will be reached during the collision. We note that for low-velocity collisions, the particles hit and stick without bouncing off. This occurs when the energy dissipation is greater than the initial kinetic energy.

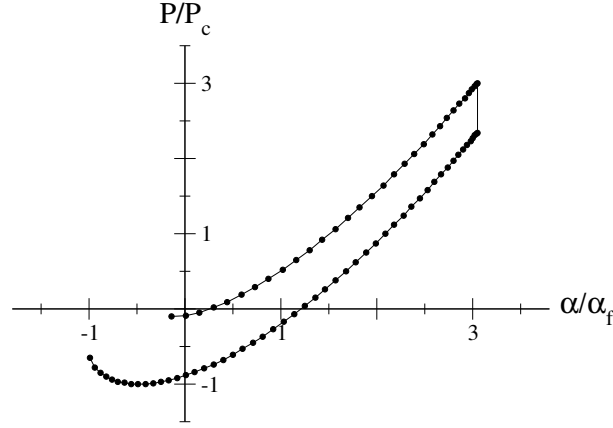


Figure 4.1: Example of a normal collision with adhesion hysteresis where $\Gamma_r = 10\Gamma_a$ and $v_i = 0.22\text{m/s}$. P_c and α_f were calculated using Γ_r

Table 4.1: The default particle properties used in the simulations reported in this work.

Parameter	Value	Units
R_{ave}	40	μm
E	68.95	GPa
G	25.92	GPa
ν	0.33	
ρ	2700	kg/m^3
Γ_a	0.32	J/m^2
Γ_r	3.2	J/m^2
μ	0.3	
dt	2.00	ns

IV Device design

With a model that captures the energy dissipated through adhesive contacts, we can use particle dynamics simulations to connect the inter-particle forces to bulk powder damping behavior. Design of a damping device includes matching the expected external forces (impacts, torques or vibrations) to the dissipation of the damping medium. Parameters that might be altered to change the performance of the powder include: particle size, adhesive properties, and packing density (solid fraction). We will investigate the effects of changing some of these parameters in two possible damper geometries.

A Couette flow

One of the canonical geometries in fluid mechanics is Couette flow. The shearing of adhesive particles in Couette flow may prove to be a useful geometry to design a mechanical damping device. The shear cell in Figure 4.2 is operated at constant volume with the rigid walls made of 80 (20x4) particles each. The radius of the wall particles is $50\mu\text{m}$ (slightly larger than the free-flowing particles), and the top wall sheared at a constant rate of 0.1 m/s . Periodic boundary conditions are applied at the open faces of the shear cell.

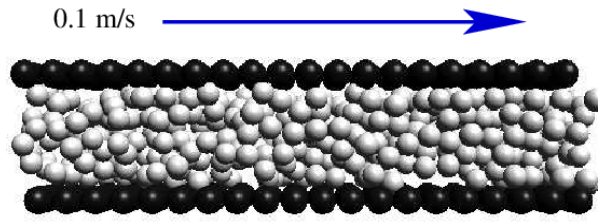


Figure 4.2: *Shear cell geometry.*

In the simulated results that follow, the shear stress that the top wall experiences is calculated at each time-step and averaged over a length of time after it has stabilized (once there is no long-time trend either up or down in the shear stress).

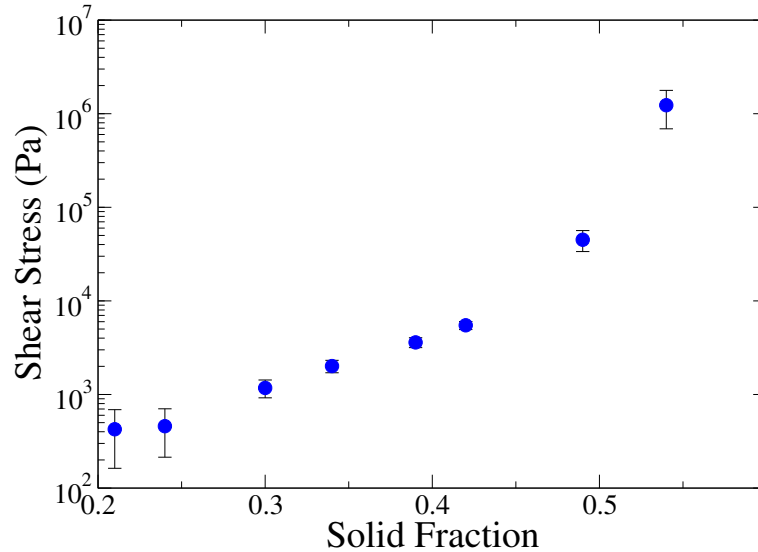


Figure 4.3: *Shear stress as a function of the packing density. Note that the y-axis is on a log scale.*

As seen in Figure 4.3 the packing density (reported here as the fraction solids) has a large effect on the shear stress. Higher solid fractions produce higher shear stresses, more particle contacts are created and broken, which increases the total energy dissipated.

In our adhesion model with hysteresis, the energy release rates of loading and unloading can be changed independently. Both the loading and unloading energy release rate have a large effect on the resulting shear stress. The shear stresses reported in Figure 4.4 were calculated by changing the energy release rate during unloading (Γ_r) while holding the energy release rate during loading constant (Γ_a). Increasing Γ_r in this manner increases the force required to break particle contacts, which is reflected by the corresponding increase in the shear stress.

The behavior of the calculated shear stress when Γ_a is changed holding Γ_r constant is somewhat more complex (Figure 4.5). Perhaps surprisingly, the shear stress as a function of Γ_a passes through a maximum. The decrease in shear stress as Γ_a approaches Γ_r can be understood by considering the amount of energy dissipated per collision. As Γ_a approaches Γ_r , collisions become increasingly elastic and less energy is dissipated per collision. The shear stress is dependent upon the energy dissipated in the flowing powder. Higher dissipation in the powder requires a greater force on the wall to maintain its velocity constant.

The increase in shear stress in Figure 4.5 at low values of Γ_a cannot be explained by dissipation in normal collisions. Decreasing Γ_a while holding Γ_r constant can only increase the energy dissipated per normal collision. The increase can, however, be explained by considering the tangential or friction force. Increasing Γ_a causes higher frictional forces during the loading portion of the contact, and frictional forces contribute to energy dissipation. The maximum seen in Figure 4.5 thus reflects two competing dissipation mechanisms when Γ_a is increased while holding Γ_r constant. The shear stress is a collective measure of the energy dissipated in the flowing powder. Higher dissipation in the powder requires a greater force on the wall to maintain its velocity constant.

B Modifying the geometry of the shear cell

We imagine a damping device which dissipates energy through the continuous breaking and reforming of adhesive contacts. Agglomerates of micro or nano particles will dissipate energy as

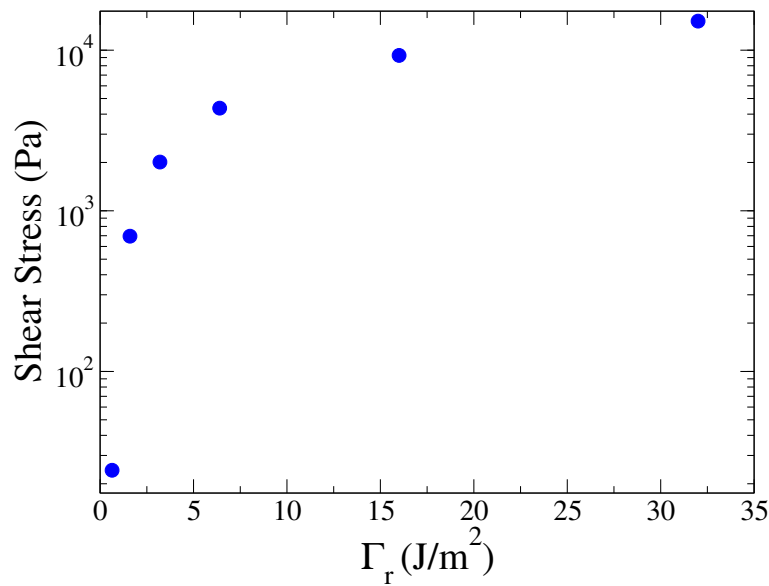


Figure 4.4: Shear stress as a function of the energy release rate of unloading (Γ_r). Note that the y-axis is on a log scale.

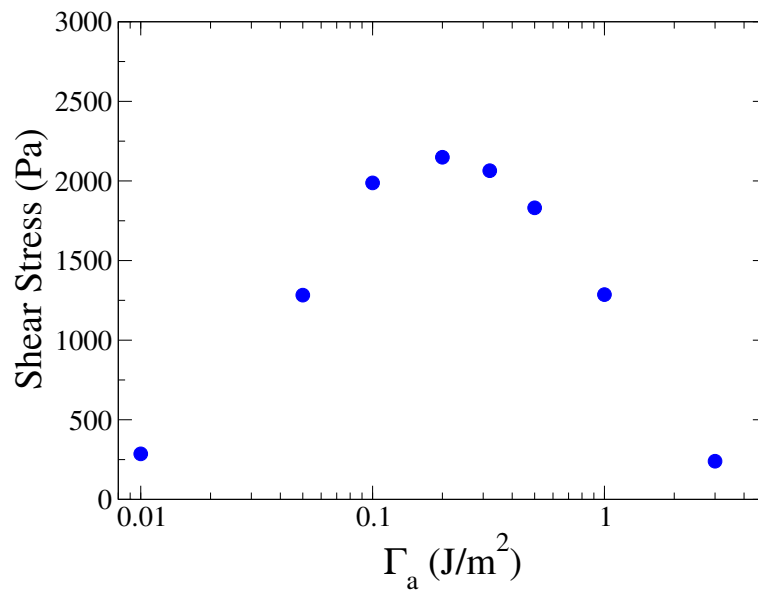


Figure 4.5: Shear stress as a function of the energy release rate of loading (Γ_a). Note that the x-axis is on a log scale.

they are broken and then naturally reform as flow continues, enabling a cyclic or continuous process. Some small modifications to the basic shear cell may increase damping by creating flow patterns that more effectively break up particle agglomerates. One way to achieve this could be to control the surface roughness or add teeth to the solid surface of the shear cell. Figure 4.6 displays

how a shear cell with teeth would be hindered by particle flow and thus increase damping.

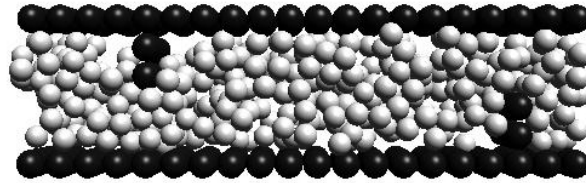


Figure 4.6: *Couette shear cell with teeth to break up agglomerates.*

C Piston geometry

Another geometry that can be targeted for device design is a piston. The shock absorbers on a car are an example of this geometry, which achieves damping by forcing the fluid to pass through orifices in a moving disc. This section shows simulation results for a similar piston geometry filled with particles instead of a liquid. The simulation volume shown in Figure 4.7 represents one repeating unit of the full piston. The faces not bounded by the end walls have periodic boundary conditions. The black particles near the middle on either side of the picture are moved up and down in the simulation. We refer to these as the disc. As the disc moves, free-flowing particles (white) are forced through the gap in the disc. The adhesive contacts of the flowing particles are broken and reformed, dissipating energy along the way.

One way to study the damping performance of the piston geometry is to apply a prescribed motion to the disc and calculate the force experienced by the disc as the particles are forced through it. Figure 4.8 shows the position and force for an applied sinusoidal vibration at 700 Hz.

Knowing the force which the disc experiences as it is displaced enables us to evaluate damping by calculating the energy dissipated per cycle. A plot of the force vs disc position is shown in Figure 4.9. The cyclic process creates a loop. The area bounded by this loop is the energy dissipated per cycle. The energy dissipated per cycle is a function of both the particle and system properties. One of the easiest parameters to control from the perspective of a device designer is the packing

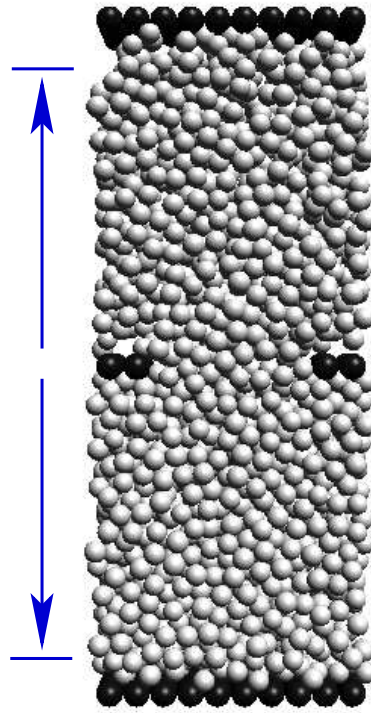


Figure 4.7: *Enclosed container with moving piston. particles are forced to flow through the hole in the moving piston*

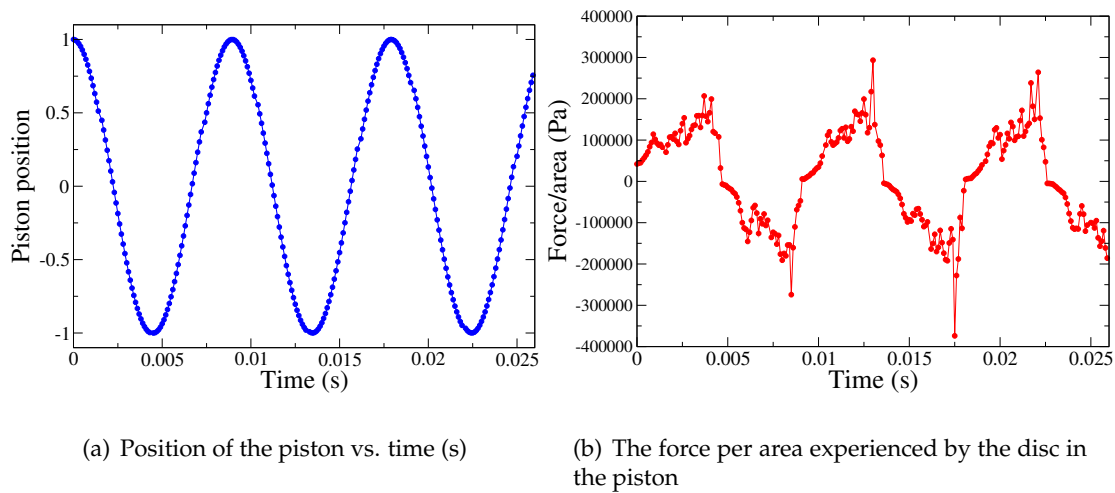


Figure 4.8: *The position and force experienced by the disc in the piston for a sinusoidal vibration at 700 Hz*

density or solid fraction. Adding more particles or taking some out should provide a straightforward way to tune the device to meet the expected vibrations. Figure 4.10 reports the performance

of this piston assembly as the number of particles in the simulation is changed to give a range of solid fractions from 0.35 to 0.55. It should be noted that the maximum solid fraction of identical spheres is 0.74.

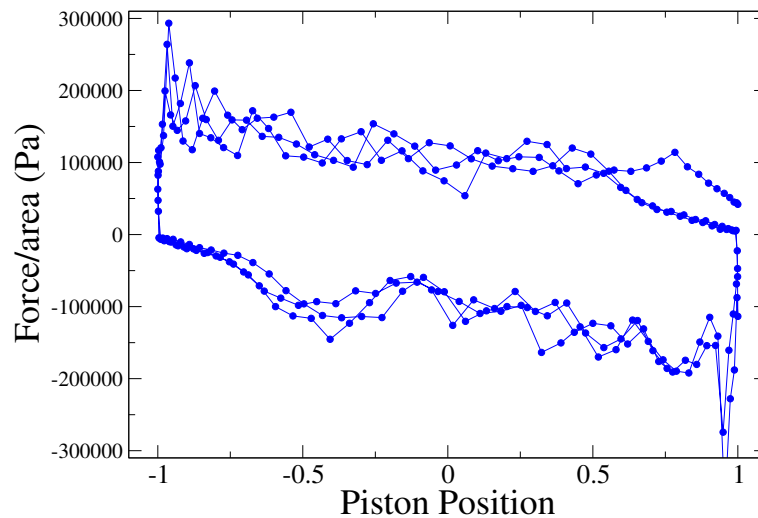


Figure 4.9: Force per area of disc plotted vs. disc position. The area bounded by the loop represents the energy dissipated per cycle.

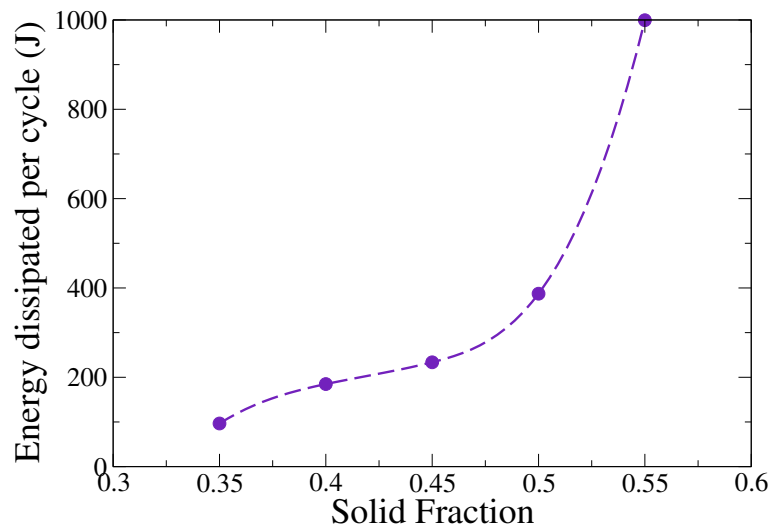


Figure 4.10: Energy dissipated per cycle for increasing packing density. Sinusoidal vibrations are applied at 700 Hz

Changing the packing density is just one example of the many particle and system properties which could be explored using particle dynamics simulations. We have already mentioned that

particle size and adhesion both affect damping. In addition system properties such as the size of the holes in the disc or disc thickness could be explored as a guide to experiments.

V Conclusion

We have added hysteresis to a particle dynamics model for adhesive particles and have used these simulations to investigate the dependence of damping performance on the adhesive properties and packing densities of small particles. The simulation results offer evidence that micro or nano particles can be used as a novel damping medium which dissipates energy through adhesion hysteresis. This simulation method and model promise to provide a useful tool to design particle dampers based upon this or other damping mechanisms.

Monte Carlo simulations of chain molecules are used to study lubricant film behavior in confined regions. Lubrication failure is studied under two possible scenarios. The first is desorption of the lubricant molecules from the gap between asperities driven by equilibrium thermodynamics with increasing temperature. The second is the physical removal (squeezing out) of lubricant molecules from between asperities in close proximity due to high loads on solid asperities. Using simulations in the grand canonical and grand isostress ensembles, combinations of load and increased temperature are evaluated for their potential to thermodynamically drive the system to a lubrication failure event.

5

Analysis of lubrication failure using molecular simulation

I Introduction

The purpose of a lubricant is to decrease friction and protect solid surfaces from wear. When a lubricant no longer performs this function, it is said to have failed [141]. One of the main ways that lubricants protect surfaces is by preventing solid-solid contact. In many important mechanical systems, only a thin nanometer lubricant film adsorbed to the sliding solid surfaces prevents them from coming into direct contact and initiating failure [142]. A system relying on thin films is called boundary lubrication. Because these lubricant layers are so thin, they are very sensitive to system conditions and can fail by several mechanisms. The lubricant molecules can desorb from the confined regions [143–145], be physically removed [146, 147] (squeezed out from between solid surfaces) or they can degrade through chemical reactions [148–150]. Failure could be prevented

more often if the details of the mechanisms were better understood [141].

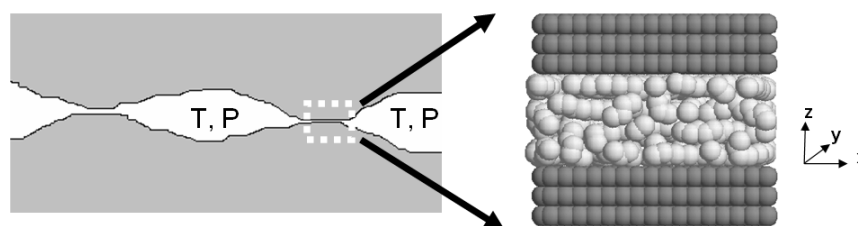


Figure 5.1: The simulation cell on the right models a lubricant between two asperity surfaces. These regions may experience high stress and significant temperature spikes.

Lubrication failure is often thought to initiate between asperities in close proximity [148](Figure 5.1). Extreme temperatures and stresses are most likely to occur in these locations [151]. High shear rates causing temperature spikes of several hundred degrees above the ambient temperature have been both theoretically predicted [143,152] and experimentally measured [153–156] between asperities. These high temperatures, often called flash temperatures, may cause desorption of the lubricant molecules from the gap depending on the duration and magnitude of the temperature spike. High normal stresses are also commonplace between asperities where the load from the whole solid can be concentrated on a very small area. The combination of increased temperature and normal load greatly increase the chances of lubrication failure. High temperatures can decrease adsorption making it easier for molecules to be squeezed out and allow the solid surfaces to come into contact.

Several studies have aimed to predict the onset of lubricant film failure. The first of these studies were based on the idea that lubricants would fail when they reached a certain critical temperature [157,158]. A later model was based more fully on the idea that desorption is the cause of lubricant film failure [143]. By using an energy balance to estimate flash temperatures and the Langmuir theory of adsorption, Lee and Cheng proposed that the onset of scuffing—wear to the solid surface signifying lubricant failure—would occur at critical combinations of flash temperature and fluid pressure. The onset of scuffing was connected to a minimum surface coverage of adsorbed lubricant molecules.

Modern molecular simulation methods can give greater insight to the behavior of lubricants confined between asperities. For example, Zhang et al. used molecular dynamics to simulate a confined fluid in contact with the bulk [159]. The density distribution and orientation of the molecules, as well as the dynamics of the squeezing out of the lubricant under an applied load were studied, but only at one temperature and not to the point of failure (not all of the lubricant was ever squeezed out).

The molecular simulations presented in this paper address the influence of applied load and increased temperature as possible driving forces for lubricant film failure. Combinations of two of the three mechanisms of lubrication failure discussed previously are considered: desorption and physical removal of lubricant molecules from between asperities in close proximity. The possibility of chemical degradation of the lubricant molecules is not addressed here. The molecular behavior under different temperatures and loads can be analyzed in the simulation in detail to see how they lead to failure.

Monte Carlo simulations are an efficient way to study equilibrium on the molecular level. The lubricant confined between the asperities in this study is assumed to be in equilibrium with a reservoir of bulk lubricant outside of the confined region. The failure process by either desorption or the squeezing-out mechanism is a dynamic occurrence, but the focus here will be on the thermodynamic driving forces which may drive a system toward a failure event. We will not consider motion of the asperity surfaces. Rather the results from these equilibrium simulations are the end state that the system will try to reach, and this driving force is still operative under the dynamics conditions of real lubrication.

Results from Monte Carlo simulations in two different statistical ensembles will be presented. Each method of simulation will be discussed followed by the results obtained from that ensemble. The rest of this paper is organized as follows: A description of the molecular model, simulation methods for grand canonical Monte Carlo (GCMC), results from GCMC simulations, simulation methods for the grand isostress (GI) ensemble, results from simulations in the GI ensemble, and finally conclusions.

II Molecular model

The lubricants modeled are normal (straight-chain) alkanes confined between two graphite-carbon planar surfaces. The geometry of the simulation cell is analogous to the commonly-used slit-pore in the adsorption literature [160–172]. The graphite walls contain three layers of carbon atoms and have lateral dimensions of 34.10 Å in the x and 39.38 Å in the y directions. The sides of the simulation cell not bounded by the graphite walls have periodic boundary conditions. Carbon atoms interact with atoms in the opposite wall via dispersion and repulsion interactions, modeled here with a Lennard-Jones potential ($\sigma = 3.474 \text{ Å}$, $\epsilon/kB = 47.9 \text{ K}$). In some simulations, the walls can move rigidly in the z direction, but the lateral x and y positions are kept fixed.

The alkane molecules are represented with the united atom model—each carbon and its bonded hydrogen atoms are modeled as one Lennard-Jones sphere. The lubricant molecules are flexible. Their bonds have potentials to allow bending and bond torsion, but the bond lengths are fixed (rigid). The Lennard-Jones potential is used to calculate the interaction between non-bonded atoms. The interaction parameters used in this study are taken from previous simulations of chain alkanes [173,174]]. Interaction parameters between the lubricant molecules and the carbon wall were calculated using the Lorentz-Berthelot mixing rules.

III Grand canonical Monte Carlo methods

Monte Carlo simulations in the grand canonical and grand isostress ensembles were used to evaluate equilibrium conditions of the lubricant film. Grand canonical Monte Carlo (GCMC) operates in the constant μVT ensemble, where μ is the chemical potential, V is the simulation volume and T is the temperature. GCMC has often been used to study adsorption in porous materials. The simulation volume is in equilibrium with a bulk reservoir of molecules at the system temperature and chemical potential. When the chemical potential of a species in two phases is equal, the fugacity of the species in the two phases is equal as well. The fugacity of the lubricant was calculated from the bulk fluid pressure and the flash temperature using the Peng-Robinson equation of state. In the grand canonical ensemble, the number of molecules in the simulation is allowed to fluctuate.

The average density equilibrates as the simulation progresses, and the density of molecules in the simulation volume represents the amount adsorbed at the system conditions. Since GCMC is a common tool to calculate adsorption, it will also prove to be a useful tool here to study lubricant failure due to desorption.

Monte Carlo simulations produce millions of configurations of molecules which can be used to calculate ensemble averages for properties of interest. These configurations are produced as a Markov chain by the Metropolis method [175], where the next configuration of molecules is derived from the current configuration by attempting one of a variety of Monte Carlo move types. In the GCMC simulations used here, four move types were implemented, which were taken from Macedonia and Maginn [174]. The types of moves used are insertions, deletions, translations, and cut-and-regrow moves. The molecular insertions are configurationally biased—a molecule is inserted one united atom at a time and each insertion is biased toward the more energetically favorable positions. A Rosenbluth weight is accumulated as each atom is inserted, and the weight is considered in the acceptance of the move so that the biased nature of the insertion is offset. The biased insertions increase the efficiency of insertions into the dense lubricant phase. Deletions are also weighted to remove the bias introduced by the insertions. The cut-and-regrow move deletes a portion of a lubricant molecule and regrows the deleted portion with new internal degrees of freedom.

For each simulation 5 million Monte Carlo moves were attempted. 75% of the moves were insertions and deletions, 12.5% were translations and 12.5% were cut-and-regrow moves. It was generally found that equilibrium conditions were reached after 1 million moves. Results were obtained by averaging over configurations generated from the last 3 million moves.

The Monte Carlo code used in this study was an extension of an object-oriented multipurpose simulation code (MUSIC) developed for porous materials [176]. The object-oriented nature of MUSIC provided the flexibility necessary to expand the GCMC code to incorporate the new moves required to simulate in the grand isostress ensemble (explained later).

IV Solvation pressure

The molecular level forces felt by lubricant molecules determine whether or not they are squeezed out of a gap between asperities. One measure of the stress that exists in a confined lubricant film is the solvation pressure. The solvation pressure is the pressure that the lubricant exerts on the solid surfaces. Several research studies have calculated the solvation pressure of various alkanes from simulation to highlight the effects of chain length and branching [172, 177–179]. GCMC configurations can be used to calculate the solvation pressure by summing up the force that each lubricant atom exerts on each atom in the solid surfaces.

$$P_{Sol}A = \left\langle \sum_{i=1}^N \sum_{j=1}^{N_s} \left(\frac{d\mathcal{V}}{dr_{ij}} \right) \frac{z_{ij}}{r_{ij}} \right\rangle \quad (1)$$

The first summation is over all fluid atoms N , and the second is over all solid atoms N_s . The derivative of the potential energy V with respect to the separation vector r_{ij} yields the force between atoms i and j . The factor z_{ij}/r_{ij} scales the force to take into account only the component normal to the solid surface. The angled brackets denote an ensemble average. A positive solvation pressure pushes out on the walls of the slit.

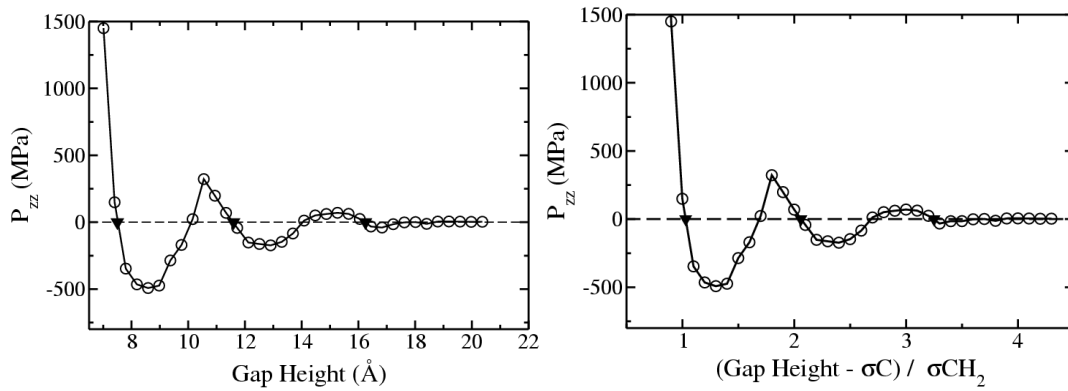


Figure 5.2: Solvation pressure as a function of gap height for pentane at 300K and 200 kPa. Stable gap heights (marked with solid triangles) correspond to molecular layering in the slit.

Figure 5.2 shows the solvation pressure calculated for pentane at a 200 kPa fluid pressure in gaps of heights ranging from 6.5 to 20 Å. The gap height is defined as the distance between the

centers of the exposed wall atoms. It should be noted that a gap height smaller than the diameter of one carbon atom ($\sigma = 3.474 \text{ \AA}$) would put the two walls in physical contact. Oscillations are seen in the solvation pressure as a function of gap height in Figure 5.2. As the solvation pressure oscillates, it crosses the x axis several times, marking gap heights where the solvation pressure is zero. Of the gap heights that have zero solvation pressure, some are stable while others are unstable. The stable points are those where the slope of the curve is negative when it crosses zero. If a perturbation in gap height were to occur and carry the system away from one of these stable gap heights, the resulting solvation pressure would work to push the gap height back to the stable point. For the unstable equilibrium points, a perturbation will be amplified by the resulting solvation pressure, and the gap height would be forced toward a neighboring stable point.

The gap height can be normalized by the size of the atoms in the simulation. By subtracting the size of one carbon atom and dividing by the size of one CH_2 group, the stable equilibrium points are seen to occur at gap heights that can accommodate integer numbers of lubricant layers (Figure 5.2 right). This signifies that the pentane lubricant lies mostly in horizontal layers parallel to the solid surface as has been seen in several other studies [159,177,178,180].

The solvation pressure can be several orders of magnitude larger than the fluid pressure (as seen in Figure 5.2). This is an important observation for understanding the balance of forces in gaps of molecular dimensions. In boundary lubrication, the pressure of the lubricant is not sufficient to carry the load [142]. Even though the bulk fluid pressure cannot carry the load, these thin lubricant films can still protect the solid surfaces from coming into contact. They are able to do this because of the huge solvation pressures obtainable in these confined geometries. For thin lubricant films, it is the solvation pressure and not the bulk fluid pressure that creates the counter force against squeezing the lubricant out of the gap. It should also be noted that the bulk fluid pressure is not defined by the load on solid asperities, but instead by the lubricant outside of the contacting asperity region. This is an important piece of information to understand the premise of the grand isostress ensemble simulations presented later.

With this understanding of the balance of forces between fluid and solid, one can estimate the equilibrium gap height (or film height) when a load is applied from the plot of solvation pressure.

If we start with a large gap filled with lubricant and apply a load greater than the fluid pressure, lubricant will be squeezed out and the gap will shrink until the load meets a solvation force high enough to balance it. For example, for the conditions of Figure 5.2 if there were a load of 250 MPa applied to a lubricant gap larger than 20\AA , we would expect the lubricant to be squeezed out until the gap shrinks to a height that has a solvation pressure large enough to counter the applied load. This occurs at a gap height of about 11\AA . We should expect the system to contract to a gap height of 11\AA at equilibrium under a load of 250 MPa.

V Effects of temperature and fluid pressure

The traditional way to represent adsorption and desorption data is the isotherm, which is a plot of the number of molecules adsorbed as a function of the fluid pressure at constant temperature. Isotherms can be calculated from GCMC simulations and are useful for evaluating thermodynamic lubrication failure. Isotherms of pentane in slits of various heights are shown in Figure 5.3. These isotherms show that at low fluid pressures, there is more pentane adsorbed in smaller slits than larger ones in spite of the difference in volume. More pentane is adsorbed in the smaller slits at low pressures because of the increased interaction with the walls. This idea agrees with the solvation pressure plot. Figure 5.2 shows that at smaller gaps the amplitude of the oscillations in solvation pressure increases. As the gap shrinks the remaining molecules can induce larger and larger pressures on the walls because they strongly interact with the solid surfaces. It becomes harder to squeeze out the molecules because they are more firmly adsorbed.

Isotherms of pentadecane were also calculated. Pentadecane has fifteen carbon atoms and is comparable in length to molecules in mineral oil, a common lubricant. The pentadecane isotherms reported in Figure 5.4 show that as temperature increases, the isotherms shift to the right. This shift shows that at higher temperatures the lubricant can desorb even at significant fluid pressures. The isotherms in Figure 5.4 show at what temperature desorption—and hence lubrication failure—might occur even when it is under high fluid pressure.

Producing isotherms from GCMC gives insight into molecular behavior important to lubrication failure. The isotherms shown here can be used to predict the fluid pressure where a critical

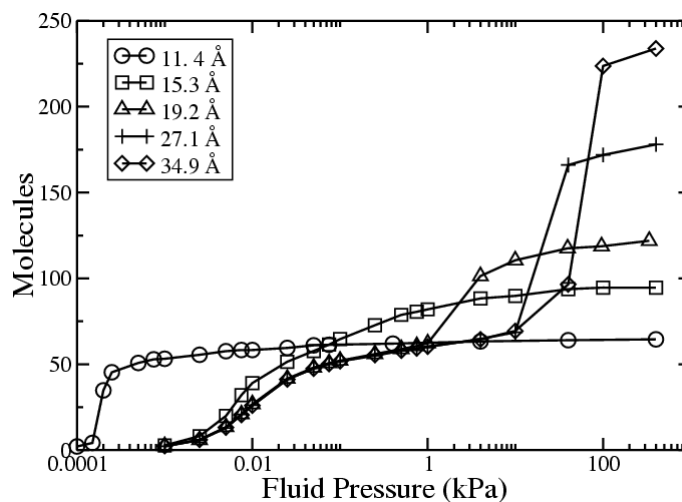


Figure 5.3: *Pentane isotherms in slits of various heights at 300 K.*

density of lubricant may be lost in the slit as gap height or temperature changes. When the lubricant density is low, it will be easier for the solid surfaces to come into contact and cause lubrication failure.

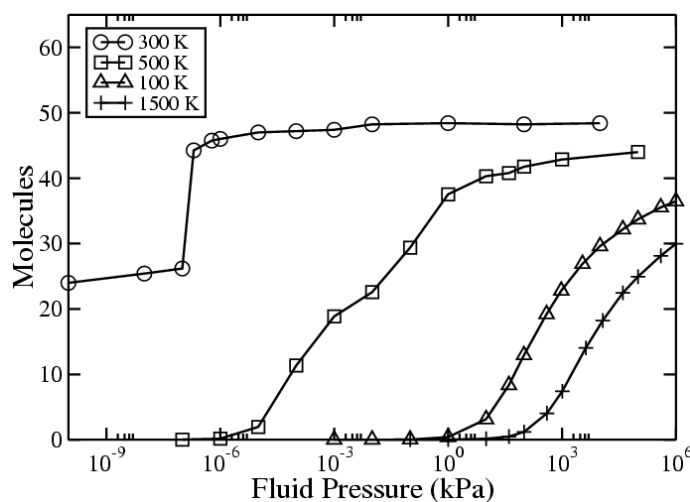


Figure 5.4: *Pentadecane isotherms in a 19.2 Å slit at various temperatures.*

VI Grand isostress ensemble methods

We would like to study the solvation pressure like in Figure 5.2 for many different lubricants, at various fluid pressures and at different temperatures. However, it is tedious to calculate the

solvation pressure at the many gap heights necessary to obtain this curve, and it is not feasible to perform all of the necessary simulations to study lubricant behavior over so many conditions. Simulations in a new ensemble, the grand isostress ensemble, can reduce the number of simulations necessary to get a picture of the solvation pressure under various conditions.

Unlike GCMC, the volume is not held constant in the grand isostress (GI), or $\mu P_{zz}AT$, ensemble. Instead the simulation cell length is allowed to fluctuate in the z direction during one of the Monte Carlo moves. A normal load (a stress normal to the walls i.e. P_{zz}) is applied to the solid walls in the simulation, and the effect of that load on the lubricant film can be studied directly. An applied load will drive the gap height to an equilibrium value where the solvation pressure balances the applied load on the walls.

The grand isostress ensemble was derived by Schoen, Diestler and Cushman [181] and has been used to study a variety of problems. The creators of the ensemble used it to study the layer thickness of simple molecules in slit pores, while other researchers have used it to simulate experiments performed with the surface force apparatus [182]. Similar ensembles that permit volume fluctuation moves have also been derived to study such phenomena as the swelling of clays immersed in water [183, 184] and the swelling of a polymer immersed in a fluid [185]. Here we have used the grand isostress ensemble to predict lubricant layer thicknesses for longer chain alkanes under various temperature/load combinations to investigate when lubrication failure may occur.

A Monte Carlo volume fluctuation move was added to the Monte Carlo moves mentioned previously. The volume fluctuation move expands or contracts the simulation volume as shown in Figure 5.5. The two solid walls are moved apart in the z direction by a random distance, and the alkanes are displaced as rigid bodies. The average gap height fluctuation attempted was 0.2\AA . The frequency of attempted gap fluctuation moves depended on the number of molecules in the simulation. One gap height fluctuation was performed for every N Monte Carlo moves, where N was the current number of lubricant molecules in the simulation. This ratio was used because every gap fluctuation causes all molecules to be moved, whereas each other move type affects only one molecule in the simulation [181]. Simulations in the GI ensemble took about the same number of Monte Carlo moves to equilibrate as the GCMC simulations. Average properties were

calculated in a similar manner.

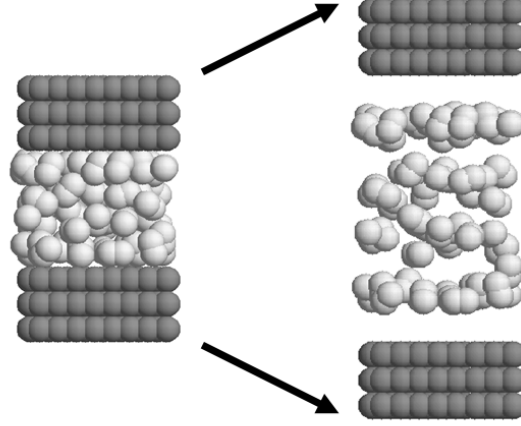


Figure 5.5: Gap height fluctuation. All molecules are spread out proportionally. The gap fluctuation shown is greatly exaggerated.

The acceptance criterion of a gap fluctuation is derived from the statistics of the ensemble. The probability that a move will be accepted is

$$P_{acc} = \min \left[1, \exp \left\{ -\beta(\Delta\mathcal{V} + P_{zz}A\Delta h) + N \ln \left(\frac{h_n}{h_o} \right) \right\} \right] \quad (2)$$

where β is $1/kT$, $\Delta\mathcal{V}$ is the change in potential energy of the system because of the move, P_{zz} is the applied stress resisting expansion, h_n is the new height of the lubricant gap, and h_o is the old height. From this acceptance criterion it can be seen how the system parameters affect the probability that a move is accepted. For example, a move which decreases the system's energy will be more likely to be accepted. Also, for a load squeezing the surfaces together, a decrease in gap height is more likely to be accepted as long as it does not cause a large increase of the system energy.

VII Grand isostress ensemble results

Results from the grand isostress ensemble can be compared with the solvation pressure plots made from GCMC simulations to check that the two methods give the same results. For example if the

Table 5.1: Initial and final average gap heights in grand isostress ensemble simulations of pentane at 300 K and 200 kPa. The grand isostress ensemble simulations with zero load equilibrate to a nearby stable equilibrium gap height that agrees with results from the GCMC simulations in Figure 5.2.

GI Initial Gap(Å)	GI Average final gap(Å)	GCMC Closest stable gap(Å)
6.70	7.42±0.09	7.48
9.00	7.48±0.09	7.48
10.50	11.61±0.15	11.62
13.00	11.65±0.13	11.62
15.50	16.10±0.20	16.24

normal load is set to zero in the GI simulations, we expect the solvation pressure to drive the gap height to a nearby stable equilibrium point. This is in fact what we see. GI simulations of pentane were performed at 300 K and 200 kPa (the same conditions used in Figure 5.2) starting from several initial gap heights. The first column in Table 1 shows the initial gap heights used in each GI simulation, and column 2 shows the stable points reached after the simulations equilibrated. In each case, the final equilibrated gap height matched the stable points found in Figure 5.2. The simulation methods agree.

It may appear that the GI ensemble predicts multiple stable equilibrium points for a single set of ensemble conditions, i.e. the simulation will settle on a different equilibrium gap height depending on the starting gap height. Schoen et al. have addressed this concern by noting that only one final gap height is actually stable; the others are metastable [181]. The distinction between metastable and stable is that the GI potential has a global minimum at only one of these equilibrium points. For the application at hand, however, both the stable and metastable points can be of interest. In the dynamic physical picture, the system may spend considerable time at or near metastable points since the path from a metastable to a stable point contains a large barrier.

Armed with the GI ensemble simulation method we can more quickly estimate the lubricant layer thickness for many temperature/load combinations and evaluate when thermodynamic driving forces may cause lubrication failure. One approach to investigate the response of a lubricant film to an applied load is to start the simulation at a rather large lubricant gap and observe how the load squeezes out the lubricant to reach an equilibrium height. If this is done at several temperatures, we can gain insight into how increased temperature can cause lubrication failure

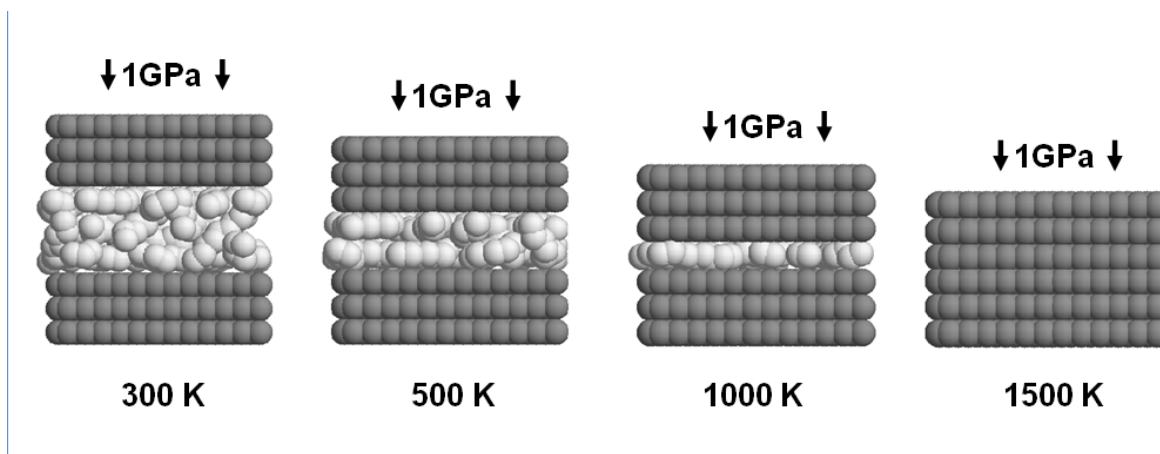


Figure 5.6: *GI simulations of pentadecane at a fluid pressure of 200 kPa and under a load of 1 GPa. Increasing temperature allows more lubricant to be “squeezed” out.*

under a particular load. Figure 5.6 shows that under a load of 1 GPa, an increasing amount of pentadecane is squeezed out as the temperature increases. At some temperature between 1000 K and 1500 K all of the lubricant is squeezed out, representing lubrication failure.

Figure 5.7 is a three dimensional plot showing the effects of both temperature and applied load on the equilibrium lubricant layer thickness. By following the axes on this graph one can see how the pentadecane is affected by increasing temperature at constant load and also how increasing the load affects the pentadecane film at constant temperature. When the whole plot is considered together, it maps out a thermodynamic failure regiona region where the combinations of temperature and load allow all of the lubricant molecules to be squeezed out. This region could be used to evaluate appropriate operating conditions for a particular lubricant/surface pair.

By considering Figure 5.7 in conjunction with the isotherms in Figure 5.4, a richer understanding of lubrication failure can be obtained. Figure 5.7, which was calculated for a fluid pressure of 200 kPa, shows that at 300 K extremely high loads—upward of 10,000 MPa—are required to force pentadecane completely out of the gap. Figure 5.4 shows that in a slit fixed at 19.2 Å, pentadecane forms a dense lubrication layer at 200 kPa and 300 K. The dense lubricant layer is firmly adsorbed and adamantly resists the applied load. To contrast, at the much higher temperature of 1500 K, very little pentadecane is adsorbed at 200 kPa (Figure 5.4). This small amount of lubricant is forced out of the gap with relative ease under an applied load of only 300 MPa as seen

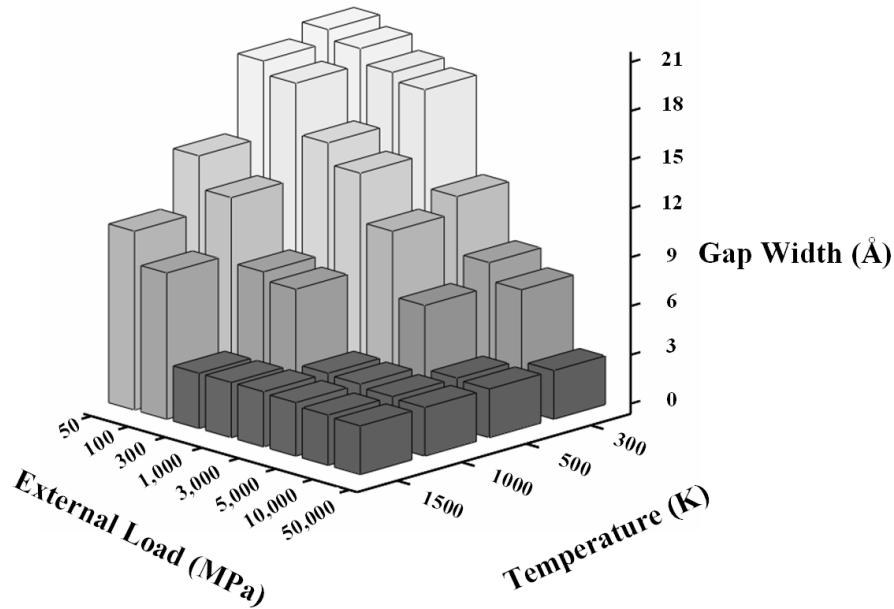


Figure 5.7: Lubrication gap for several temperature-load combinations for pentadecane at 200 kPa. Gaps less than 4 Å have no lubricant molecules in them.

in Figure 5.7. From this analysis we see that failure will occur at a much lower load if the corresponding isotherm shows that there is only a small amount of lubricant in between the asperities at a fixed gap height and the corresponding fluid pressure. This shows that temperature spikes greatly decrease the ability of the lubrication layer to protect the solid surfaces under an applied load.

VIII Conclusions

Monte Carlo simulations have been used to assess the equilibrium state of a lubricant confined between asperities. The influences of load, temperature and fluid pressure were each evaluated. Simulations in both the grand canonical and grand isostress ensembles illuminated lubricant behavior determined by the thermodynamic driving forces present. In many cases the thermodynamics will drive the lubricant out of the gaps between asperities—a condition that will likely lead to lubrication failure. Grand isostress ensemble simulations can test specific temperature/load

combinations in a single simulation and thus present a much quicker way to investigate failure behavior than GCMC simulations.

Acknowledgments: We express our gratitude to the NSF for an Integrated Graduate Education, Research and Training grant (IGERT) on Virtual Tribology. We would also like to acknowledge Professor Jane Wang for helpful discussions on lubrication failure.

The single component adsorption of alkanes in carbon slit pores was studied using configurational biased grand canonical Monte Carlo simulations. Wide ranges of temperature, pressure, alkane chain length and slit height were studied to evaluate their effects on adsorption. Adsorption isotherms and density and orientation profiles were calculated. The behavior of long alkanes at high temperatures was found to be similar to short alkanes at lower temperatures. This suggests that the isotherms may be related through the Polanyi potential theory.



Monte Carlo simulation of n-alkane adsorption isotherms in carbon slit pores

I Introduction

The adsorption of alkanes and the molecular structure of alkane films are important to a wide variety of applications including lubrication [186, 187], adhesives [188, 189], the purification and storage of natural gas [168, 190], and catalytic cracking of crude oil [191, 192]. In each of these applications the adsorption and structure of carbon-chain-based molecules in confined spaces is critical to the overall performance of the intended operation.

In recent decades, computer simulation has become an indispensable tool to study molecules in confined spaces. Increased computational speed and better molecular modeling algorithms allow simulations of larger systems and with increasing accuracy. Simulation studies are well suited to explore the effects of a wide range of system conditions since this merely requires changing the input parameters. An experimental study, on the other hand, may be limited to a small range of temperature and pressure due to the limitations of the particular experimental apparatus

used. Simulations also provide the ability to observe the atomic details of adsorption including the molecular packing and structure of the adsorbate, which are difficult to obtain experimentally.

A common geometry used in molecular simulations of adsorption is the slit pore, consisting of two flat surfaces at a fixed distance with the open sides treated with periodic boundary conditions. Slit pores serve as a simple model of activated carbons, which are widely used in industrial adsorption separations. In addition, this simple geometry lends itself to fundamental studies that focus on general trends rather than the behavior of a particular adsorbent structure. In recent years, molecular simulations of adsorption have focused largely on detailed atomistic models of more complicated structures such as zeolites [173, 193–196], carbon nanotubes [197], metal-organic frameworks [198, 199], and more realistic models of heterogeneous activated carbons [200, 201]. Because many of the simulations of adsorption in slit pores were performed when computers were much slower and newer algorithms did not exist, they were performed exclusively for small, simple molecules that are essentially spherical in shape. There are, therefore, no reports in the literature for adsorption isotherms of longer n-alkanes in the important slit-pore geometry.

Adsorption isotherms for n-alkanes in carbon slit pores may shed new light on experimental studies of adsorption of chain molecules in activated carbon [202–204]—materials that are widely used in purification processes. Molecular simulation allows us to easily cover a wide range of alkane chain length, slit pore height, and system conditions such as temperature and pressure. In addition, isotherms in idealized slits may serve as a useful comparison to classify adsorption in new adsorbent materials where the pore size and chemistry can be tailored for specific purposes. Zeolites, carbon nanotubes and metal organic frameworks now allow uniform pore structures throughout the adsorbent with tailored pore size, shape, and chemistry.

It should be pointed out that there have been numerous molecular dynamics simulations for chain molecules in slit pores [187, 205–208], and these simulations have generated much insight into the dynamic behavior and structure of chain molecules in slit pores. These simulations, however, require the density of molecules within the slit as an input. The Monte Carlo simulations reported here calculate the density within the pores corresponding to a given temperature and the

pressure of the fluid outside the slit. There have also been some Monte Carlo studies modeling the surface forces apparatus which calculate the solvation pressure generated by confined alkane films [179,209,210]; however, these studies do not report the isotherms either.

II Molecular model

The simulation cell used in this study is a slit pore with walls made of three layers of graphitic carbon. Unlike some studies where the walls are a continuum, the walls in this study are made up of discrete carbon atoms. The edges of the simulation cell not bounded by the graphite wall are treated with periodic boundary conditions.

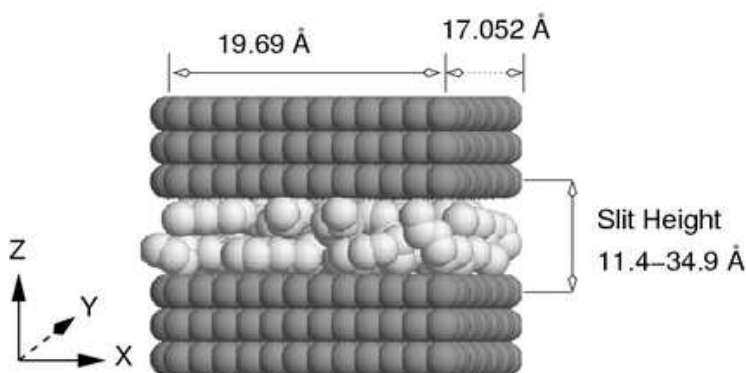


Figure 6.1: *Slit pore unit cell. The slit height is measured from carbon center to carbon center. Note that the simulation cell usually contains several unit cells.*

We have found it useful to define a slit pore unit cell in order to compare the results from simulation cells of different volumes. Each unit cell has a constant area, but a range of slit heights are used. The dimensions of one unit cell are shown in Figure 6.1. The wide range of system conditions explored produced a wide range of densities within the slits. For conditions where low densities were expected, as many as eight unit cells were connected side-by-side to increase the simulation cell volume and hence the number of molecules in the simulation. For simulations

Table 6.1: *Alkane and slit wall interaction parameters*

Nonbonded	$(\epsilon/k_B)/K$	$\sigma/\text{\AA}$		
CH ₃ –CH ₃	98.1	3.77		
CH ₂ –CH ₂	47.0	3.93		
CH ₃ –CH ₂	67.9	3.84		
C–CH ₂	47.45	3.70		
C–CH ₃	68.55	3.62		
Bond angle	$k_\theta/\text{kcal rad}^{-2}$	θ_0/deg		
CH _x –CH ₂ –CH _x	62.1	114		
Torsion	$(a_0/k_B)/K$	$(a_1/k_B)/K$	$(a_2/k_B)/K$	$(a_3/k_B)/K$
CH _x –CH ₂ –CH ₂ –CH ₂ –CH _x	0.0	355.0	-68.2	791.3

where very high densities were expected, sometimes only two unit cells were needed to ensure an appropriate number of molecules in the simulation for good statistics. For the majority of the simulations, where system conditions were not extreme, the simulation cell consisted of four unit cells. The alkane molecules were represented with the united atom model—each carbon and its bonded hydrogen atoms were modeled as one Lennard-Jones sphere. For alkanes longer than ethane, the molecules were flexible and had potentials to allow bond bending and torsional flexibility. The bond lengths, however, were fixed. Bond angle bending was modeled with a harmonic potential.

$$\mathcal{V}(\theta) = k_\theta(\theta - \theta_0)^2 \quad (1)$$

Torsional flexibility was treated with the cosine expansion model.

$$\mathcal{V}(\phi) = a_0 + a_1[1 + \cos(\phi)] + a_2[1 - \cos(2\phi)] + a_3[1 + \cos(3\phi)] \quad (2)$$

The Lennard-Jones potential was used to calculate the interaction between non-bonded atoms. The interaction parameters used in this study were taken from previous simulations of n-alkanes [173, 174] and are shown in Table 6.1.

III Simulation method

Configurational-biased grand canonical Monte Carlo (CB-GCMC) simulations were used to evaluate equilibrium conditions of the alkanes in the slit pores. Grand canonical Monte Carlo operates in the constant μVT ensemble. The simulation volume is in equilibrium with a bulk reservoir of molecules at the system temperature and chemical potential. For ease of use, the fugacity is used instead of the chemical potential as an input to the simulations. When the chemical potential of a species in two phases is equal, the fugacity of the species in the two phases is equal as well. The fugacity of the alkane adsorbate was calculated from the bulk fluid pressure and the system temperature using the Peng-Robinson equation of state. In the grand canonical ensemble, the number of molecules in the simulation is allowed to fluctuate. The average density equilibrates as the simulation progresses, and the density of molecules in the simulation volume corresponds to the amount adsorbed at the system conditions. Monte Carlo simulations produce millions of configurations of molecules which can be used to calculate ensemble averages for properties of interest. These configurations are produced as a Markov chain by the Metropolis method [175], where the next configuration of molecules is derived from the current configuration by attempting one of a variety of Monte Carlo move types. In the GCMC simulations used here, four move types were implemented, which were taken from Macedonia and Maginn.³⁰ The types of moves used were insertions, deletions, translations, and cut-and-regrow moves. The molecular insertions have a configurational bias (CB). The biased insertions increase the efficiency of insertions into a dense adsorbate film. Without a CB, the acceptance of a random insertion of a long chain would be prohibitively rare. The CB algorithm inserts one united atom at a time and each insertion is biased toward the more energetically favorable positions. A Rosenbluth weight is accumulated as each atom is inserted, and the weight is considered in the acceptance of the move so that the bias of the insertion is offset. Deletions are also weighted to remove the bias introduced by the insertions. The cut-and-regrow move deletes a portion of an alkane molecule and regrows the deleted portion using a CB with new internal degrees of freedom. For each simulation between five and ten million Monte Carlo moves were attempted. 75% of the moves were insertions and deletions, 12.5% were translations and 12.5% were cut-and-regrow moves. Results were obtained by aver-

aging properties of configurations generated in the last 3 million moves. The Monte Carlo code used in this study was an extension of an object-oriented multipurpose simulation code (MUSIC) developed for porous materials [176].

IV Results

A Density and orientation profiles

The configurations generated from the simulation were analyzed to determine the average position and orientation of the molecules in the adsorbed alkane films. Density profiles were created by sorting the molecules according to the distance of their center of mass from the nearest wall and averaging the number of molecules found at each distance over all configurations considered. The orientation of the molecules in the slit was evaluated using the following order parameter:

$$S = \frac{3\langle \cos^2 \alpha \rangle - 1}{2} \quad (3)$$

Here α is defined as the angle between the head-to-tail vector of the alkane molecule and the Z axis (Figure 6.1). The orientation parameter takes a value of 1 if all of the molecules are aligned perpendicular to the wall, a value of -1/2 if they are all parallel to the walls and a value of 0 if they are randomly oriented.

Like previous studies of small molecules, our simulations show that shorter n-alkanes such as ethane form ordered layers in slits of molecular dimensions [180, 185, 211–213]. The density profiles for ethane at moderate pressures in Figure 6.2 show that molecules lay in distinct layers within the slit. The number of layers is determined by the slit height. The orientation order parameter shows that the molecules in each layer are ordered and lay parallel to the walls ($S < 0$). The layers decrease in density and order with distance from the wall. Pentane also forms layers between the slit walls as seen in Figure 6.3. The density profiles of pentane for the same series of slit heights look similar to those for ethane except for one feature; a small secondary peak can be seen in between each of the much larger peaks. The orientation profiles show that molecules with their centers of mass in these small bumps have an orientation parameter greater than zero, indi-

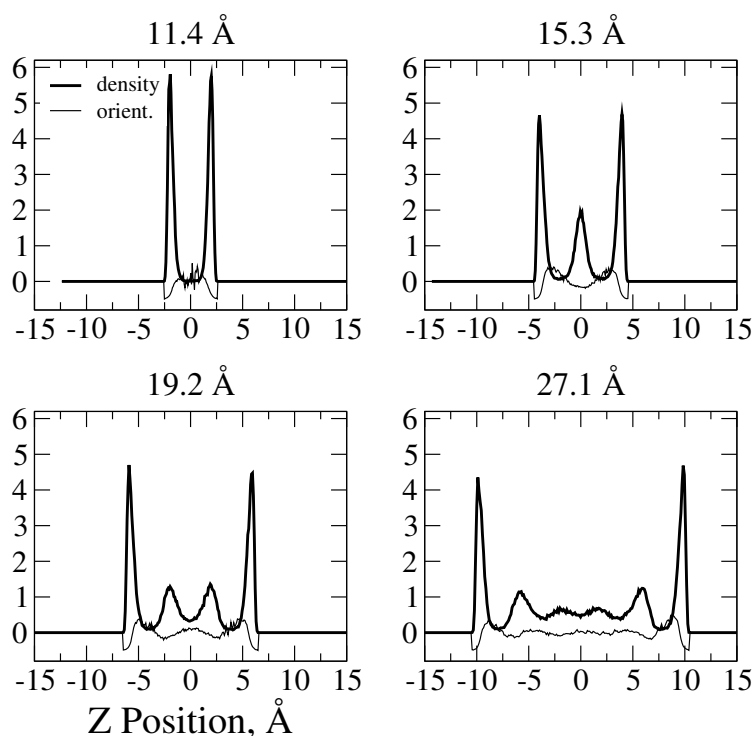


Figure 6.2: Ethane density and orientation profiles at 300 K and 10,000 kPa for slits of different heights. Layers form parallel to the slit walls and the number of layers increases as the gap increases. Density is reported in units of molecules per cubic angstrom.

cating that their orientation is more perpendicular than parallel to the walls. These few molecules span from one layer to the next and have CH_X groups belonging to two layers. The number of pentane molecules which span layers is only a small fraction of the molecules in the simulation volume, but they can have a large influence on properties like viscosity or the strength of the thin film—properties important to lubrication and adhesion. For example, the viscosity of long alkanes has been observed to decrease with increasing shear velocity [207,214]. This phenomenon known as shear thinning occurs in part because interdigitation is seen to decrease when the velocity is increased.

For longer alkane molecules the layering and orientational order is less distinct but still present. This may be attributed to the greater flexibility of the longer molecules and the ability of a single molecule to bridge between two or more layers. The orientation parameter loses some meaning as the molecules become so long that they are often bent or curled. The head-to-tail vector has less

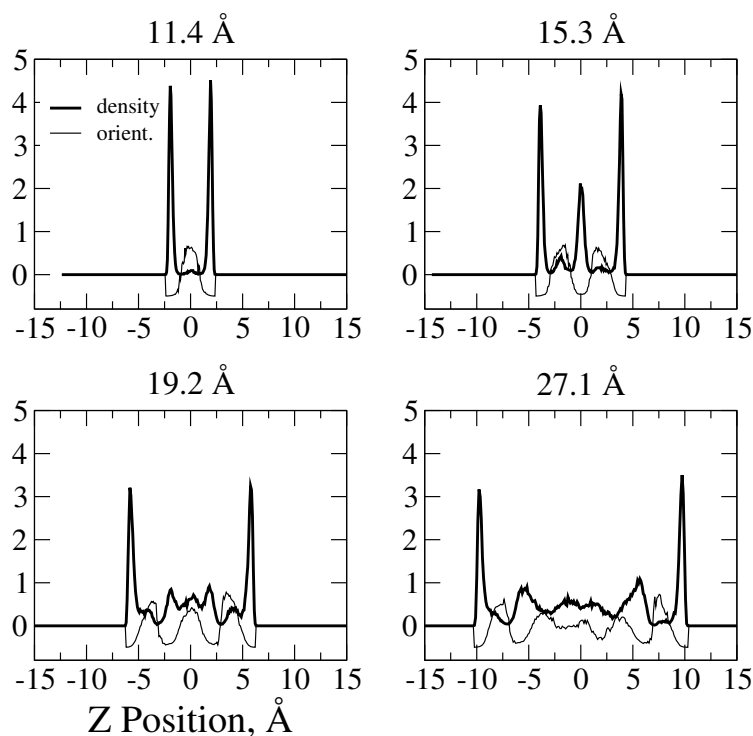


Figure 6.3: Pentane density and orientation profiles for slits of different heights at 300 K and 400 KPa.

relevance to the orientation of the molecule in this case. Other studies have measured the orientation of individual bond vectors for very long molecules adsorbed near a planar surface. Some amount of order can be seen with this alternate method of analysis [215]. The density profiles and the order parameter calculated by Equation 3 generally show order in the form of layers across the slit. However, the structure of the molecules in any layer does not show significant order. Their structure within a layer is amorphous rather than crystalline.

Figure 6.4 shows the progression of pentane layer formation as pressure is increased. The layers nearest the walls form at much lower pressures than the layers near the center of the pore. Molecules adsorb onto the solid walls until the walls become covered. When the walls are mostly covered and do not have enough free space for another molecule to adsorb lying flat, a few molecules adsorb with only a few CH₃ near the wall, the rest of the molecule projecting out into the empty pore. This can be seen in Figure 6.5 and seems related to a dynamic study by Xia and Landman where the tail of an alkane chain is seen to adsorb before it lays fully next to the wall [216]. The layers directly adjacent to the walls essentially reach their full density before

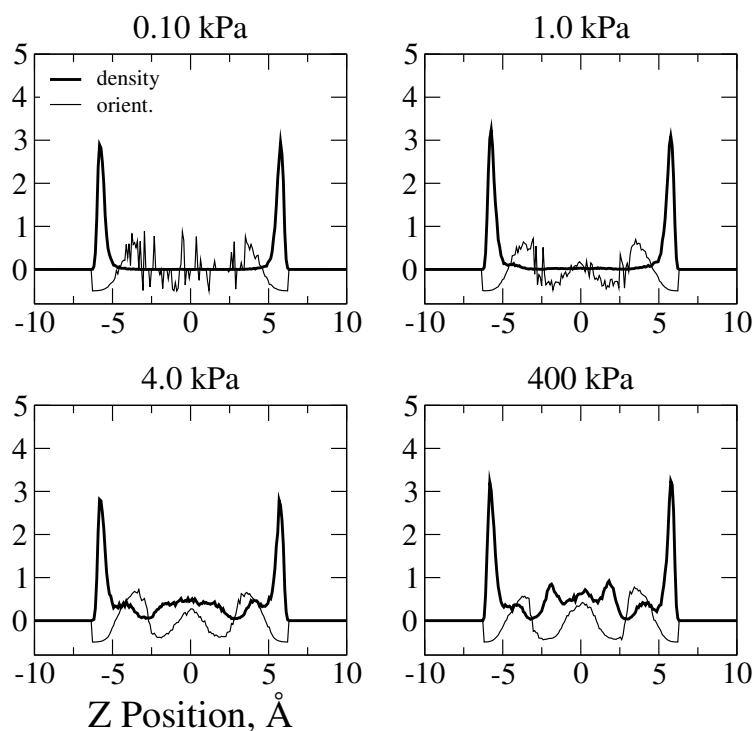


Figure 6.4: *Pentane density and orientation profiles in a 19.2 Å slit at 300 K and varying pressure.*

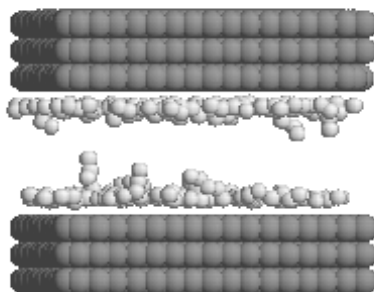


Figure 6.5: *Pentane at 300K and 1.0 kPa in a 19.2 Å slit. This pressure is just below the abrupt filling of the center of the pore. A few pentane molecules have a head or tail contacting the wall but extend out into the empty pore. (Note that adsorbate atoms are not shown with a full LJ radius.)*

the inner layers even begin to form. The inner layers then form rather abruptly at a much higher pressure. The density and orientation profiles of pentane look somewhat different at higher temperatures. The high temperature disrupts the ordered layers that are seen at lower temperatures. Figure 6.6 shows a side-by-side comparison of profiles for pentane at 300 K and 1500 K. The pres-

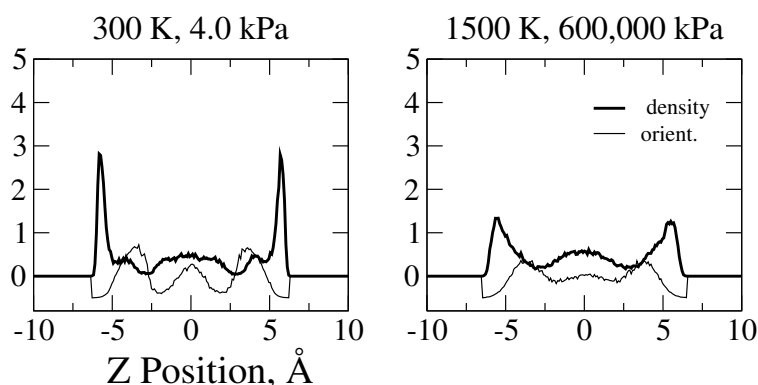


Figure 6.6: Pentane density and orientation profiles in a 19.2 Å slit at 300 K and 1500 K. Pressures were chosen so that the average density of the two systems was the same. Pentane layers are less discrete as temperature increases.

tures of the two systems were chosen so that the average densities of the systems were the same. The profile at 1500 K shows that the layer of molecules near the wall is not nearly as dense and the layer is spread out over a larger distance away from the wall compared to the profile at 300 K. The orientation profile shows that in the middle of the pore, molecules are no longer ordered but extend in random directions. The clear decrease in order represents the increased importance of entropic effects at higher temperatures.

B Isotherms

Isotherms for ethane, pentane and decane were calculated from GCMC simulation for pores with slits ranging from 11.4–34.9 Å in height at 300 K. The results are shown in Figures 6.7,6.8,6.9. For each alkane, adsorption at the lowest pressures occurs only in the smallest slit. Adsorbed molecules in the smallest slits can interact with both walls, making adsorption very favorable energetically. The isotherms in the two smallest slits are type I isotherms in the IUPAC classification, typical of micropores.⁴²

For slit pores of 19.2 Å and larger the shape is different. For these isotherms there are two regions where the density rapidly increases in the isotherm. The first rise corresponds to the formation of a molecular layer adjacent to the slit wall as discussed above. The second abrupt rise in density corresponds to the filling of the center of the pore. The shape of these isotherms—

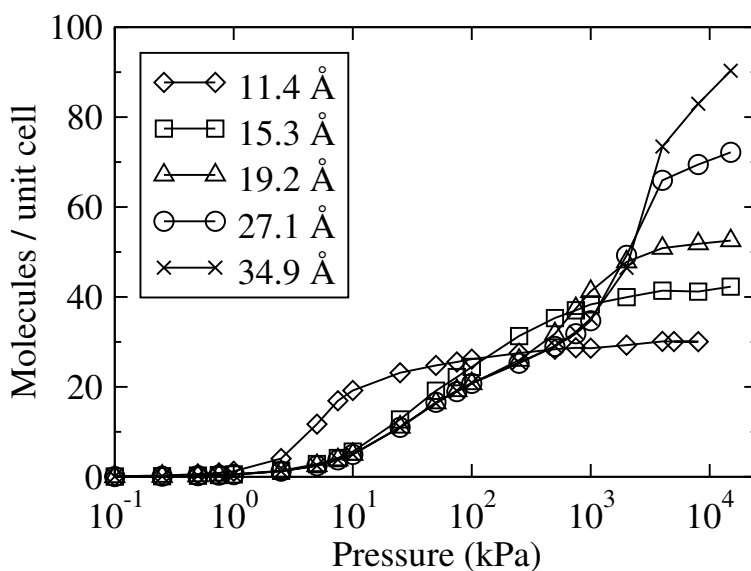


Figure 6.7: Ethane isotherms at 300 K in slits of various heights

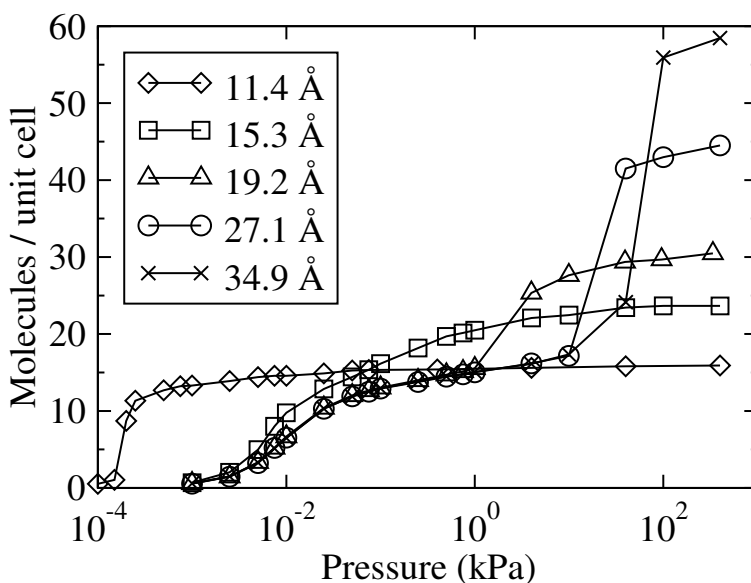


Figure 6.8: Pentane isotherms at 300 K in slits of various heights

typical of mesopores—is classified as a type IV isotherm by the IUPAC. Experimental isotherms for n-alkanes in activated carbon [202–204] generally display type I isotherms, without steep increases, even though they usually contain both micro and mesopores. This is attributed to the heterogeneity of the materials, which comes from the distribution of pore sizes, the edges of the graphite sheets, and chemical heterogeneity. One common feature of type IV isotherms is hys-

teresis. Adsorption hysteresis refers to a system for which the adsorption isotherm differs from the desorption isotherm. Hysteresis is usually manifest in mesopores at pressures around a pore condensation event [171]. The isotherms displayed in Figures 6.7, 6.8, 6.9 were calculated using the final configuration at a given pressure as the starting configuration for the simulation at the next point on the isotherm, moving from low pressures to high pressures (adsorption direction). To check for hysteresis we calculated desorption isotherms for the 27.1 Å slit for ethane, pentane, and decane. No hysteresis was detected in the isotherms for ethane or pentane. This does not necessarily mean that there is no hysteresis in the isotherm, but if there is a hysteresis loop it is smaller than the pressure increment used in the isotherm. Hysteresis was detected in the decane isotherm as shown in Figure 6.10. Adsorption isotherms for ethane, pentane, decane, and pentadecane are compared in Figure 6.11 for a 19.2 Å slit at 300 K. Several trends can be seen. As expected, the longer alkanes undergo pore filling at much lower pressures than the shorter ones. Similarly, adsorption initiates at a lower pressure as alkane length increases. The smaller molecules, of course, achieve a higher molecular density in the slit at saturation since they occupy less volume per molecule. When the density is reported in carbon atoms per unit cell, a feel for the mass density can be gained. The longer chains achieve the highest densities of carbon atoms in the slit. This is logical considering that the bond length between carbons is shorter than the equilibrium Lennard-Jones distance between methyl or methylene groups. Another trend is that the shape of the isotherm changes as chain length increases, with the width of the plateau in the middle of each isotherm increasing with alkane length. This plateau represents a region where the walls are covered with molecules but the center of the slit is still empty. For the longer molecules, there are several orders of magnitude in pressure between the initial adsorption on the walls and pore filling.

C Effect of temperature

Temperature, of course, also has an important effect on the isotherm. In order to study this effect, pentane isotherms were computed for temperatures ranging from 300K to 1500K and are shown in Figure 6.12. As expected, at any given pressure the density of pentane in the slit decreases as

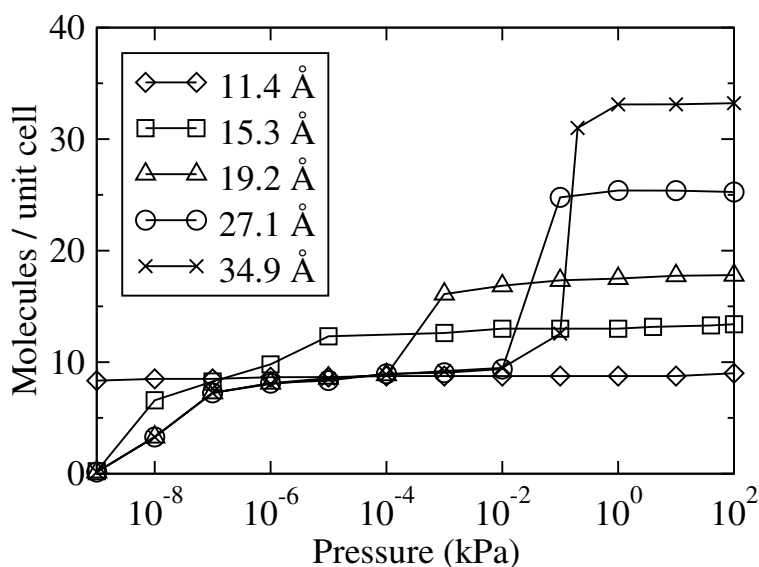


Figure 6.9: Decane isotherms at 300 K in slits of various heights

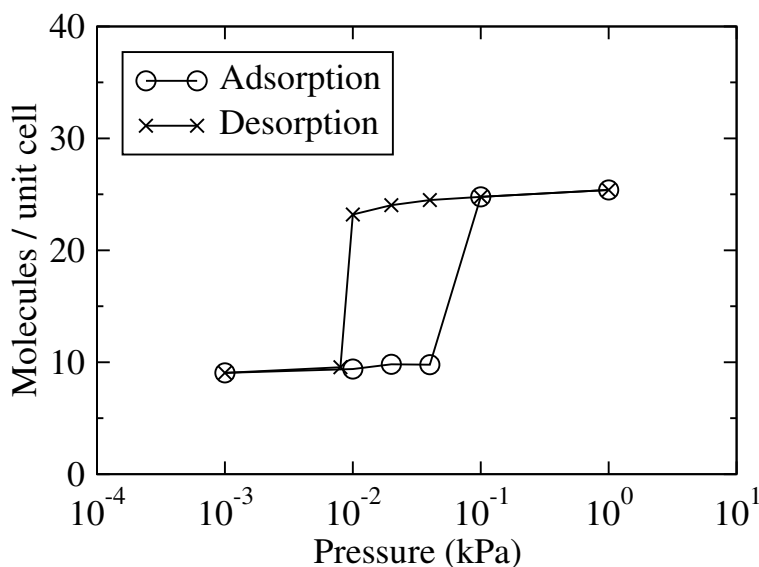


Figure 6.10: Hysteresis between the adsorption and desorption isotherms for decane in a 27.1 Å slit at 300 K.

temperature increases. The plateaus in isotherms found at low temperatures disappear as temperature increases. Snap-shots of configurations and the density profiles for points along an isotherm at higher temperatures show that the slit fills in a different manner than at the lower temperatures. The molecules are found more evenly distributed throughout the pore volume at higher temperatures, and there is no longer a point in the isotherm where only the walls are covered

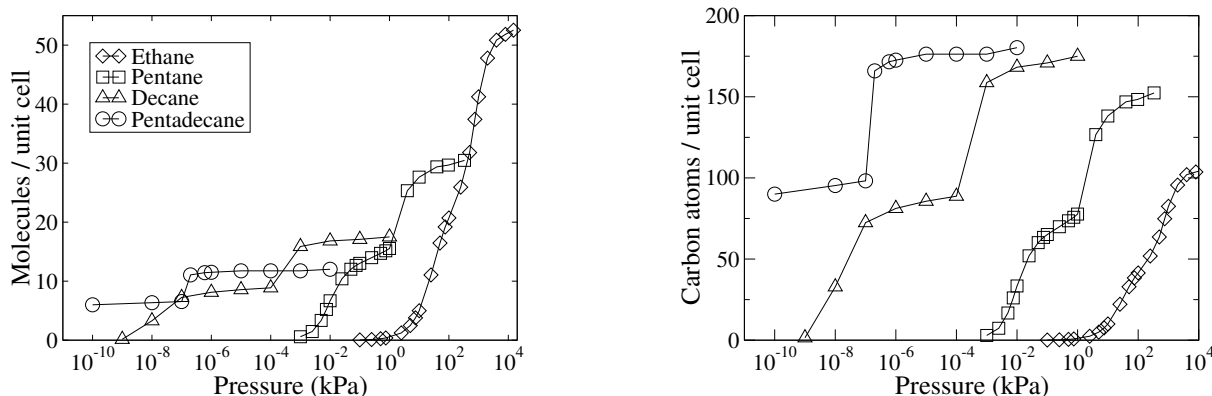


Figure 6.11: Comparison of isotherms for alkanes of different lengths. Each isotherm is for a 19.2 slit at 300 K. Density is reported in both molecules per unit cell (left) and carbon atoms per unit cell (right).

with molecules and the center of the pore is empty. The elevated temperature allows molecules to reside anywhere in the pore even at low loadings. At extremely high pressures, above the bulk critical pressure of pentane, the isotherms again begin to rise. The fugacity of pentane at these high pressures increases rapidly with increasing pressure, which causes the increased density in the simulation. The density of the pentane in the slit pore in the extremely high pressure regime converges for all of the temperatures simulated, and the density in the slit approaches the density of bulk pentane (as calculated by the Peng-Robinson equation of state). The effects of the extreme pressure dominate over the effects of temperature and the energetics of the pore, so that the properties of the confined fluid converge with the bulk properties. Isotherms for pentadecane at increasing temperatures were also calculated in the 19.2 slit as shown in Figure 6.13. Many important lubricants have chain lengths comparable to pentadecane. The adsorption of lubricant molecules is important to protect solid surfaces from wear during sliding. Considerable temperature spikes can occur in tribological applications, and temperature-induced desorption is commonly thought to be a major contributor to lubrication failure [141,186,217].

The shapes of some of the pentadecane isotherms are very similar to the shapes of some of the pentane isotherms except at lower temperatures and pressures. For example compare the shape of the pentadecane isotherm at 500 K in Figure 6.13 to the shape of the pentane isotherm at 350 K in Figure 6.12. Furthermore, the isotherm for ethane in the 19.2 Å at 300 K in Figure 6.11 also has this shape. The relationship between the adsorption isotherm and temperature, pressure and

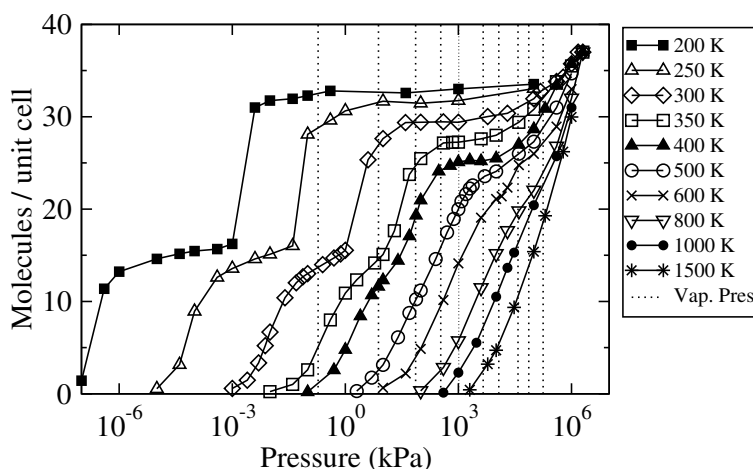


Figure 6.12: *Pentane isotherms at various temperature in a 19.2 Å slit*

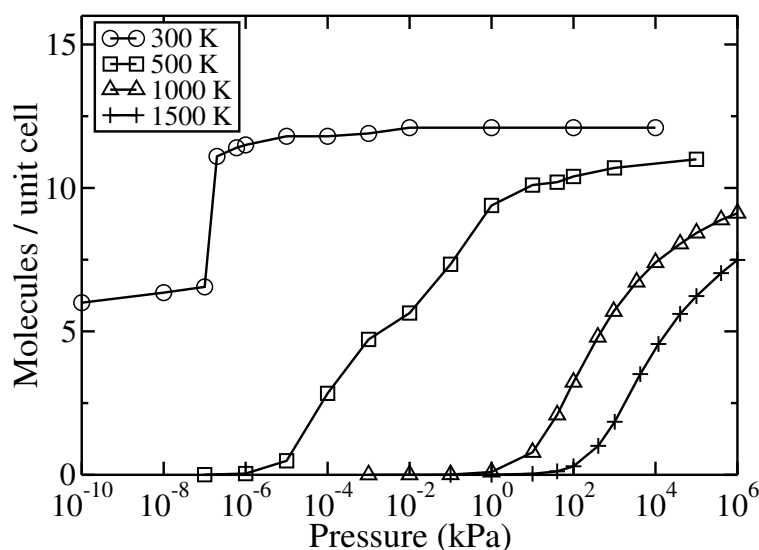


Figure 6.13: *Pentadecane isotherms in a 19.2 Å slit for temperatures from 300 to 1500 K*

adsorbate-adsorbent interaction strength has been analyzed for nearly 50 years using the Dubinin and Raduschkevich theory or modifications to it [218,219]. These theories are based on a parameter called the adsorption potential, ϵ , which was first defined by Polanyi and which characterizes the strength of the field near a surface:

$$\epsilon = RT \ln \left(\frac{P_s^i}{P_i} \right) \quad (4)$$

The adsorption potential represents the work required to compress the solute from its par-

tial (P_i) pressure to its vapor pressure (P_s^i). According to the D-R theory, loadings for a single adsorbate-adsorbent pair at a range of temperatures should collapse to fall on one characteristic curve when plotted against the adsorption potential. The D-R theory has been shown to fit adsorption data well for microporous media which have type I isotherms. Because of the similarities of isotherms at different temperatures noted above, we attempted to apply the D-R theory to our data even though the isotherms in Figure 6.12 are not all type I and 19.2 \AA is on the border between microporous and mesoporous. As Figure 6.14 shows, the theory is only partially successful for the data of Figure 6.12. The collapse is good at the highest and lowest loadings, but it is poor in the region of abrupt pore filling ($-15 < \epsilon < 5 \text{ kJ/mol}$ in Figure 6.14). This is not surprising since pore condensation is not present in type I isotherms. The correlation is encouraging and suggests that a modification of the D-R theory for type IV isotherms may be possible.

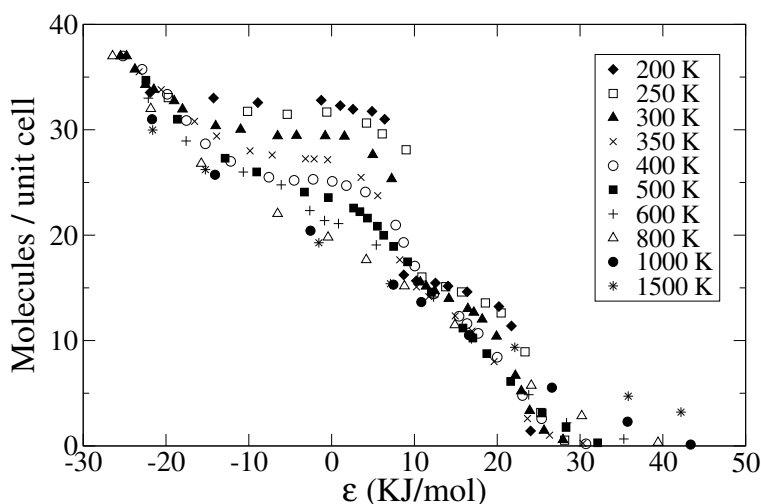


Figure 6.14: Loading as a function of ϵ for pentane in a 19.2 \AA slit. In Polanyi and D-R theory, these data points should all fall on the same curve.

Application of some of the D-R collapsing principles to isotherms of different adsorbates which have similar shapes results in somewhat more success. As mentioned previously, the isotherms of ethane at 300 K, pentane at 350 K and pentadecane at 500 K have a similar shape but are on different scales of pressure and molar density. In order to normalize the density scale, we have chosen to divide by the loading at the bulk saturation pressure of each species. This puts each isotherm on the same scale which we call the percent saturation. The pressure axis was converted to the

adsorption potential and normalized by dividing by an affinity coefficient (β) for each adsorbate. As the name suggests, the affinity coefficient represents the affinity of the adsorbate to the adsorbent. Affinity coefficients have been found to correlate to factors such as the critical temperature, molecular parachor, polarizability [220], or the molar volume at the normal boiling point [221]. We have found that taking β inversely proportional to the saturation loadings collapses the data very well. The β 's used in Figure 6.15 were calculated by dividing a reference value by the saturation loading of each component. The reference value used was the saturation loading for pentane, and the values of β for ethane, pentane and pentadecane used were 0.53, 1.00, and 2.67, respectively.

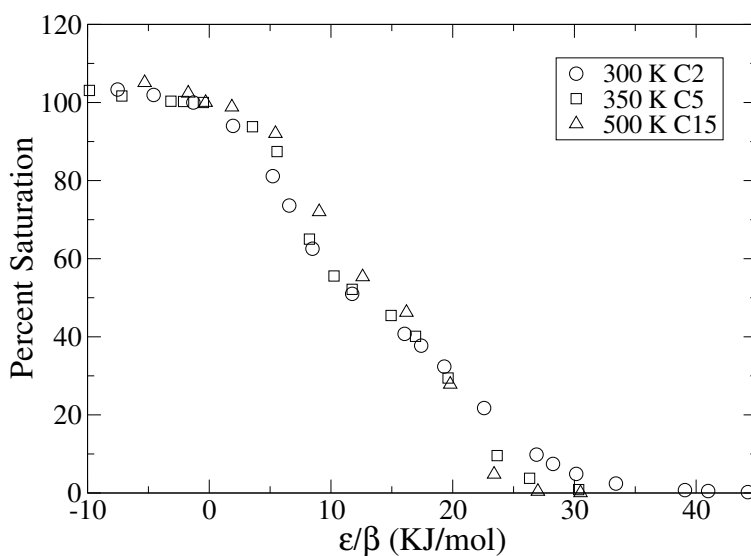


Figure 6.15: An ethane, pentane and pentadecane isotherm can be collapsed onto the same curve using principles from D-R theory.

V Conclusion

Adsorption isotherms for normal alkanes in ideal slit pores have been calculated using CB-GCMC. The behavior of alkanes in idealized pores should serve as a valuable reference system for investigations of adsorption in activated carbons, lubrication, and adsorption in more complex geometries. The effects of alkane chain length, temperature, pressure and slit height on density and molecular ordering have been determined. Isotherms have been reported for alkanes ranging from ethane to pentadecane. There is a strong similarity in the shape of the isotherms and density

and orientation profiles across the range of alkanes and temperatures studied.

Acknowledgments The authors thank K.S. Walton, C.L. Cavalcante, and R. Staudt for helpful discussions and the U.S. National Science Foundation for funding through the IGERT program and through grant CTS-0302428.

Several examples of the effects of friction and adhesion in granular flows are shown in this dissertation. The simulations and experiments isolate the effects of surface forces and find direct links to macroscopic behavior. The effects of friction and adhesion change with the length scale of the particles. Conclusions from the individual chapters are drawn here and then more general conclusions are drawn from the connections between chapters. Finally, recommendations are given to continue this line of work and expand it to new types of problems.

7

Conclusions

I Specific

Conclusions from chapter 2 Even nanoscale differences in the surface roughness of a granular material can change its macroscale behavior. Increasing the surface roughness from an rms roughness of about 50 nm to about 250 nm has a large effect on particle behavior. The angle of repose in a rotating drum is greater for rough particles than for smooth particles over a wide range of rotation rates. Experiments mixing different concentrations of rough and smooth particles show that the angle of repose increases with the concentration of rough particles. It is logical to conclude that the increase in the angle of repose is due to an increase in the inter particle frictional forces. However, the connection between increasing surface roughness and increasing friction was difficult to establish experimentally. By simulating this same system with particle dynamics, the dependence of the angle of repose on frictional forces became clear. In fact the friction coefficient was the only particle property in the simulations capable of capturing significant changes in the angle of repose.

Even though the angles of repose of the rough and smooth particles differed substantially, seg-

regation could not be observed in either a quasi-two-dimensional tumbler or in three-dimensional tumblers. The absence of segregation both experimentally and computationally suggests that the segregation mechanisms based solely on the angle of repose need to be reconsidered. A difference in the angle of repose between the two species may be necessary for segregation but is clearly not sufficient alone. Surface roughness, friction and the angle of repose do not by themselves cause segregation.

Conclusions from chapter 3 Chapter 3 connects the behavior of bulk properties of a binary mixture of particles to the interaction strength between the two particle types and their concentration in the mixture. Previous to this study, no connections of this type had been made for granular materials. Chemical solutions are often characterized in this manner suggesting that parallels may be used for granular mixtures.

A chemical solution which displays a linear dependence in its properties as a function of concentration is called ideal. Depending on the heterogeneous interaction (A-B), the bulk properties of a granular mixture can be classified as ideal or can display either positive or negative deviations from ideality as a function of concentration. This classification scheme is shown to work well to describe the angle of repose for mixtures of particles differing by frictional and adhesive properties. It also describes the behavior of the effective viscosity of a sheared granular mixture. The study of other properties of granular mixtures (e.g. packing densities, rheology, ease of fluidization etc.) could benefit from an analysis using this same structure, the structure of solution theory.

Application of solution theory could provide a way to predict the properties of the bulk powder given the properties of the particles, or possibly even facilitate the reverse analysis—providing a way to estimate individual particle interactions based on the bulk behavior of a mixture.

Conclusions from chapter 4 Small adhesive particles show promise to developing a novel damping medium. The resulting damper has the advantage of temperature insensitive operation over dampers relying on a viscous fluid. Adding energy dissipation due to adhesion hysteresis to the JKR model of adhesive contact provides a relationship which can be input onto particle dynamics

simulations. With the new model the damping performance of micro particles was studied.

The damping performance of the micro powder is affected by the energy release rate of both loading and unloading. The packing density—a parameter easily controlled in experiment—also significantly affects damping performance. The simulation results offer evidence that micro or nano particles can be used as a novel damping medium which dissipates energy through adhesion hysteresis. This simulation method and model promise to provide a useful tool to design particle dampers based upon this or other damping mechanisms.

Conclusions from chapter 5 Monte Carlo simulations are used to assess the equilibrium state of a lubricant confined between asperities. The influences of applied load, temperature and fluid pressure are each evaluated. Simulations in both the grand canonical and grand isostress ensembles illuminated lubricant behavior determined by the thermodynamic driving forces present. In many cases the thermodynamics will drive the lubricant out of the gaps between asperities—a condition that will likely lead to lubrication failure. The thermodynamics of the confined lubricant are more likely drive the system to failure when the temperature and load are high and the fluid pressure is low. The simulation results show the relative importance of these factors and specific cases of thermodynamic lubrication failure. Grand isostress ensemble simulations can test specific temperature/load combinations in a single simulation and thus present a much quicker way to investigate failure behavior than GCMC simulations.

Conclusions from chapter 6 Adsorption isotherms for normal alkanes in ideal slit pores have been calculated using CB-GCMC. The behavior of alkanes in idealized pores serve as a valuable reference system for investigations of adsorption in activated carbons, lubrication, and adsorption in more complex geometries. The effects of alkane chain length, temperature, pressure and slit height on density and molecular ordering have been determined. Isotherms have been reported for alkanes ranging from ethane to pentadecane in slit widths ranging from 11 to 34 Å. The isotherms are generally of the type II classification by the IUPAC.

There is a strong similarity in the shape of the isotherms and density and orientation profiles across the range of alkanes and temperatures studied. These similarities suggest that the isotherms

may be collapsed through the appropriate use of thermodynamic variables. Collapsing theories typically used on type I isotherms had limited success at collapsing these type II isotherms. The similarity in the isotherms suggests that some way to collapse type II isotherms exists.

II Connections between chapters

Chapters 2 and 3 The experiments of Chapter 2 of rough and smooth particles are what prompted the simulations in Chapter 3 and the subsequent connection of granular mixtures to solution theory. With the structure created in Chapter 3, the experiments of Chapter 2 can now be examined by the principles of solution theory.

The experimental data in Chapter 2 show that the angle of repose of the mixture increases in a fairly linear fashion with the concentration of rough particles. This lends the system of rough and smooth particles to be labeled an “ideal” mixture by the characterization of Chapter 3. The linear or ideal behavior of the frictional system could only be produced in the simulations of Chapter 3 when $\mu_{A-A} > \mu_{A-B} > \mu_{B-B}$. This means that the friction coefficients in the experiment must have the relationship $\mu_{rough-rough} > \mu_{rough-smooth} > \mu_{smooth-smooth}$. This qualitative relationship between friction coefficients may seem obvious, but this relationship could not be obtained experimentally with any certainty. The solution theory analogy in Chapter 3 is in fact useful.

Chapters 3 and 4 It may prove difficult in practice to precisely control the adhesive properties of small particles to the degree desirable for the design of a damping device as suggested in Chapter 4. However, the theory of adhesive mixtures from Chapter 3 may help. Instead of controlling the adhesive properties of a homogeneous system, Chapter 3 suggests that precise control of the bulk adhesion behavior of a mixture may be gained by controlling the concentration of the two particle types. Controlling the concentration of particles in the damper is simply a matter of how much of each powder is put in.

Some control of adhesive forces between micro and nanoparticles has already been demonstrated through the use of surface coatings, so particles of at least two degrees of adhesion should be producible. As long as one interaction is stronger than needed, and the other weaker, the full

intermediate range of adhesion behavior can be achieved by controlling the concentration. The ideas of solution theory can aid in the device design of the damper.

Chapters 5 and 6 In Chapter 5, thermodynamic conditions capable of producing lubrication failure are connected, in part, to adsorption. Many more adsorption isotherms are reported in Chapter 6. The isotherms in Chapter 6 may be viewed with an understanding of lubrication failure in mind.

Chapter 6 also discusses theories used to collapse isotherms of different molecules at different temperatures. This idea of collapsing the isotherms can be useful to be able to predict the adsorption behavior for molecules not yet studied. In Chapter 5, pentadecane is the largest molecule studied. However, it is not the largest alkane used as a lubricant. The adsorption theories of Chapter 6 may enable the extrapolation of the behavior of pentadecane to even longer molecules to predict their failure conditions.

III Recommendations

Particle dynamics simulations offer a flexible framework to study the behavior of granular materials. There is almost no limit to the problems one can study considering the many combinations of flow geometry, length scale, and forces to model. The majority of the particle dynamics simulations in this dissertation were done in only two geometries: the rotating drum and shearing between parallel plates. The simulation methods used here could easily be extended to new geometries.

Other flow geometries which are likely to be affected by inter-particle friction and adhesion are: chute flow, hopper flow, screw feeders, and sieving. For example, intuition implies that flow from a hopper will be slowed for high friction or adhesion between particles, and that flow can be halted entirely when arching or clogging occurs. The relationship between surface forces and flow rates could acutely be studied through simulation.

During sieving, small particles are intended to pass through holes that are very close to their size in order to get good separation from larger particles. There are many areas of this operation

which can be investigated. Questions such as these could be answered: How is a sieving operation impeded by friction? What magnitude of adhesion forces can be overcome during sieving? The sieve is usually oscillated to enhance flow. Is there a relationship between the inter-particle forces and the amplitude and frequency of oscillation to maximize flow through the sieve?

Studies of different length scales and forces go somewhat hand in hand. Particularly at the smaller length scales there are many forces which can affect particle behavior. Our understanding of the interplay of these various forces could benefit from particle dynamics studies. Some forces of interest may include viscous forces from a flowing fluid, electrostatic forces which build up through tribo-charging, and the forces experienced by charged or ferromagnetic particles in an electric or magnetic field. The goal of studying these forces could be to develop ways to manipulate particles. For example, iron nanoparticles are finding many applications in the medical field. When injected into the body they can serve as an MRI resolution enhancer. Furthermore, techniques are being developed to manipulate them throughout the body with magnetic fields to deliver drugs to a target, or they can be made to generate a localized hyperthermic treatment with an alternating field. An understanding of the interplay between the applied (controlled) magnetic forces and the forces generated by the particle's environment is clearly needed to understand and optimize these technologies. Particle dynamics simulations can be useful to investigate the interplay of the magnetic force with viscous forces, van der Waals, electrostatic forces etc.

This method of connecting particle properties, and force models to collective behavior is a relatively straight forward process which can analyze systems with complicated and sometimes complex interactions. It holds great promise.

- [1] J. Duran. *Sands, powders, and grains*. Partially Ordered Systems. Springer, New York, 2000.
- [2] L. Abboud and S. Hensley. Factory shift: new prescription for drug makers: update the plants, 3 September 2003. Wall Street Journal.
- [3] B. J. Ennis, J. Green, and R. Davies. The legacy of neglect in the United States. *Chemical Engineering Progress*, 90(4):32–43, 1994.
- [4] H. M. Jaeger and S. R. Nagel. Physics of the granular state. *Science*, 255(5051):1523–1531, 1992.
- [5] H. M. Jaeger, S. R. Nagel, and R. P. Behringer. The physics of granular materials. *Physics Today*, 49(4):32–38, 1996.
- [6] H. M. Li and J. J. McCarthy. Controlling cohesive particle mixing and segregation. *Physical Review Letters*, 90(18), 2003.
- [7] P.-Y. Lai, L.-C. Jia, and C.K. Chan. Friction induced segregation of a granular binary mixture in a rotating drum. *Physical Review Letters*, 79(25):4994–4997, 1997.
- [8] S. Chakraborty, P.R. Nott, and J.R. Prakash. Analysis of radial segregation of granular mixtures in a rotating drum. *Eur. Phys. J. E*, 1:265–273, 2000.
- [9] T. Boutreux and P.G. de Gennes. Surface flows of granular mixtures: I. general principles and minimal model. *J. phys. I France*, 6:1295–1304, 1996.
- [10] N. A. Pohlman, B. L. Severson, J. M. Ottino, and R. M. Lueptow. Surface roughness effects in granular matter: Influence on angle of repose and the absence of segregation. *Physical Review E*, 73(3), 2006.

- [11] K.M. Hill, D.V. Khakhar, J.F. Gilchrist, J.J. McCarthy, and J.M. Ottino. Segregation-driven organization in chaotic granular flows. *PNAS*, 96(21):11701–11706, 1999.
- [12] Y. C. Zhou, B. D. Wright, R. Y. Yang, B. H. Xu, and A. B. Yu. Rolling friction in the dynamic simulation of sandpile formation. *Physica a-Statistical Mechanics and Its Applications*, 269(2-4):536–553, 1999.
- [13] Y. C. Zhou, B. H. Xu, A. B. Yu, and P. Zulli. Numerical investigation of the angle of repose of monosized spheres. *Physical Review E*, 6402(2), 2001.
- [14] Y. C. Zhou, B. H. Xu, A. B. Yu, and P. Zulli. An experimental and numerical study of the angle of repose of coarse spheres. *Powder Technology*, 125(1):45–54, 2002.
- [15] M.P. Allen and D.J. Tildesley. *Computer simulation of liquids*. Clarendon Press, Oxford, 1987.
- [16] R.W. Hockney and J.W. Eastwood. *Computer simulations using particles*. Hilger, New York, 1988.
- [17] F. Y. Fraige and P. A. Langston. Integration schemes and damping algorithms in distinct element models. *Advanced Powder Technology*, 15(2):227–245, 2004.
- [18] H. Hertz and J. Reine. On the contact of elastic solid. *Angew. Mathematik*, 92:156–171, 1882.
- [19] K. L. Johnson. *Contact Mechanics*. Cambridge University Press, New York, 1985.
- [20] R.D. Mindlin. Compliance of elastic bodies in contact. *J. Appl. Mech.*, 16:259, 1949.
- [21] P. A. Cundall and O. D. L. Strack. Discrete numerical-model for granular assemblies. *Geotechnique*, 29(1):47–65, 1979.
- [22] A. R. Savkoor and G. A. D. Briggs. Effect of tangential force on contact of elastic solids in adhesion. *Proceedings of the Royal Society of London Series a-Mathematical Physical and Engineering Sciences*, 356(1684):103–114, 1977.
- [23] Y. H. Taguchi. Powder turbulence - direct onset of turbulent-flow. *Journal De Physique II*, 2(12):2103–2114, 1992.

- [24] S. Luding, E. Clement, A. Blumen, J. Rajchenbach, and J. Duran. Anomalous energy-dissipation in molecular-dynamics simulations of grains - the detachment effect. *Physical Review E*, 50(5):4113–4122, 1994.
- [25] G. Kuwabara and K. Kono. Restitution coefficient in a collision between 2 spheres. *Japanese Journal of Applied Physics Part 1-Regular Papers Short Notes and Review Papers*, 26(8):1230–1233, 1987.
- [26] N. V. Brilliantov, F. Spahn, J. M. Hertzsch, and T. Poschel. Model for collisions in granular gases. *Physical Review E*, 53(5):5382–5392, 1996.
- [27] J. Schafer, S. Dippel, and D. E. Wolf. Force schemes in simulations of granular materials. *Journal De Physique I*, 6(1):5–20, 1996.
- [28] J.J. McCarthy, T. Shinbrot, G. Metcalfe, J.E. Wolf, and J.M. Ottino. Mixing of granular materials in slowly rotated containers. *AIChE Journal*, 42(12):3351–3363, 1996.
- [29] J.J. McCarthy and J.M. Ottino. Particle dynamics simulation: a hybrid technique applied to granular mixing. *Powder Technology*, 97:91–99, 1998.
- [30] K. D. Kafui, C. Thornton, and M. J. Adams. Discrete particle-continuum fluid modelling of gas-solid fluidised beds. *Chemical Engineering Science*, 57(13):2395–2410, 2002.
- [31] A. Dziugys and B. Peters. An approach to simulate the motion of spherical and non-spherical fuel particles in combustion chambers. *Granular Matter*, 3(4):231–265, 2001.
- [32] V. Buchholtz, T. Poschel, and H. J. Tillemans. Simulation of rotating drum experiments using noncircular particles. *Physica A*, 216(3):199–212, 1995.
- [33] H. G. Matuttis, S. Luding, and H. J. Herrmann. Discrete element simulations of dense packings and heaps made of spherical and non-spherical particles. *Powder Technology*, 109(1-3):278–292, 2000.

- [34] A. A. Mirghasemi, L. Rothenburg, and E. L. Matyas. Influence of particle shape on engineering properties of assemblies of two-dimensional polygon-shaped particles. *Geotechnique*, 52(3):209–217, 2002.
- [35] X. Lin and T. T. Ng. A three-dimensional discrete element model using arrays of ellipsoids. *Geotechnique*, 47(2):319–329, 1997.
- [36] X. S. Lin and T. T. Ng. Contact detection algorithms for 3-dimensional ellipsoids in discrete element modeling. *International Journal for Numerical and Analytical Methods in Geomechanics*, 19(9):653–659, 1995.
- [37] J. M. Ting, L. Meachum, and J. D. Rowell. Effect of particle-shape on the strength and deformation mechanisms of ellipse-shaped granular assemblages. *Engineering Computations*, 12(2):99–108, 1995.
- [38] J. M. Ting, M. Khwaja, L. R. Meachum, and J. D. Rowell. An ellipse-based discrete element model for granular-materials. *International Journal for Numerical and Analytical Methods in Geomechanics*, 17(9):603–623, 1993.
- [39] O. R. Walton and R. L. Braun. Viscosity, antigranulocytes-temperature, and stress calculations for shearing assemblies of inelastic, frictional disks. *Journal of Rheology*, 30(5):949–980, 1986.
- [40] S. Masson and J. Martinez. Effect of particle mechanical properties on silo flow and stresses from distinct element simulations. *Powder Technology*, 109(1-3):164–178, 2000.
- [41] H. P. Kuo, P. C. Knight, D. J. Parker, Y. Tsuji, M. J. Adams, and J. P. K. Seville. The influence of dem simulation parameters on the particle behaviour in a v-mixer. *Chemical Engineering Science*, 57(17):3621–3638, 2002.
- [42] D.C. Montgomery. *Design and Analysis of Experiments*. John Wiley and Sons, Hoboken, 6th edition, 2005.
- [43] W.B. Russel, D.A. Saville, and W.R. Schowalter. *Colloidal Dispersions*. UP, Cambridge, 1989.

- [44] A. G. Bailey. Electrostatic phenomena during powder handling. *Powder Technology*, 37:71–85, 1984.
- [45] M. Polanyi and F. London. *naturwissenschaften*, 18:1099, 1930.
- [46] H.C. Hamaker. The london-van der waals attraction between spherical particles. *Physica*, 4(10):1058–1072, 1937.
- [47] J.N. Israelachvili. *Intermolecular and surface forces*. Academic Press, New York, 2003.
- [48] D. Henderson, D. M. Duh, X. L. Chu, and D. Wasan. An expression for the dispersion force between colloidal particles. *Journal of Colloid and Interface Science*, 185(1):265–268, 1997.
- [49] K.L. Johnson, K. Kendall, and A.D. Roberts. Surface energy and the contact of elastic solids. *Proc. R. Soc. Lond. A*, 324:301–313, 1971.
- [50] B. V. Derjaguin, V. M. Muller, and Y. P. Toporov. Effect of contact deformations on adhesion of particles. *Journal of Colloid and Interface Science*, 53(2):314–326, 1975.
- [51] K. Kendall. *Molecular adhesion and its applications: the sticky universe*. Kluwer Academic/Plenum publishers, New York, 2001.
- [52] H. Rumpf. Science of agglomeration. *Chemie Ingenieur Technik*, 46(1):1–11, 1974.
- [53] Y. I. Rabinovich, J. J. Adler, A. Ata, R. K. Singh, and B. M. Moudgil. Adhesion between nanoscale rough surfaces - i. role of asperity geometry. *Journal of Colloid and Interface Science*, 232(1):10–16, 2000.
- [54] A. Samadani and A. Kudrolli. Angle of repose and segregation in cohesive granular matter. *Physical Review E*, 6405(5), 2001.
- [55] G. P. Lian, C. Thornton, and M. J. Adams. A theoretical-study of the liquid bridge forces between 2 rigid spherical bodies. *Journal of Colloid and Interface Science*, 161(1):138–147, 1993.
- [56] S. T. Nase, W. L. Vargas, A. A. Abatan, and J. J. McCarthy. Discrete characterization tools for cohesive granular material. *Powder Technology*, 116(2-3):214–223, 2001.

- [57] J.J. McCarthy. Micro-modeling of cohesive mixing processes. *Powder Technology*, 138:63–67, 2003.
- [58] H. M. Li and J. J. McCarthy. Cohesive particle mixing and segregation under shear. *Powder Technology*, 164(1):58–64, 2006.
- [59] H. M. Li and J. J. McCarthy. Phase diagrams for cohesive particle mixing and segregation. *Physical Review E*, 71(2), 2005.
- [60] J. Krim. Surface science and the atomic-scale origins of friction: what was old is new again. *Surface Science*, 500:741–758, 2002.
- [61] J. Krim. Friction at the atomic scale. *Scientific American*, pages 74–80, October 1996.
- [62] M. Cieplak, E. Smith, and M. Robbins. Molecular origins of friction: the force on adsorbed layers. *Science*, 265:1209–1212, 1994.
- [63] J. N. Israelachvili, Y. L. Chen, and H. Yoshizawa. Relationship between adhesion and friction forces. *Journal of Adhesion Science and Technology*, 8(11):1231–1249, 1994.
- [64] D. Geldart. Effect of particle-size and size distribution on behavior of gas-fluidized beds. *Powder Technology*, 6(4):201, 1972.
- [65] A. Castellanos, J. M. Valverde, A. T. Perez, A. Ramos, and P. K. Watson. Flow regimes in fine cohesive powders. *Physical Review Letters*, 82(6):1156–1159, 1999.
- [66] A. Castellanos, J. M. Valverde, and A. T. Prez. The dynamics of fine powders in a rotating drum. *Inorganic Materials*, 35(8):837–841, 1999.
- [67] J. M. Valverde, A. Ramos, A. Castellanos, and P. K. Watson. The tensile strength of cohesive powders and its relationship to consolidation, free volume and cohesivity. *Powder Technology*, 97(3):237–245, 1998.
- [68] J. M. Valverde, A. Castellanos, and P. K. Watson. The effect of particle size on interparticle adhesive forces for small loads. *Powder Technology*, 118(3):236–241, 2001.

- [69] J. M. Valverde, M. A. S. Quintanilla, and A. Castellanos. Jamming threshold of dry fine powders. *Physical Review Letters*, 92(25), 2004.
- [70] R. Jones, H. M. Pollock, D. Geldart, and A. Verlinden-Luts. Frictional forces between cohesive powder particles studied by afm. *Ultramicroscopy*, 100(1-2):59–78, 2004.
- [71] M. Gotzinger and W. Peukert. Dispersive forces of particle-surface interactions: direct afm measurements and modelling. *Powder Technology*, 130(1-3):102–109, 2003.
- [72] R. Jones. From single particle afm studies of adhesion and friction to bulk flow: Forging the links. *Granular Matter*, 4(4):191–204, 2003.
- [73] C. S. Hodges, J. A. S. Cleaver, M. Ghadiri, R. Jones, and H. M. Pollock. Forces between polystyrene particles in water using the afm: Pull-off force vs particle size. *Langmuir*, 18(15):5741–5748, 2002.
- [74] A. Karolyi, J. Kertesz, S. Havlin, H. A. Makse, and H. E. Stanley. Filling a silo with a mixture of grains: Friction-induced segregation. *Europhysics Letters*, 44:386, 1998.
- [75] D. I. Goldman, M. D. Shattuck, S. J. Moon, J. B. Swift, and H. L. Swinney. Lattice dynamics and melting of a nonequilibrium pattern. *Physical Review Letters*, 90(10), 2003.
- [76] Y. C. Zhou, B. H. Xu, A. B. Yu, and P. Zulli. Numerical investigation of the angle of repose of monosized spheres. *Physical Review E*, 6402(2), 2001.
- [77] Y. C. Zhou, B. H. Xu, A. B. Yu, and P. Zulli. An experimental and numerical study of the angle of repose of coarse spheres. *Powder Technology*, 125(1):45–54, 2002.
- [78] G. H. Ristow. Pattern formation in granular materials - introduction. In *Pattern Formation in Granular Materials*, volume 164 of *Springer Tracts in Modern Physics*, pages 1–+. 2000.
- [79] M. Mullier, U. Tuzun, and O. R. Walton. A single-particle friction cell for measuring contact frictional-properties of antigranulocytes materials. *Powder Technology*, 65(1-3):61–74, 1991.
- [80] R. G. Cain, N. W. Page, and S. Biggs. Microscopic and macroscopic effects of surface lubricant films in granular shear. *Physical Review E*, 62(6):8369–8379, 2000.

- [81] A. V. Orpe and D. V. Khakhar. Scaling relations for granular flow in quasi-two-dimensional rotating cylinders. *Physical Review E*, 6403(3), 2001.
- [82] K. M. Hill and J. Kakalios. Reversible axial segregation of rotating granular media. *Physical Review E*, 52(4):4393–4400, 1995.
- [83] C. M. Dury, G. H. Ristow, J. L. Moss, and M. Nakagawa. Boundary effects on the angle of repose in rotating cylinders. *Physical Review E*, 57(4):4491–4497, 1998.
- [84] S. N. Dorogovtsev and J. F. F. Mindes. Time of avalanche mixing of granular materials in a half filled drum. *European Physical Journal E*, 5(4):441–444, 2001.
- [85] N. Thomas. Reverse and intermediate segregation of large beads in dry granular media. *Physical Review E*, 62(1):961–974, 2000.
- [86] N. Jain, J. M. Ottino, and R. M. Lueptow. Regimes of segregation and mixing in combined size and density granular systems: an experimental study. *Granular Matter*, 7(2-3):69–81, 2005.
- [87] G. Felix and N. Thomas. Evidence of two effects in the size segregation process in dry granular media. *Physical Review E*, 70(5), 2004.
- [88] Y. Oyama. *Bulletin of the Institute for Physical Chemistry Research*, 18:600, 1939.
- [89] B. Roseman and M.B. Donald. *International Chemical Engineering*, 7:823, 1962.
- [90] S. J. Fiedor and J. M. Ottino. Dynamics of axial segregation and coarsening of dry granular materials and slurries in circular and square tubes. *Physical Review Letters*, 91(24), 2003.
- [91] S. B. Savage and C. K. K. Lun. Particle-size segregation in inclined chute flow of dry cohesionless granular solids. *Journal of Fluid Mechanics*, 189:311–335, 1988.
- [92] P.-Y. Lai, L.-C. Jia, and C.K. Chan. Friction induced segregation of a granular binary mixture in a rotating drum. *Physical Review Letters*, 79(25):4994–4997, 1997.

- [93] Z. S. Khan and S. W. Morris. Subdiffusive axial transport of granular materials in a long drum mixer. *Physical Review Letters*, 94(4), 2005.
- [94] J. F. Gilchrist and J. M. Ottino. Competition between chaos and order: Mixing and segregation in a spherical tumbler. *Physical Review E*, 68(6), 2003.
- [95] K. M. Hill, G. Gioia, and V. V. Tota. Structure and kinematics in dense free-surface granular flow. *Physical Review Letters*, 91(6), 2003.
- [96] S. Das Gupta, D.V. Khakhar, and S.K. Bhatia. *Chemical Engineering Science*, 46:1513, 1991.
- [97] N. Taberlet, P. Richard, A. Valance, W. Losert, J. M. Pasini, J. T. Jenkins, and R. Delannay. Superstable granular heap in a thin channel. *Physical Review Letters*, 91(26), 2003.
- [98] N. Taberlet, P. Richard, E. Henry, and R. Delannay. The growth of a super stable heap: An experimental and numerical study. *Europhysics Letters*, 68(4):515–521, 2004.
- [99] S.B. Ogalea, R.N. Bathea, R.J. Choudharya, Kalea S.N., A.G. Ogalea, A.G. Banpurkarb, and A.V. Limaye. *Statistical Mechanics and its Applications*, 354:49, 2005.
- [100] N. A. Pohlman, S. W. Meier, R. M. Lueptow, and J. M. Ottino. Surface velocity in three-dimensional granular tumblers. *Journal of Fluid Mechanics*, 560:355–368, 2006.
- [101] A. B. Yu, C. L. Feng, R. P. Zou, and R. Y. Yang. On the relationship between porosity and interparticle forces. *Powder Technology*, 130(1-3):70–76, 2003.
- [102] J.J. McCarthy, T. Shinbrot, G. Metcalfe, J.E. Wolf, and J.M. Ottino. Mixing of granular materials in slowly rotated containers. *AIChE Journal*, 42(12):3351–3363, 1996.
- [103] C. M. Dury and G. H. Ristow. Radial segregation in a two-dimensional rotating drum. *Journal De Physique I*, 7(5):737–745, 1997.
- [104] J.J. McCarthy and J.M. Ottino. Particle dynamics simulation: a hybrid technique applied to granular mixing. *Powder Technology*, 97:91–99, 1998.

- [105] C. M. Dury and G. H. Ristow. Competition of mixing and segregation in rotating cylinders. *Physics of Fluids*, 11(6):1387–1394, 1999.
- [106] J. J. McCarthy, D. V. Khakhar, and J. M. Ottino. Computational studies of granular mixing. *Powder Technology*, 109(1-3):72–82, 2000.
- [107] D.C. Rapaport. *Physical Review E*, 65:061306, 2002.
- [108] J. Schafer, S. Dippel, and D. E. Wolf. Force schemes in simulations of granular materials. *Journal De Physique I*, 6(1):5–20, 1996.
- [109] H. M. Jaeger, S. R. Nagel, and R. P. Behringer. The physics of granular materials. *Physics Today*, 49(4):32–38, 1996.
- [110] R.S. Saksena and L.V. Woodcock. Quasi-thermodynamics of powders and granular dynamics. *Physical Chemistry Chemical Physics*, 6:5195–5202, 2004.
- [111] H. M. Li and J. J. McCarthy. Phase diagrams for cohesive particle mixing and segregation. *Physical Review E*, 71(2), 2005.
- [112] G. D’Anna, P. Mayor, A. Barrat, V. Loreto, and F. Nori. Observing brownian motion in vibration-fluidized granular matter. *Nature*, 424(6951):909–912, 2003.
- [113] H. J. Herrmann. On the thermodynamics of granular media. *Journal De Physique Ii*, 3(4):427–433, 1993.
- [114] Anita Mehta. A phenomenological approach to relaxation in powders. *Physica A*, 168:714–722, 1990.
- [115] Anita Mehta and S.F. Edwards. Statistical mechanics of powder mixtures. *Physica A*, 157:1091–1100, 1989.
- [116] M. P. Ciamarra, A. Coniglio, and M. Nicodemi. Thermodynamics and statistical mechanics of dense granular media. *Physical Review Letters*, 97(15), 2006.

- [117] H. M. Jaeger, S. R. Nagel, and R. P. Behringer. Granular solids, liquids, and gases. *Reviews of Modern Physics*, 68(4):1259–1273, 1996.
- [118] A.V. Orpe and D.V. Khakhar. Solid-fluid transition in a granular shear flow. *Physical Review Letters*, 93(6):068001, 2004.
- [119] J. Casas-Vazquez and D. Jou. Temperature in non-equilibrium states: a review of open problems and current proposals. *Reports on Progress in Physics*, 66(11):1937–2023, 2003.
- [120] S.I. Sandler. *Chemical and Engineering Thermodynamics 3rd Ed.* John Wiley and Sons, New York, third edition edition, 1999.
- [121] J.M. Smith, H.C. Van Ness, and M.M. Abbott. *Introduction to Chemical Engineering Thermodynamics 6th Ed.* McGraw-Hill, New York, sixth edition edition, 2001.
- [122] J. Schafer, S. Dippel, and D. E. Wolf. Force schemes in simulations of granular materials. *Journal De Physique I*, 6(1):5–20, 1996.
- [123] P. A. Cundall and O. D. L. Strack. Discrete numerical-model for granular assemblies. *Geotechnique*, 29(1):47–65, 1979.
- [124] N. A. Pohlman, B. L. Severson, J. M. Ottino, and R. M. Lueptow. Surface roughness effects in granular matter: Influence on angle of repose and the absence of segregation. *Physical Review E*, 73(3), 2006.
- [125] R. D. Friend and V. K. Kinra. Particle impact damping. *Journal of Sound and Vibration*, 233(1):93–118, 2000.
- [126] C. M. Yu, K. Craig, and J. Tichy. Granular collision lubrication. *Journal of Rheology*, 38(4):921–936, 1994.
- [127] Z. W. Xu, M. Y. Wang, and T. N. Chen. An experimental study of particle damping for beams and plates. *Journal of Vibration and Acoustics-Transactions of the ASME*, 126(1):141–148, 2004.
- [128] W. Liu, G. R. Tomlinson, and J. A. Rongong. The dynamic characterisation of disk geometry particle dampers. *Journal of Sound and Vibration*, 280(3-5):849–861, 2005.

- [129] A. Papalou and S. F. Masri. Performance of particle dampers under random excitation. *Journal of Vibration and Acoustics-Transactions of the ASME*, 118(4):614–621, 1996.
- [130] K. M. Mao, M. Y. Wang, Z. W. Xu, and T. N. Chen. Dem simulation of particle damping. *Powder Technology*, 142(2-3):154–165, 2004.
- [131] J.N. Israelachvili. *Intermolecular and surface forces 2nd Ed.* Elsevier, New York, 1992.
- [132] K. Z. Y. Yen and T. K. Chaki. A dynamic simulation of particle rearrangement in powder packings with realistic interactions. *Journal of Applied Physics*, 71(7):3164–3173, 1992.
- [133] K.L. Johnson. In W.T. Koiter, editor, *Theoretical and Applied Mechanics*, page 133. North-Holland, 1976.
- [134] C. Thornton. Interparticle sliding in the presence of adhesion. *Journal of Physics D-Applied Physics*, 24(11):1942–1946, 1991.
- [135] C. Thornton and K. K. Yin. Impact of elastic spheres with and without adhesion. *Powder Technology*, 65(1-3):153–166, 1991.
- [136] V. S. Mangipudi, E. Huang, M. Tirrell, and A. V. Pocius. Measurement of interfacial adhesion between glassy polymers using the jkr method. *Macromolecular Symposia*, 102:131–143, 1996.
- [137] K. R. Shull. Contact mechanics and the adhesion of soft solids. *Materials Science and Engineering R-Reports*, 36(1):1–45, 2002.
- [138] U. Landman and W. D. Luedtke. Nanomechanics and dynamics of tip substrate interactions. *Journal of Vacuum Science and Technology B*, 9(2):414–423, 1991.
- [139] H. Yoshizawa, Y. L. Chen, and J. Israelachvili. Fundamental mechanisms of interfacial friction: Relation between adhesion and friction. *Journal of Physical Chemistry*, 97(16):4128–4140, 1993.
- [140] A.E. Filippov, J. Klafter, and M. Urbakh. Friction through dynamical formation and rupture of molecular bonds. *Physical Review Letters*, 92(13):1–4, 2004.

- [141] W.F. Bowman and G.W. Stachowiak. A review of scuffing models. *Tribology Letters*, 2(2):113–131, 1996.
- [142] G.W. Stachowiak and A.W. Batchelor. *Engineering Tribology*. Butterworth-Heinemann, Boston, 2001.
- [143] S. C. Lee and H. S. Cheng. Scuffing theory modeling and experimental correlations. *Journal of Tribology-Transactions of the Asme*, 113(2):327–334, 1991.
- [144] D. E. Deckman, S. Jahanmir, and S. M. Hsu. Wear mechanisms of alpha-alumina lubricated with a paraffin oil. *Wear*, 149(1-2):155–168, 1991.
- [145] S. Jahanmir and M. Beltzer. An adsorption model for friction in boundary lubrication. *Asle Transactions*, 29(3):423–430, 1986.
- [146] H. Aramaki, H. S. Cheng, and D. Zhu. Film thickness, friction, and scuffing failure of rib roller end contacts in cylindrical roller-bearings. *Journal of Tribology-Transactions of the Asme*, 114(2):311–316, 1992.
- [147] J. Castro and J. Seabra. Scuffing and lubricant film breakdown in fzg gears part i. analytical and experimental approach. *Wear*, 215(1-2):104–113, 1998.
- [148] Y. Z. Lee and K. C. Ludema. The effects of surface roughening and protective film formation on scuff initiation in boundary lubrication. *Journal of Tribology-Transactions of the Asme*, 113(2):295–302, 1991.
- [149] E. E. Klaus, J. L. Duda, and K. K. Chao. A study of wear chemistry using a micro sample 4-ball wear test. *Tribology Transactions*, 34(3):426–432, 1991.
- [150] E. C. Cutiongco and Y. W. Chung. Prediction of scuffing failure based on competitive kinetics of oxide formation and removal - application to lubricated sliding of aisi-52100 steel on steel. *Tribology Transactions*, 37(3):622–628, 1994.
- [151] D. M. Bailey and R. S. Sayles. Effect of roughness and sliding friction on contact stresses. *Journal of Tribology-Transactions of the Asme*, 113(4):729–738, 1991.

- [152] S. Wang and K. Komvopoulos. A fractal theory of the temperature distribution at elastic contacts of fast sliding surfaces. *Journal of Tribology-Transactions of the Asme*, 117(2):203–214, 1995.
- [153] H. Li, K. K. Chao, J. L. Duda, and E. E. Klaus. A study of wear chemistry and contact temperature using a microsample four-ball wear test. *Tribology Transactions*, 42(3):529–534, 1999.
- [154] F.P. Bowden and D. Tabor. *Friction and lubrication of solids*. International series of monographs on physics. Clarendon Press, Oxford, 1986 edition, 1958.
- [155] B. Vick, M. J. Furey, and K. Iskandar. Theoretical surface temperatures generated from sliding contact of pure metallic elements. *Tribology International*, 33(3-4):265–271, 2000.
- [156] B. Vick, M. J. Furey, and K. Iskandar. Surface temperatures generated by friction with ceramic materials. *Tribology Transactions*, 42(4):888–894, 1999.
- [157] J. Castro and J. Seabra. Scuffing and lubricant film breakdown in fzg gears part ii. new pv scuffing criteria, lubricant and temperature dependent. *Wear*, 215(1-2):114–122, 1998.
- [158] A. Dyson. Scuffing, a review. *Tribology International*, 8:77–87, 1975.
- [159] L. Zhang, R. Balasundaram, S. Gehrke, and S. Jiang. Nonequilibrium molecular dynamics simulations of confined fluids in contact with the bulk. *Journal of Chemical Physics*, 114(15):6869–6877, 2001.
- [160] M. Schoen, J. H. Cushman, D. J. Diestler, and C. L. Rhykerd. Fluids in micropores .2. self-diffusion in a simple classical fluid in a slit pore. *Journal of Chemical Physics*, 88(2):1394–1406, 1988.
- [161] C. Lastoskie, K. E. Gubbins, and N. Quirke. Pore-size heterogeneity and the carbon slit pore - a density-functional theory model. *Langmuir*, 9(10):2693–2702, 1993.
- [162] H. Dominguez, M. P. Allen, and R. Evans. Monte carlo studies of the freezing and condensation transitions of confined fluids. *Molecular Physics*, 96(2):209–229, 1999.

- [163] D. P. Cao and W. C. Wang. Simulation of microscopic structure of propane adsorbed in slit micropores. *Acta Physico-Chimica Sinica*, 15(7):581–587, 1999.
- [164] J. E. Curry. Structure of a model lubricant in a mica slit pore. *Journal of Chemical Physics*, 113(6):2400–2406, 2000.
- [165] D. P. Cao and W. C. Wang. Grand canonical ensemble monte carlo simulation for determination of pore size of activated carbon. *Chemical Journal of Chinese Universities-Chinese*, 23(5):910–914, 2002.
- [166] P. B. Balbuena and K. E. Gubbins. Theoretical interpretation of adsorption behavior of simple fluids in slit pores. *Langmuir*, 9(7):1801–1814, 1993.
- [167] R.F. Cracknell and D. Nicholson. Grand canonical monte carlo study of lennard-jones mixtures in slit pores: Part 3. *J. Chem. Soc. Faraday Trans.*, 90(11):1487–1493, 1994.
- [168] S. Bhatia. Adsorption of binary hydrocarbon mixtures in carbon slit pores: a density functional theory study. *Langmuir*, 14:6231–6240, 1998.
- [169] A. V. Shevade, S. Y. Jiang, and K. E. Gubbins. Molecular simulation study of water-methanol mixtures in activated carbon pores. *Journal of Chemical Physics*, 113(16):6933–6942, 2000.
- [170] R. Radhakrishnan, K.E. Gubbins, and M. Sliwinska-Bartkowiak. Global phase diagrams for freezing in porous media. *Journal of Chemical Physics*, 116(3):1147–1151, 2002.
- [171] L.D. Gelb, K.E. Gubbins, R. Radhakrishnan, and M. Sliwinska-Bartkowiak. Phase separation in confined systems. *Rep. Prog. Phys.*, 62:1573–1659, 1999.
- [172] P.B. Balbuena, D. Berry, and K.E. Gubbins. Solvation pressures for simple fluids in micropores. *J. Phys. Chem.*, 97:937–943, 1993.
- [173] S. Chempath, J. F. M. Denayer, K. M. A. De Meyer, G. V. Baron, and R. Q. Snurr. Adsorption of liquid-phase alkane mixtures in silicalite: Simulations and experiment. *Langmuir*, 20(1):150–156, 2004.

- [174] M. D. Macedonia and E. J. Maginn. A biased grand canonical monte carlo method for simulating adsorption using all-atom and branched united atom models. *Molecular Physics*, 96(9):1375–1390, 1999.
- [175] M.P. Allen and D.J. Tildesley. *Computer simulation of liquids*. Clarendon Press, Oxford, 1987.
- [176] A. Gupta, S. Chempath, M. J. Sanborn, L. A. Clark, and R. Q. Snurr. Object-oriented programming paradigms for molecular modeling. *Molecular Simulation*, 29(1):29–46, 2003.
- [177] J. Gao, W.D. Luedtke, and U. Landman. Structure and solvation forces in confined films: linear and branched alkanes. *Journal of Chemical Physics*, 106(10):4309–4318, 1996.
- [178] J. C. Wang and K. A. Fichthorn. Molecular dynamics studies of the effects of chain branching on the properties of confined alkanes. *Journal of Chemical Physics*, 116(1):410–417, 2002.
- [179] F. Porcheron, B. Rousseau, and A.H. Fuchs. Structure of ultra-thin confined alkane films from monte carlo simulations. *Molecular Physics*, 100(13):2109–2119, 2002.
- [180] F. Porcheron, B. Rousseau, M. Schoen, and A. H. Fuchs. Structure and solvation forces in confined alkane films. *Physical Chemistry Chemical Physics*, 3(7):1155–1159, 2001.
- [181] M. Schoen, D. J. Diestler, and J. H. Cushman. Fluids in micropores. iv. the behavior of molecularly thin confined films in the grand isostress ensemble. *Journal of Chemical Physics*, 100(10):7707–7717, 1994.
- [182] J. J. Magda, M. Tirrell, and H. T. Davis. Molecular-dynamics of narrow, liquid-filled pores. *Journal of Chemical Physics*, 83(4):1888–1901, 1985.
- [183] J. Samuel, C. J. Brinker, L. J. D. Frink, and F. van Swol. Direct measurement of solvation forces in complex microporous media: A new characterization tool. *Langmuir*, 14(10):2602–2605, 1998.
- [184] C. Ghatak and K. G. Ayappa. Solvation force, structure and thermodynamics of fluids confined in geometrically rough pores. *Journal of Chemical Physics*, 120(20):9703–9714, 2004.

- [185] J. P. Gao, W. D. Luedtke, and U. Landman. Layering transitions and dynamics of confined liquid films. *Physical Review Letters*, 79(4):705–708, 1997.
- [186] S. C. Lee and H. S. Cheng. Scuffing theory modeling and experimental correlations. *Journal of Tribology-Transactions of the Asme*, 113(2):327–334, 1991.
- [187] S. A. Gupta, H. D. Cochran, and P. T. Cummings. Shear behavior of squalane and tetracosane under extreme confinement .2. confined film structure. *Journal of Chemical Physics*, 107(23):10327–10334, 1997.
- [188] J.N. Israelachvili. *Intermolecular and surface forces*. Academic Press, New York, 2003.
- [189] A. R. C. Baljon and M. O. Robbins. Adhesion and friction of thin films. *Mrs Bulletin*, 22(1):22–26, 1997.
- [190] K. R. Matranga, A. L. Myers, and E. D. Glandt. Storage of natural-gas by adsorption on activated carbon. *Chemical Engineering Science*, 47(7):1569–1579, 1992.
- [191] S. Altwasser, C. Welker, Y. Traa, and J. Weitkamp. Catalytic cracking of n-octane on small-pore zeolites. *Microporous and Mesoporous Materials*, 83(1-3):345–356, 2005.
- [192] D. S. Maciver, P. H. Emmett, and H. S. Frank. Alkane adsorption on silica, alumina and silica-alumina catalysts. *Journal of Physical Chemistry*, 62(8):935–942, 1958.
- [193] A. H. Fuchs and A. K. Cheetham. Adsorption of guest molecules in zeolitic materials: Computational aspects. *Journal of Physical Chemistry B*, 105(31):7375–7383, 2001.
- [194] B. Smit and J. I. Siepmann. Simulating the adsorption of alkanes in zeolites. *Science*, 264(5162):1118–1120, 1994.
- [195] J. P. Fox, V. Rooy, and S. P. Bates. Simulating the adsorption of linear, branched and cyclic alkanes in silicalite-1 and alpo4-5. *Microporous and Mesoporous Materials*, 69(1-2):9–18, 2004.
- [196] A. Gupta, L. A. Clark, and R. Q. Snurr. Grand canonical monte carlo simulations of nonrigid molecules: Siting and segregation in silicalite zeolite. *Langmuir*, 16(8):3910–3919, 2000.

- [197] J. W. Jiang, S. I. Sandler, M. Schenk, and B. Smit. Adsorption and separation of linear and branched alkanes on carbon nanotube bundles from configurational-bias monte carlo simulation. *Physical Review B*, 72(4), 2005.
- [198] T. Duren, L. Sarkisov, O. M. Yaghi, and R. Q. Snurr. Design of new materials for methane storage. *Langmuir*, 20(7):2683–2689, 2004.
- [199] H. Frost, T. Duren, and R. Q. Snurr. Effects of surface area, free volume, and heat of adsorption on hydrogen uptake in metal-organic frameworks. *Journal of Physical Chemistry B*, 110(19):9565–9570, 2006.
- [200] T. J. Bandosz, M. J. Biggs, K. E. Gubbins, Y. Hattori, T. Iiyama, K. Kaneko, J. Pikunic, and K. T. Thomson. Molecular models of porous carbons. *Chemistry and Physics of Carbon*, 28:41–228, 2003.
- [201] N. A. Seaton, S. P. Friedman, J. M. D. MacElroy, and B. J. Murphy. The molecular sieving mechanism in carbon molecular sieves: A molecular dynamics and critical path analysis. *Langmuir*, 13(5):1199–1204, 1997.
- [202] K. S. Walton, C. L. Cavalcante, and M. D. Levan. Adsorption equilibrium of alkanes on a high surface area activated carbon prepared from brazilian coconut shells. *Adsorption-Journal of the International Adsorption Society*, 11(2):107–111, 2005.
- [203] C. E. Holland, S. A. Al-Muhtaseb, and J. A. Ritter. Adsorption of c-1-c-7 normal alkanes on bax activated carbon. 1. potential theory correlation and adsorbent characterization. *Industrial and Engineering Chemistry Research*, 40(1):338–346, 2001.
- [204] A. Matsumoto, J. X. Zhao, and K. Tsutsumi. Adsorption behavior of hydrocarbons on slit-shaped micropores. *Langmuir*, 13(3):496–501, 1997.
- [205] R. Balasundaram, S. Y. Jiang, and J. Belak. Structural and rheological properties of n-decane confined between graphite surfaces. *Chemical Engineering Journal*, 74(1-2):117–127, 1999.

- [206] J. C. Wang and K. A. Fichthorn. Influence of molecular structure on the properties of confined fluids by molecular dynamics simulation. *Colloids and Surfaces a-Physicochemical and Engineering Aspects*, 206(1-3):267–276, 2002.
- [207] S. T. Cui, S. A. Gupta, P. T. Cummings, and H. D. Cochran. Molecular dynamics simulations of the rheology of normal decane, hexadecane, and tetracosane. *Journal of Chemical Physics*, 105(3):1214–1220, 1996.
- [208] A. Martini, Y. Liu, R. Q. Snurr, and Q. J. Wang. Molecular dynamics characterization of thin film viscosity for ehl simulation. *Tribology Letters*, 21(3):217–225, 2006.
- [209] M. Dijkstra. Confined thin films of linear and branched alkanes. *Journal of Chemical Physics*, 107(8):3277–3288, 1997.
- [210] M. Schoen, T. Gruhn, and D. J. Diestler. Solvation forces in thin films confined between macroscopically curved substrates. *Journal of Chemical Physics*, 109(1):301–311, 1998.
- [211] M. Schoen, C. L. Rhykerd, J. H. Cushman, and D. J. Diestler. Slit-pore sorption isotherms by the grand-canonical monte-carlo method - manifestations of hysteresis. *Molecular Physics*, 66(6):1171–1182, 1989.
- [212] A.V. Klochko, E. N. Brodskaya, and E. M. Piotrovskaya. Computer simulations of dependence of adsorption characteristics of ethane on the size of graphite micropores. *Langmuir*, 15:545–552, 1999.
- [213] J. C. Wang and K. A. Fichthorn. Molecular dynamics studies of the effects of chain branching on the properties of confined alkanes. *Journal of Chemical Physics*, 116(1):410–417, 2002.
- [214] A. R. C. Baljon and M. O. Robbins. Energy dissipation during rupture of adhesive bonds. *Science*, 271(5248):482–484, 1996.
- [215] K. F. Mansfield and D. N. Theodorou. Atomistic simulation of a glassy polymer surface. *Macromolecules*, 23(20):4430–4445, 1990.

- [216] T. K. Xia and U. Landman. Molecular-dynamics of adsorption and segregation from an alkane mixture. *Science*, 261(5126):1310–1312, 1993.
- [217] B.L. Severson, R. Q. Snurr, and J.M. Ottino. Analysis of lubrication failure using molecular simulation. *Tribology Letters*, 23(3):253–260, 2006.
- [218] G. L. Aranovich and M. D. Donohue. Adsorption-isotherms for microporous adsorbents. *Carbon*, 33(10):1369–1375, 1995.
- [219] M. D. LeVan, G. Carta, and C.M. Yon. Adsorption and ion exchange. In R.H. Perry, editor, *Perry's Chemical Engineers' Handbook*. McGraw-Hill, New York, 1997.
- [220] G. O. Wood. Affinity coefficients of the polanyi/dubinin adsorption isotherm equations - a review with compilations and correlations. *Carbon*, 39(3):343–356, 2001.
- [221] X. H. Ye, N. Qi, Y. Q. Ding, and M. D. LeVan. Prediction of adsorption equilibrium using a modified d-r equation: pure organic compounds on bpl carbon. *Carbon*, 41(4):681–686, 2003.